

**Analysis of the Demonstrator Readout of the
Liquid-Argon Calorimeter at the ATLAS Detector**

DISSERTATION

zur Erlangung des akademischen Grades

**Doctor rerum naturalium
(Dr. rer. nat.)**

vorgelegt der

**Fakultät Physik des
Bereichs Mathematik und Naturwissenschaften der
Technischen Universität Dresden**

von

**M.Sc. Maximilian Hils
geboren am 23. Oktober 1986 in Frankfurt am Main**

Eingereicht am: 20. Dezember 2019

Verteidigt am: 21. September 2020

Die Dissertation wurde in der Zeit von August 2015 bis Dezember 2019 im
Institut für Kern- und Teilchenphysik angefertigt.

1. Gutachter: Prof. Dr. Arno Straessner
2. Gutachter: Prof. Yuji Enari

Kurzdarstellung

Die laufenden Aufrüstungsarbeiten des Large Hadron Colliders haben das Ziel, die Luminosität der Teilchenkollisionen zu erhöhen. Die erhöhte Luminosität liefert zwar neue Möglichkeiten für Präzisionsmessungen und Teilchensuchen, stellt aber gleichzeitig eine große Herausforderung an die beteiligten Experimente. Aus diesem Grund wird auch der ATLAS-Detektor auferüstet. Der Fokus ist dabei, eine hohe Effizienz des Triggers sicherzustellen, der die interessantesten Physikereignisse in Echtzeit auswählt. Dafür wird das Flüssig-Argon-Kalorimeter des ATLAS-Detektors mit einer neuen Ausleseelektronik ausgerüstet.

Um die Funktionsfähigkeit zu testen, wurde ein Demonstrationsaufbau der zukünftigen Ausleseelektronik installiert und von 2014 bis 2018 parallel zur ATLAS-Datennahme betrieben. In dieser Arbeit werden die Daten, die mit dem Aufbau aufgezeichnet wurden, analysiert. Die neue Ausleseelektronik erlaubt es, komplexere Algorithmen zur Erkennung von Signal- und Untergrundereignissen zu nutzen. Es handelt sich dabei um Variablen zur Beschreibung der Form von elektromagnetischen und hadronischen Teilchenschauern im Flüssig-Argon-Kalorimeter. Die Effizienz dieser Variablen wird untersucht. Dabei wird nach Kombination mehrerer Variablen eine Untergrundunterdrückung hadronischer Jets von 75 % bei einer Elektronenerkennungseffizienz von 90 % erreicht.

Die zukünftige, erhöhte Luminosität führt dazu, dass sich bei Teilchenkollisionen die Zahl der Ereignisse, die sich sowohl zeitlich als auch räumlich überlappen, erhöht. Der Effekt dieser Überlappereignisse hat Auswirkungen auf die Energierekonstruktion. Daher wird eine Untersuchung der Überlappereignisse durchgeführt, um eine möglichst genaue Kenntnis über diese zu erhalten.

Für die Rekonstruktion aus den Signalen der im Detektor deponierten Energie stehen verschiedene digitale Signalfilter zur Auswahl. Die Performanz hinsichtlich der Signalerkennung dieser Algorithmen wird überprüft. Es zeigt sich, dass neue digitale Signalfilter zwar den Effekt des zeitlichen Überlapps von Detektorpulsen reduzieren, jedoch sehr sensitiv auf die genaue Pulsmodellierung sind.

Abstract

The ongoing upgrade activities at the Large Hadron Collider aim for an increase of the luminosity in the particle collisions. The increased luminosity delivers new capabilities for precision measurements and searches for signatures of new physics. At the same time, challenges arise for the experiments. For this reason, the ATLAS detector is upgraded. The focus is on maintaining the high efficiency of the trigger that selects interesting physics events in real-time. Therefore, the Liquid-Argon calorimeter of the ATLAS detector is upgraded with new readout electronics.

To evaluate the performance, a demonstrator readout was installed and operated in parallel to the data taking of the main readout between 2014 and 2018. In this thesis, the data recorded with the demonstrator is analyzed. The new readout electronics allow more sophisticated algorithms to distinguish between signal and background events. They are based on variables that describe electromagnetic and hadronic showers. The proposed shower-shape variables are studied concerning their trigger efficiency and background rejection power. With a combination of the shower-shape variables, a background rejection power of 75 % for hadronic jets is achieved while keeping the electron trigger efficiency at 90 %.

The increase in luminosity will lead to an increase in in-time and out-of-time pile-up effects. These have an impact on the energy reconstruction. Therefore, pile-up events are investigated, to gain precise knowledge about their effects.

For the energy reconstruction of the detector signals, different digital filter algorithms are available. The signal detection efficiency of these algorithms is examined. While new filter algorithms are capable of reducing the effect of out-of-time pile-up, they depend greatly on the correct phase of the pulse shape.

Contents

1. Introduction	1
2. Physics Motivation	3
2.1. The Standard Model of Particle Physics	3
2.1.1. Fundamental Interactions	4
2.1.2. Matter Particles	6
2.2. Verifications of the Standard Model and Challenges	8
2.3. Extensions to the Standard Model	8
3. Experimental Setup	11
3.1. The Large Hadron Collider	11
3.2. The ATLAS Detector	15
3.2.1. The Coordinate System	15
3.2.2. Variables in the Transverse Plane	17
3.2.3. The Magnet System	18
3.2.4. The Inner Detector	18
3.2.5. The Calorimeter System	20
3.2.6. The Muon Spectrometer	21
3.2.7. The Trigger System and Data Acquisition	23
3.3. Physics at the Large Hadron Collider	25
4. The Liquid-Argon Calorimeter	31
4.1. Energy Measurement Working Principal	31
4.2. Structure of the Liquid-Argon Calorimeter	33
4.2.1. Barrel Geometry	35
4.2.2. End-Cap Geometry	36
4.3. Readout Electronics	39
4.3.1. Front-End Electronics	39
4.3.2. Back-End Electronics	41
4.4. Level-1 Calorimeter Trigger	43

5. Upgrade Plans	45
5.1. Upgrades of the Large Hadron Collider	45
5.2. The Phase-I Upgrade of the ATLAS Detector	47
5.3. Upgrade of the Liquid-Argon Calorimeter	47
5.3.1. Supercells	47
5.3.2. Upgrade of the Front-End Electronics	49
5.3.3. Upgrade of the Back-End Electronics	52
5.3.4. Upgrade of the Level-1 Calorimeter Trigger	53
5.3.5. Shower Shape Variables	53
5.4. Demonstrator System of the Phase-I Upgrade of the Trigger Readout Electronics	58
6. Digital Processing of Liquid-Argon Calorimeter Signals	63
6.1. Pulse Shapes of the Liquid-Argon Calorimeter	63
6.2. Sources of Noise	66
6.3. Digital Filter Algorithms	68
6.3.1. Finite Impulse Response Filter	68
6.3.2. Infinite Impulse Response Filter	68
6.4. Optimal Filter	69
6.5. Wiener Filter	72
6.6. Wiener Filter with Forward Correction	73
7. Preparation of Liquid-Argon Demonstrator Data	75
7.1. Trigger Coverage	75
7.2. The Datasets	77
7.2.1. Dataset of the Main Readout	77
7.2.2. Dataset of the LAr Demonstrator	78
7.3. Energy Reconstruction	79
7.4. Preparation for the Data Analysis	81
7.4.1. Pedestal Value Adjustment	81
7.4.2. Peak Sample Identification	82
7.5. Irregular Signals	84
8. Studies of the Shower-Shape Variables	87
8.1. Particle Identification	87
8.2. Matching of Main Readout and Demonstrator Data	88
8.3. Energy Distribution of the Hottest Supercell	93
8.4. Studies of the Shower-Shape variable R_η	95

8.5. Studies of the Shower-Shape variable f_3	99
8.6. Studies of the Shower-Shape variable $w_{\eta,2}$	103
8.7. Trigger Efficiency Performance of the Shower-Shape Variables	105
8.8. Conclusion	107
9. Pile-Up Analysis	109
9.1. BCID Assignment and Examined Range	110
9.2. Pile-Up Energy Spectrum	110
9.3. Pile-Up Baseline Shift	113
9.4. Studies of the Bunch-Train Beginning	118
9.4.1. Development of the Average Pile-Up Energy during a Run . . .	118
9.4.2. Correlation between Pile-Up Energy and μ	120
9.5. Conclusion	122
10. Wiener Filter Studies	123
10.1. Pulse Shape Comparison	123
10.2. Studies on the Wiener Filter with Forward Correction	125
10.3. Studies on the Wiener Filter	129
10.4. Conclusion	132
11. Conclusion and Outlook	133
A. Appendix	135
A.1. Calibration Runs	135
A.2. Additional Plots of the Shower-Shape Variables Study	139
List of Figures	143
List of Tables	147
Glossary	149
Bibliography	153

1. Introduction

What is our universe made of and which forces drive its development? These questions have driven humankind from time immemorial. Particle physicists are particularly keen to answer them. In the last century, a theory emerged that combines the elementary particles and three out of the four fundamental forces, the Standard Model of Particle Physics [1–5]. An introduction to this theory and the motivation for the studies of this thesis are given in chapter 2.

To study subatomic particles and verify the predictions of the Standard Model, very high energies are necessary. The most powerful particle accelerator ever built is the Large Hadron Collider (LHC) [6, 7] at the European Organization for Nuclear Research (CERN). Here, particles are brought to collision with energies never achieved before. The particles that emerge from these collisions are observed with particle detectors like the ATLAS detector [8]. In chapter 3, the LHC and the ATLAS detector are introduced. Calorimeters are used for the energy measurement of particles. In chapter 4, a description of the Liquid-Argon (LAr) calorimeter of the ATLAS detector is given.

The discovery of the Higgs boson in 2012 [9, 10] is the most recent verification of the predictions of the Standard Model and exemplifies the first, very successful runs of the LHC. Nevertheless, the Standard Model cannot describe all phenomena. To improve the search for signatures of physics beyond the Standard Model, precise measurements of the Standard Model parameters and searches for new phenomena are necessary. For this, the LHC follows an ambitious upgrade schedule. It foresees an increase in luminosity for Run 3 starting in 2021. To cope with the challenges of an increased luminosity and exhaust its capabilities, the ATLAS detector is upgraded as well. In chapter 5, an overview of the Phase-I upgrade [11] of the ATLAS detector is given. It includes the installation of new readout electronics for the Level-1 (L1) trigger readout of the LAr calorimeter. This upgrade is crucial for keeping a high efficiency for selecting interesting physics events while suppressing background to a level which the trigger system can cope with. The new trigger readout electronics of the LAr calorimeter will allow more sophisticated algorithms for the selection of

signal and background events of the particle collisions. For this, a precise energy reconstruction with digital filter algorithms is important. In chapter 6, the processing of LAr calorimeter signals is described.

For the evaluation of the performance of the new readout electronics, a demonstrator readout was installed and operated during Run 2 of the LHC. This demonstrator already provides all features of the future trigger readout system. In particular, event sequences can be studied in detail over longer time intervals, which was not possible before. The data taken with this demonstrator are analyzed in this thesis. In chapter 7, the preparation of the data for the analysis is presented. The shower-shape variables that will allow distinguishing between signal and background events are studied in chapter 8. The increase in luminosity leads to an increase in pile-up effects, which have an impact on the energy reconstruction. Therefore, precise knowledge about pile-up is vital. In chapter 9, the effects of pile-up on the signal and energy reconstruction are investigated. For the reconstruction of the energy, a selection of different filter algorithms is available. In chapter 10, the advantages and disadvantages of new digital filter algorithms are discussed.

2. Physics Motivation

In this chapter, the current state of particle physics is introduced. First is a review of the Standard Model of Particle Physics¹ in section 2.1. Followed by a short overview of the successes and shortcomings of this theory in section 2.2. Section 2.3 gives an overview of extensions of the Standard Model, which motivate further searches at the LHC.

2.1. The Standard Model of Particle Physics

The Standard Model [1–5] provides a theory that comprises the understanding of particle physics as of today. It describes three out of the four fundamental interactions², electromagnetism, the strong interaction, and the weak interaction. Furthermore, it includes the elementary particles.

The Standard Model classifies as elementary particles all particles that do not have a substructure. They can be grouped into two categories according to their spin. Bosons have integer spin and obey Bose-Einstein statistics [12]. Spin-1 bosons are referred to as the force carriers. Fermions with half-integer spin obey Fermi-Dirac statistics [13, 14] and are called matter particles. Fermions can be further classified into quarks, q , which couple to all three forces, charged leptons, ℓ^\pm , which do not interact via the strong force, and neutrinos, ν , which only couple to the weak force.

There are many well-written books on the Standard Model, e.g. [15–19]. The following sections are a summary of the key features which are presented in detail in these books.

¹The Standard Model of Particle Physics is referred to as Standard Model throughout this thesis.

²The fourth fundamental interaction is gravity, which in comparison to the other three interactions is too weak to play an important role in LHC physics, and is therefore not included in the Standard Model.

2.1.1. Fundamental Interactions

The Standard Model is a relativistic quantum field theory whose Lagrangian fulfills a set of global symmetries, connected by Noether's theorem [20]. The invariance under the transformation of time, space, and rotation leads to the conservation of energy, momentum, and angular momentum. Additionally, the Standard Model is based on a local gauge symmetry group $SU(3)_C \times SU(2)_L \times U(1)_Y$. The invariance under transformations related to this group leads to the conservation of color charge, weak isospin, and weak hypercharge. To fulfill the invariance under local gauge transformations, gauge fields need to be introduced into the Lagrangian. Excitations of these gauge fields can be interpreted as gauge bosons.

Electroweak Interaction

In the 1960s, Glashow, Salam, and Weinberg unified electromagnetism and the weak interaction to the electroweak interaction [1–3]. The electroweak interaction is based on a $SU(2)_L \times U(1)_Y$ symmetry group. The corresponding charges are the weak isospin, T , for $SU(2)_L$ and the hypercharge, Y , for $U(1)_Y$.

To fulfill gauge invariance under $SU(2)_L$ transformations, three gauge fields W_μ^1 , W_μ^2 , and W_μ^3 are introduced. For gauge invariance under $U(1)_Y$ transformations, a gauge field B_μ is introduced. In experiments, these gauge fields are not observed, but mixings of them.

The charged gauge fields W_μ^\pm of the weak interaction are a linear combination of W_μ^1 and W_μ^2 :

$$W_\mu^\pm = \frac{W_\mu^1 \mp iW_\mu^2}{\sqrt{2}}. \quad (2.1)$$

The gauge fields W_μ^3 and B_μ mix to the neutral field, Z_μ , of the weak interaction and the gauge field, A_μ , of electromagnetism:

$$\begin{pmatrix} Z_\mu \\ A_\mu \end{pmatrix} = \begin{pmatrix} \cos \theta_W & -\sin \theta_W \\ \sin \theta_W & \cos \theta_W \end{pmatrix} \begin{pmatrix} W_\mu^3 \\ B_\mu \end{pmatrix} \quad (2.2)$$

where θ_W is the Weinberg angle, which is connected to the coupling constants g_w of $SU(2)_L$ and g_Y of $U(1)_Y$:

$$\sin \theta_W = \frac{g_Y}{\sqrt{g_w^2 + g_Y^2}}. \quad (2.3)$$

The resulting gauge fields W_μ^\pm , Z_μ , and A_μ are still massless. The reason is that the electroweak theory does not allow elementary particles to have a mass due to local gauge invariance. Yet, observations show that the gauge bosons of the weak interaction and the fermions are massive.

Electroweak Symmetry Breaking

This conflict is resolved by the Higgs mechanism [21–25]. It introduces a scalar Higgs field with a degenerate ground state with a non-vanishing vacuum expectation value. This ground state spontaneously breaks the electroweak gauge symmetry leading to $SU(2)_L \times U(1)_Y \rightarrow U(1)_Q$.

Electromagnetism

The unbroken symmetry group $U(1)_Q$ is the symmetry group of electromagnetism. The charge, Q , is related via

$$Q = T_3 + \frac{1}{2}Y \quad (2.4)$$

to the third component of the weak isospin, T_3 , and the hypercharge.

Electromagnetism is described by Quantum Electrodynamics (QED) [26]. The local gauge field is the above mentioned A_μ . It can be interpreted as the photon field. The gauge boson of electromagnetism, the photon, γ , is massless. Therefore, the range of electromagnetic interactions is infinite. The photon does not carry any charge hence there is no self-interaction.

Weak Interactions

The decay of quarks and leptons can be explained by the theory of weak interactions [27]. In contrast to the photon, the three mediators of the weak interaction W^\pm and Z^0 are massive. Furthermore, the weak interaction is unique for its parity violation as it only couples to left-handed fermions.

Strong Interactions

The strong interaction is described by Quantum Chromodynamics (QCD) [28–31]. The Lagrangian of the strong interaction is invariant under $SU(3)_C$ transformations. Here, C denotes the charge of the strong interaction, color. It comes in three types, denoted by red, green, and blue. Eight massless gluons, g , mediate the strong interaction. They carry a color and anti-color charge themselves, which leads to gluons coupling to other gluons.

The strong interaction possesses two particular features. At very short distances, the coupling constant of the strong interaction becomes tiny. That leads to quarks and gluons behaving like quasi-free particles and is called asymptotic freedom. The second feature is called confinement. It explains why one cannot observe single quarks.

When trying to separate two quarks, the force between them increases. If the energy is sufficient, a quark-antiquark pair is produced. Hence, only zero net color states are observable, called hadrons.

2.1.2. Matter Particles

As mentioned before, fermions have half-integer spin and are referred to as the matter particles. They can be further divided into quarks and leptons. There are six quarks that carry color, weak, and electromagnetic charge. The electromagnetic charge comes in multiples of $\frac{1}{3}e$, where e is the elementary charge. The quarks are grouped into three families, being up, u , and down, d , strange, s , and charm, c , and top, t , and bottom, b , quark. The six leptons do not carry a color charge which implicates that they do not interact via the strong interaction. They can be further divided into the electrically charged leptons, electron, e , muon, μ , and tau, τ , and the electric neutral neutrinos (ν_e, ν_μ, ν_τ). Like the quarks, leptons can be grouped into three families. Each of them is composed of an electrically charged lepton and the corresponding neutrino. Additionally, each fermion has a corresponding antiparticle with an opposite charge, but the same mass.

In fig. 2.1, an overview of the elementary particles of the Standard Model is given.

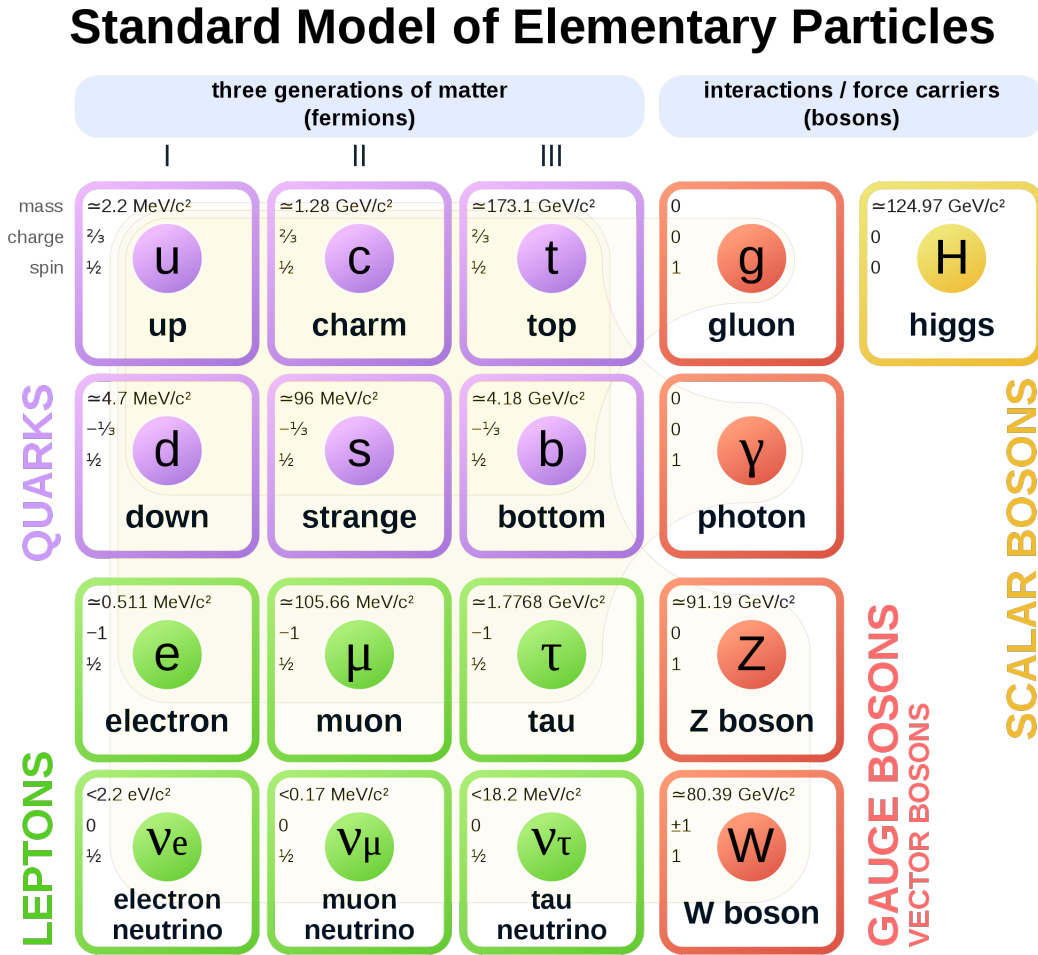


Figure 2.1.: The elementary particles of the Standard Model [32]. In the left three columns, the fermions (purple and green) are summarized according to their families. Their couplings to the bosons (red) are indicated in light brown. Additionally, the mass, the electric charge, and the spin are stated for each particle.

2.2. Verifications of the Standard Model and Challenges

The Standard Model is very successful in explaining experimental results. Many predictions of the Standard Model have been experimentally confirmed. Namely, gluons which are described by QCD were discovered in 1979 at the German Electron Synchrotron (DESY)³ [33–36]. In 1983, the gauge bosons predicted by the electroweak theory W^- , W^+ [37, 38], and Z^0 [39] have been observed at the Super Proton–Antiproton Synchrotron at the CERN⁴. And being one of the most recent discoveries, the Higgs boson has been detected in 2012 at the LHC [9, 10].

Still, the Standard Model does not explain all physical phenomena. As already mentioned, it does not incorporate gravitation as described by general relativity [40]. Also, according to the original version of the Standard Model neutrinos should be massless. But neutrino-oscillations have been observed [41, 42], which require a neutrino mass. Furthermore, the matter we know accounts only for 5% of the content of the universe. The rest, dark matter and dark energy, with 27% and 68% respectively, are not explained by the Standard Model [43]. And finally, there is the matter-antimatter asymmetry which means that there is an imbalance between matter and antimatter in the universe [44]. The observed CP -violation⁵ is not strong enough to explain this asymmetry.

2.3. Extensions to the Standard Model

The above-mentioned phenomena that are not explained by the Standard Model lead to the assumption that there is physics beyond the Standard Model [45]. Various theories exist that either extend the Standard Model or provide new explanations for these phenomena.

One of the theories that extend the Standard Model is supersymmetry. Supersymmetry relates half-integer spin particles, fermions, with integer spin particles, bosons, and vice versa. For each elementary particle of the Standard Model exists a superpartner whose spin differs by $\frac{1}{2}$ unit. As for the nomenclature, the spin-0 partners of fermions are prepended with an s , e.g. squarks (short for scalar quarks) and sleptons (scalar leptons). The spin- $\frac{1}{2}$ partners of bosons are appended with an $-ino$, e.g. gauginos. Yet, no superpartners with the same mass and quantum numbers are observed. As a consequence, supersymmetry must be broken resulting in different masses of the

³Deutsches Elektronen-Synchrotron

⁴Conseil européen pour la recherche nucléaire

⁵ CP is the symmetry of charge conjugation and parity.

superpartners [46, 47].

So far, there are no signals of physics beyond the Standard Model in the experimental searches at the LHC. A reason could be that the new particles have larger masses than covered by the LHC, which would require a new particle collider with higher center-of-mass energy. Another reason could be that the cross-sections are below the current sensitivity, which will be improved through more accumulated luminosity [48].

The search for signatures of new physics with improved sensitivity is the goal of LHC and ATLAS runs in the next decade, and the reason for the detector upgrade.

3. Experimental Setup

The data that are analyzed in this thesis were recorded by the ATLAS detector at the LHC. In this chapter, the experimental setup is introduced. Section 3.1 gives an overview of the LHC, its structure, and a short run history. In section 3.2, the ATLAS detector is outlined. In section 3.3, physics processes at the LHC are explained that are of importance to this thesis.

3.1. The Large Hadron Collider

The LHC [6, 7] is used to accelerate and collide particles at four interaction points. It was built by CERN. The LHC is installed in a nearly circular tunnel near Geneva, Switzerland, at the Franco-Swiss border. It is the last part of a chain of particle accelerators (see fig. 3.1). The tunnel is in a depth of 45–170 m below the surface and has a circumference of 26.7 km. It was formerly used for the Large Electron Positron Collider [49].

The LHC is designed as a synchrotron with two beam pipes where the particles travel in opposite directions. The design center-of-mass energy for proton-proton (pp) collision is $\sqrt{s} = 14$ TeV and $\sqrt{s} = 5.5$ TeV per nucleon pair for lead nuclei. The LHC is not a perfect circle but consists of eight straight sections and eight arcs. To bend the beams, 1232 superconducting dipole magnets are installed at the arcs. They are cooled by liquid helium to 1.9 K and have magnetic fields with a strength of 8.33 T to keep the beams on their circular path. Also, there are quadrupole magnets to focus the beams and higher-order magnets for further corrections installed.

The protons are not spread continuously in the beams but packed in bunches with a time spacing of $\Delta t_{\text{BC}} = 25$ ns between the bunches. That leads to a bunch-crossing frequency of:

$$f_{\text{BC}} = \frac{1}{t_{\text{BC}}} = 40 \text{ MHz}. \quad (3.1)$$

Each of these bunches can contain up to 1.15×10^{11} protons.

3. Experimental Setup

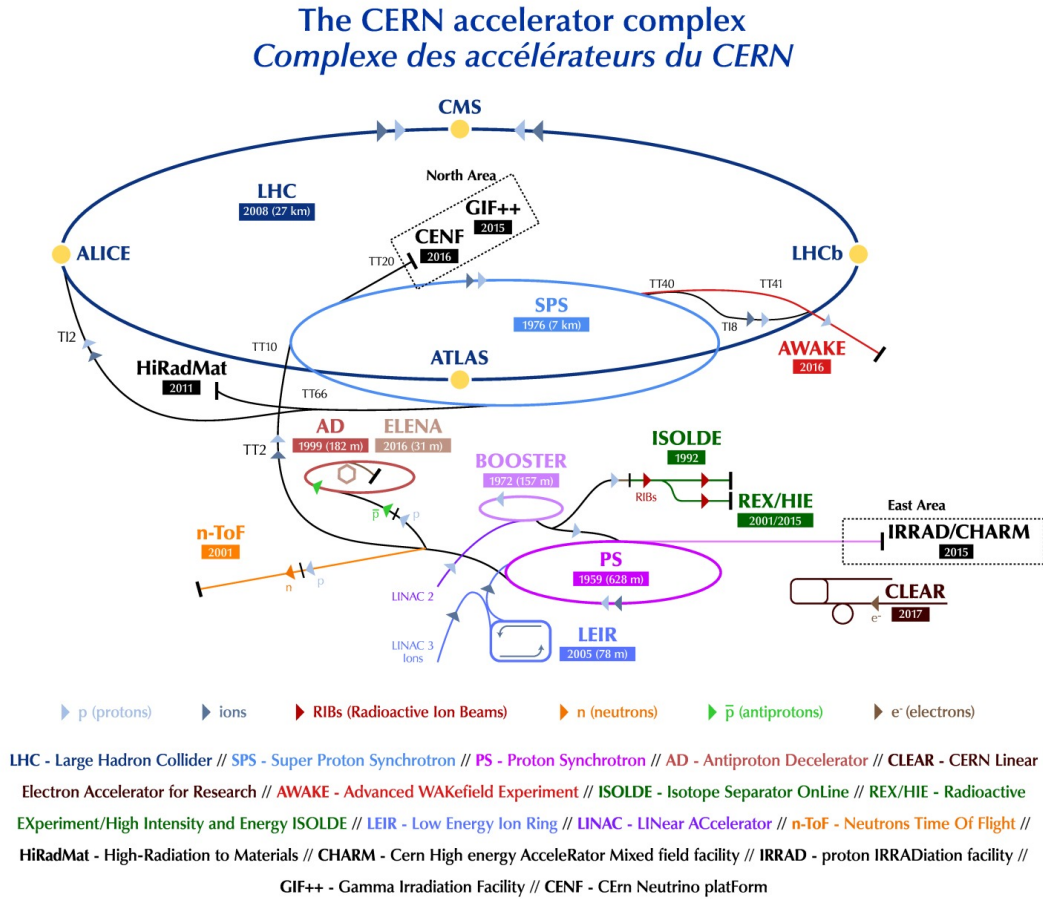


Figure 3.1.: Overview of the CERN accelerator complex [50]. The LHC is the last part of a chain of particle accelerators.

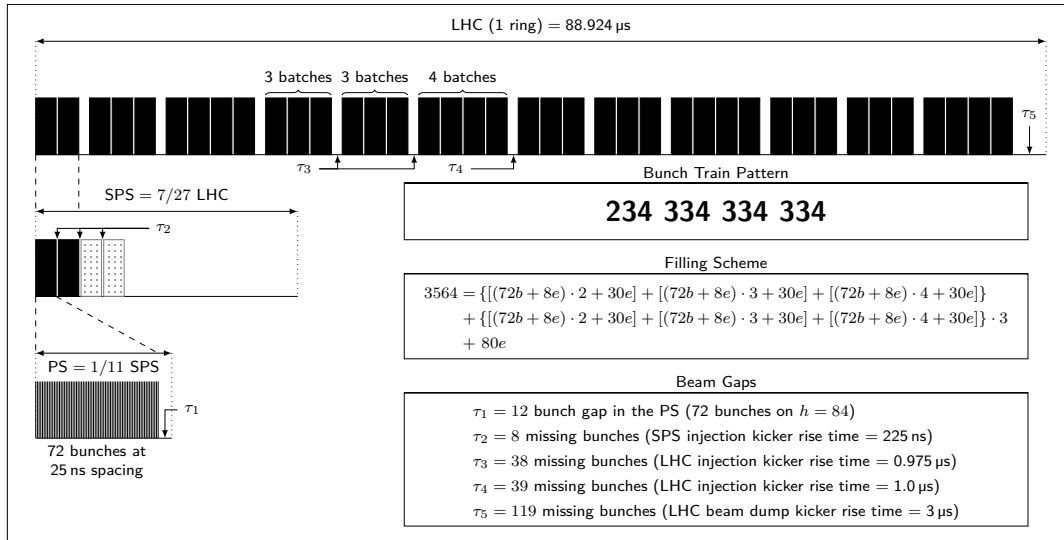


Figure 3.2.: Schematic view of the 25 ns filling scheme for high luminosity [51].

Not all of the 3564 possible bunches are filled during operation. The LHC has different filling schemes for various operation modes [51]. For high luminosity production, the 25 ns filling scheme is used (see fig. 3.2). In this scheme, the bunches are arranged in 39 batches of 72 bunches¹. That results in a total of 2808 filled bunches. More details on the other filling schemes can be found in [51].

Besides the center-of-mass energy, the instantaneous luminosity, L , is an important parameter for a particle collider. The instantaneous luminosity is defined as:

$$L = \frac{N_b^2 n_b f_{\text{rev}} \gamma_r}{4\pi \epsilon_n \beta^*} F, \quad (3.2)$$

where N_b^2 is the number of protons per bunch, n_b is the number of bunches per beam, f_{rev} is the revolution frequency, γ_r is the relativistic factor of protons, F is the geometric correction factor due to the crossing angle at the interaction point, ϵ is the normalized transverse beam emittance, and β^* is the beta function at the interaction point.

The LHC was designed to deliver an instantaneous luminosity of $L = 10^{34} \text{ cm}^{-2} \text{ s}^{-1}$. To get the rate at which certain processes occur, the instantaneous luminosity is

¹A bundle of consecutively filled bunches is called bunch train.

3. Experimental Setup

multiplied by the corresponding cross-section σ :

$$\frac{dN}{dt} = L \cdot \sigma. \quad (3.3)$$

The integrated luminosity, L_{int} , gives the total number of events in a certain time interval:

$$L_{\text{int}} = \int L dt. \quad (3.4)$$

It quantifies the amount of collision data that are collected by an experiment over a given time, t .

At the mentioned interaction points, the four main experiments are installed:

- The ALICE experiment [52] studies the collisions of heavy ions, in particular lead nuclei, to address the physics of strongly interacting particles and quark-gluon plasma at extremely high temperatures and densities.
- The LHCb experiment [53] focuses on b -physics, namely measurements of CP -violation and rare decays of b -hadrons.
- The two multi-purpose detectors, the ATLAS experiment [8] and the CMS experiment [54], are designed to measure Standard Model parameters, study the properties of the Higgs boson, which was discovered by these two experiments in 2012 [9, 10], and search for physics beyond the Standard Model.

The ATLAS detector is described in section 3.2.

In September 2008, the first beams were steered around the LHC [55]. Shortly after the start, there was an incident that caused a one-year break to repair the resulting damage [56]. The beams were back in November 2009 [57]. In March 2010, an energy of 3.5 TeV per beam was achieved [58] and exceeded in April 2012 with 4 TeV per beam [59]. During this period of data taking, the so-called Run 1 (2009–2013), an integrated luminosity of $L_{\text{int}} = 6.1 \text{ fb}^{-1}$ at a center-of-mass energy of 7 TeV and 23.1 fb^{-1} at 8 TeV was recorded [60]. The data-taking stage was followed by a two-year period, the Long Shutdown 1, for maintenance work on the accelerator and the detectors. The operation restarted in April 2015 [61] delivering collisions with a center-of-mass energy of 13 TeV to the experiments [62]. During Run 2, an integrated luminosity of $L_{\text{int}} = 4.0 \text{ fb}^{-1}$, 38.5 fb^{-1} , 50.2 fb^{-1} , and 63.4 fb^{-1} at a center-of-mass energy of 13 TeV was recorded for the years 2015–2018 [63]. Run 2 ended

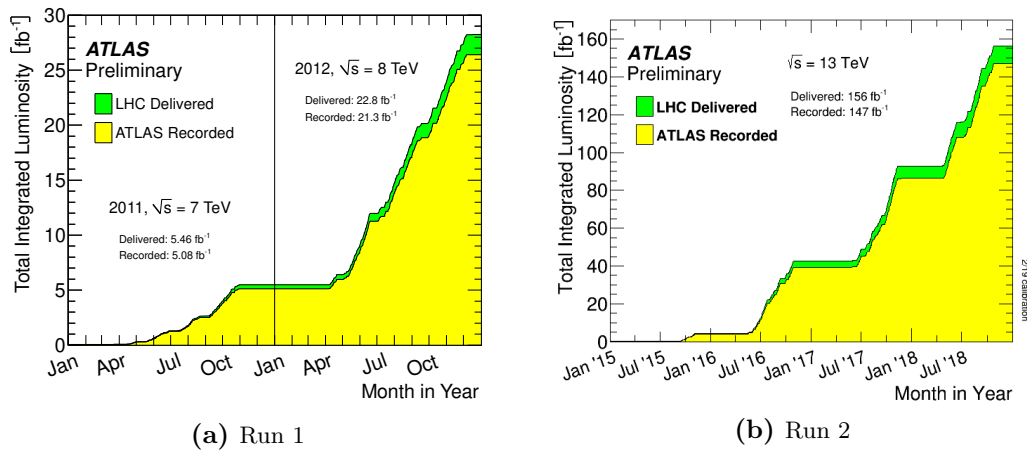


Figure 3.3.: Total integrated luminosity for Run 1 [65] and Run 2 [66]. In green is the delivered luminosity by LHC and in yellow the recorded luminosity by ATLAS.

in December 2018 followed by the ongoing Long Shutdown 2 [64]. The LHC will presumably resume operation in 2021 with Run 3.

In fig. 3.3, an overview of the integrated luminosities for Run 1 and Run 2 is shown.

3.2. The ATLAS Detector

The ATLAS detector [8] is a general-purpose detector built for studying particle collisions. With dimensions of 25 m in diameter and a length of 44 m, it is the largest detector at the LHC. It weighs approximately 7000 t. The ATLAS detector is constructed in layers around the interaction point. With the inner detector being closest to the interaction point, surrounded by the calorimeters and the muon spectrometer. In this section, a brief overview of the different parts of the ATLAS detector is given. A more detailed description can be found in [8]. In fig. 3.4, a general layout of the ATLAS detector is shown. In table 3.1, the performance goals for the different detector components are given.

3.2.1. The Coordinate System

ATLAS uses a right-handed Cartesian coordinate system with its origin being at the interaction point. The positive direction of the x -axis points from the interaction point towards the center of the LHC, while the positive direction of the y -axis is

3. Experimental Setup

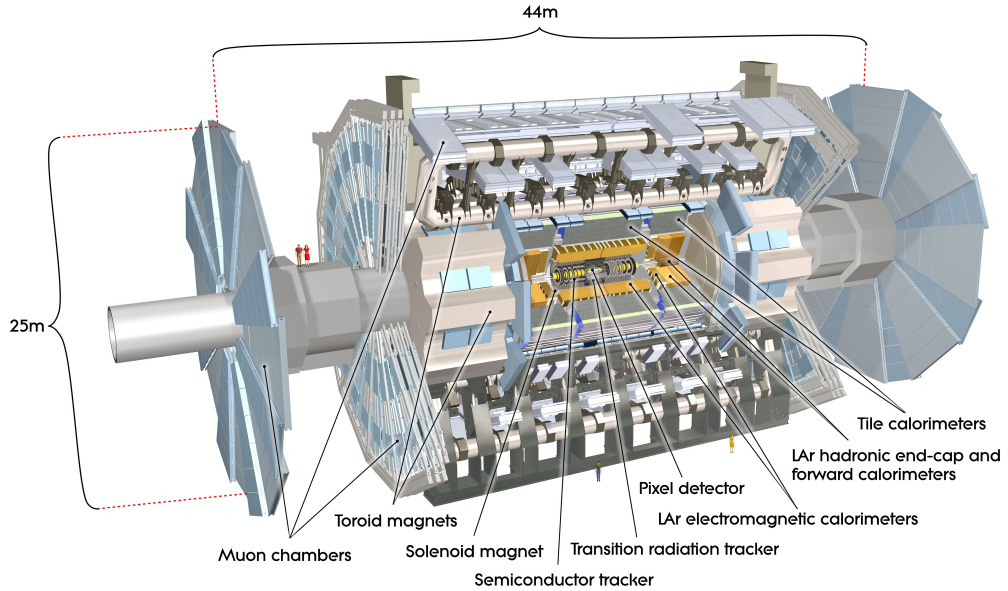


Figure 3.4.: Schematic overview of the ATLAS detector [8].

Table 3.1.: General performance goals of the ATLAS detector [8]. The requirements of the hadronic calorimeter are given for jets. For high- p_T muons, the performance of the muon spectrometer is independent of the tracking system. The units for energy, E , and transverse momentum, p_T , are given in GeV.

Detector component	Required resolution	η coverage	
		Measurement	Trigger
Tracking	$\sigma_{p_T}/p_T = 0.05\% p_T \oplus 1\%$	± 2.5	
EM calorimeter	$\sigma_E/E = 10\%/\sqrt{E} \oplus 0.7\%$	± 3.2	± 2.5
Hadronic calorimeter			
barrel and end-cap	$\sigma_E/E = 50\%/\sqrt{E} \oplus 3\%$	± 3.2	± 3.2
forward	$\sigma_E/E = 100\%/\sqrt{E} \oplus 10\%$	3.1–4.9	3.1–4.9
Muon spectrometer	$\sigma_{p_T}/p_T = 10\%$ at $p_T = 1$ TeV	± 2.7	± 2.4

defined to point upwards from the interaction point. The z -axis points in the direction of the beam. That results in the x - y plane being transverse to the beam direction. The ATLAS detector is divided into two sides, where the positive z is side- A and the negative z is side- C .

Commonly, spherical coordinates are used with the polar angle, θ , measured with respect to the z -axis, and the azimuthal angle, ϕ , measured in the x - y plane relative to the x -axis. The polar angle, θ , is often replaced by the pseudorapidity, η , which is defined as:

$$\eta = -\ln \tan\left(\frac{\theta}{2}\right). \quad (3.5)$$

Differences in pseudorapidity, $\Delta\eta$, are Lorentz invariant under boosts in the direction of the beam axis. The spatial separation between two particles in the η - ϕ space is measured with:

$$\Delta R = \sqrt{(\Delta\eta)^2 + (\Delta\phi)^2}. \quad (3.6)$$

3.2.2. Variables in the Transverse Plane

In pp collisions at the LHC, the elementary particles that form a proton, the so-called partons (quarks and gluons), interact². Since the exact positions and momentum fraction of these partons are not measurable, the rest frame of each interaction is unknown. That is the reason for introducing variables defined in the plane transverse to the beam direction.

The transverse momentum is Lorentz invariant under boosts in the direction of the beam axis:

$$p_T := \sqrt{p_x^2 + p_y^2} = |\mathbf{p}| \cdot \sin \theta. \quad (3.7)$$

Despite the energy being a scalar quantity and hence independent of direction a transverse energy is introduced:

$$E_T := E \cdot \sin \theta. \quad (3.8)$$

Two more quantities are used in particle physics. The scalar sum of all measured transverse energies:

$$E_T^{\text{sum}} := \sum_i E_{T,i}. \quad (3.9)$$

In the case of the ATLAS detector, it is summed up over all detector cells.

²For more on this see section 3.3.

3. Experimental Setup

The second quantity is the negative of the vector sum of all measured transverse energies:

$$\vec{E}_T^{\text{miss}} := - \sum_i \begin{pmatrix} E_T \times \cos \phi_i \\ E_T \times \sin \phi_i \end{pmatrix} = - \begin{pmatrix} E_{x,i} \\ E_{y,i} \end{pmatrix}. \quad (3.10)$$

Again, it is summed up over all detector channels of the ATLAS detector.

The magnitude of this vector is called missing transverse energy:

$$E_T^{\text{miss}} = |\vec{E}_T^{\text{miss}}| = \sqrt{\left(\sum_i E_{x,i}\right)^2 + \left(\sum_i E_{y,i}\right)^2}. \quad (3.11)$$

It is the sum of the energies of particles that leave the detector without interaction, which are mainly neutrinos.

3.2.3. The Magnet System

The purpose of the magnet system of the ATLAS detector is to bend the tracks of charged particles on their way through the detector in order to measure their transverse momentum. It consists of four superconducting magnets, one solenoid and three toroids. The central solenoid [67] generates an axial magnetic field of 2 T for the inner detector. The three toroids, one in the barrel region and two in the end-caps, provide a toroidal magnetic field of 0.5 T (barrel) and 1 T (end-caps) for the muon spectrometer. In fig. 3.5, an overview of the layout of the magnet system is shown.

3.2.4. The Inner Detector

The purpose of the inner detector [68, 69] is to record the tracks of charged particles that emerge at the interaction point. Therefore, it is installed nearest to the beam pipe and extends up to a radius of 1.15 m. The inner detector is embedded in the central solenoid. The magnetic field of the solenoid bends the tracks of the charged particles as they cross the inner detector. Examining the curvature of a bent track allows a determination of the charge and the momentum of the particle. The inner detector is composed of three detectors. In fig. 3.6, an overview of the layout of the inner detector is shown.

The innermost part of the inner detector is the pixel detector [70, 71]. For the detector material, silicon pixels are used. Each pixel has a size of $50 \mu\text{m} \times 400 \mu\text{m}$. They are arranged in three cylindrical layers and three disks on each side of the

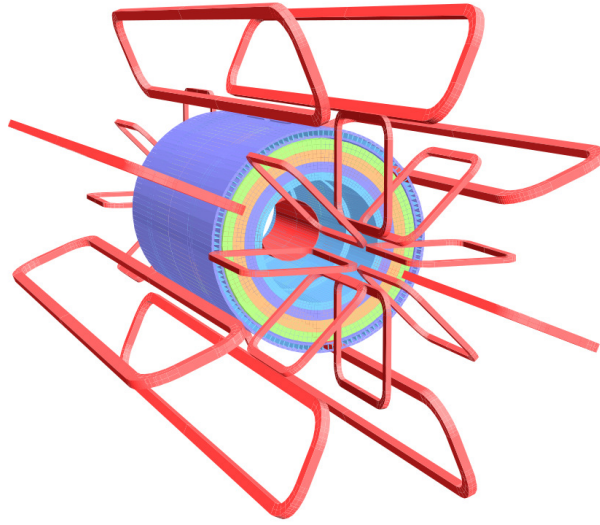


Figure 3.5.: Schematic overview of the ATLAS detector magnet system [8]. The parts of the magnet system are marked in red. There are eight barrel toroid coils, and eight end-cap toroid coils per side. In the center, the solenoid windings are depicted.

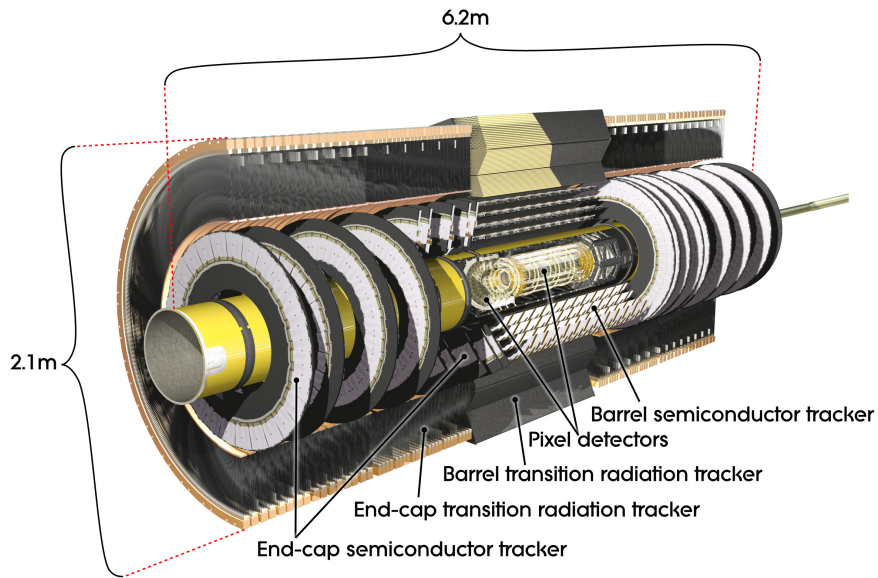


Figure 3.6.: Schematic overview of the inner detector of the ATLAS detector [8].

3. Experimental Setup

detector and cover a range of $|\eta| < 2.5$. In total, there are over 80 million readout channels.

During the Long Shutdown 1, the insertable B-layer [72] was installed. Therefore, the beam pipe had to be replaced to get the insertable B-layer as close as 33.25 mm to the beam. The pixels of the insertable B-layer have a size of $50 \mu\text{m} \times 250 \mu\text{m}$. The insertable B-layer has about 6 million additional channels.

Surrounding the pixel detector is the semiconductor tracker [73]. It consists of four cylindrical layers and nine disks on each detector side, and also covers a range of $|\eta| < 2.5$. The structure of the semiconductor tracker is similar to that of the pixel detector, but instead of pixels, silicon strips are used. In total, the semiconductor tracker has about 6.3 million readout channels.

The transition-radiation tracker [74] is the outermost part of the inner detector. It consists of drift tubes with a diameter of 4 mm. These tubes are arranged in numerous layers in a barrel and two end-cap parts and cover a range of up to $\eta = 2.0$. Resulting in an average of 36 hits per particle track. The drift tubes are filled with a xenon-based gas mixture³. In between the drift tubes, polypropylene fibers and foils are installed as the transition-radiation material. The transition radiation that is emitted when charged particles cross the border between two materials with different dielectric constants allows separating electrons from charged pions according to their relativistic γ factor. The transition-radiation tracker has about 351 000 readout channels.

3.2.5. The Calorimeter System

The ATLAS calorimeter system consists of the LAr calorimeter [76] and the Tile calorimeter [77]. They cover a range of $|\eta| < 4.9$. In fig. 3.7, an overview of the calorimeters is shown. As the main subject of this thesis, the LAr calorimeter is discussed in detail in chapter 4.

The Tile calorimeter is a sampling calorimeter. For the absorber, steel is used and scintillating tiles are the active material. It consists of three parts: the barrel covers $|\eta| < 1.0$ and the two extended barrels cover $0.8 < |\eta| < 1.7$. The Tile calorimeter is arranged in three layers in depth of different thicknesses. In terms of interaction lengths⁴, λ , the layers of the barrel are 1.5λ , 4.1λ , and 1.8λ thick, and the layers of

³Due to large, irreparable gas leaks, some parts of the transition-radiation tracker are filled with an argon-based gas mixture [75].

⁴The mean free path of a particle between two interactions.

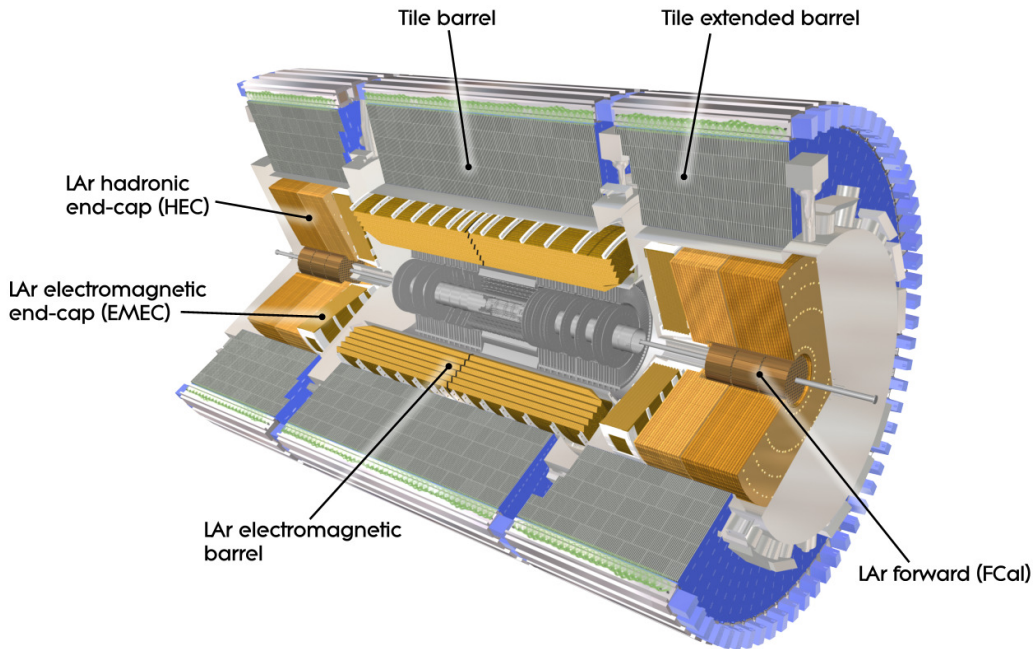


Figure 3.7.: Schematic overview of the calorimeter of the ATLAS detector [8].

the extended barrels 1.5λ , 2.6λ , 3.3λ , respectively. The Tile calorimeter has more than 9800 readout channels.

3.2.6. The Muon Spectrometer

The muon spectrometer [78] is the outermost part of the ATLAS detector. In fig. 3.8, an overview of the structure is shown. The purpose of the muon spectrometer is to record charged particles that exit the calorimeters, which are mainly muons. Therefore, the tracks are bent by the magnetic fields of the three toroids. The barrel toroid bends the tracks in a region of $|\eta| < 1.4$, the two end-cap toroids in a region of $1.6 < |\eta| < 2.7$, respectively. In the transition region ($1.4 < |\eta| < 1.6$), the tracks are bent by a combination of the magnetic fields of the barrel and end-cap toroids.

The tracks are measured in chambers which are arranged in three cylindrical layers in the barrel and three planes perpendicular to the beam axis in the end-caps. These

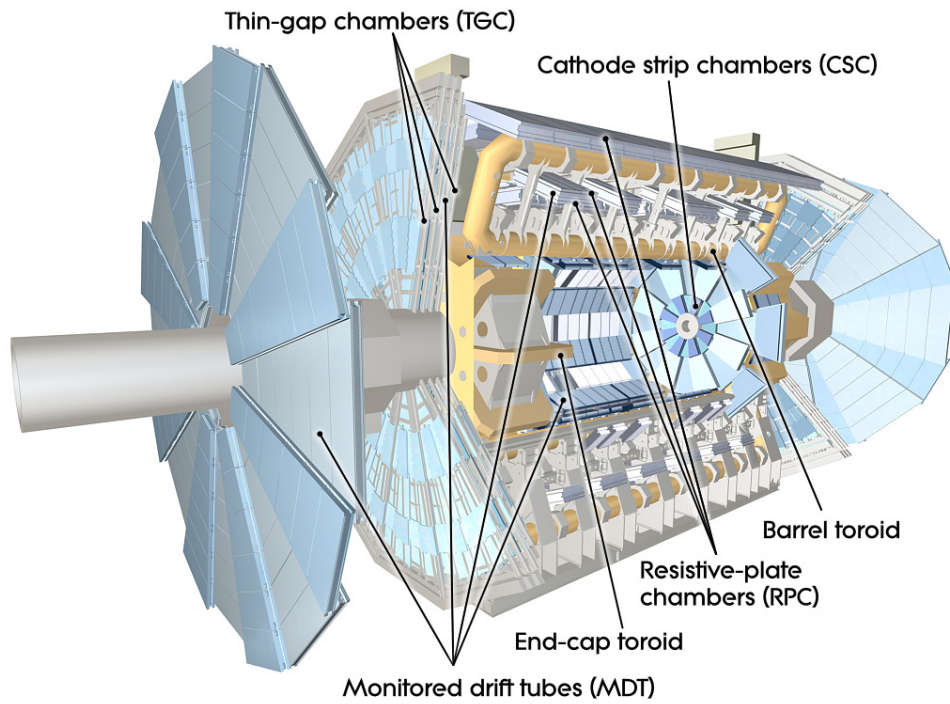


Figure 3.8.: Schematic overview of the muon spectrometer of the ATLAS detector [8].

are mainly monitored-drift tubes that are installed in a range of $|\eta| < 2.7$. Only in the innermost layer of the planes ($2.0 < |\eta| < 2.7$) cathode-strip chambers are used.

For the muon trigger ($|\eta| < 2.4$), different chambers are used. In the barrel region, resistive-plate chambers are installed in a range of $|\eta| < 1.05$. For the end-cap region, thin-gap chambers cover the range of $1.05 < |\eta| < 2.7$. In total, the muon spectrometer has more than 1 million readout channels.

3.2.7. The Trigger System and Data Acquisition

With a bunch-crossing frequency of 40 MHz, the LHC produces a large number of pp collisions each second. Due to the technical capabilities of data storage, it is not possible to record all events that are registered by the ATLAS detector [79]. In addition, the cross-section of events that are interesting for physics studies is rather low (see section 3.3). Therefore, to decrease the number of events that are recorded they are selected based on the signatures they leave in the detector.

The Trigger and Data Acquisition (TDAQ) system [8] is responsible for the selection and recording of the events. During Run 1, the trigger system had three levels, the L1 trigger, the Level-2 (L2) trigger, and the event filter. Between Run 1 and Run 2, it received an upgrade combining the L2 trigger and the event filter to the high-level trigger [80, 81]. Resulting in a two-level trigger system. In fig. 3.9, an overview of the structure is shown.

The first level is the L1 trigger which is realized in custom-built hardware [83]. It identifies regions-of-interest and sends the corresponding information to the next trigger stage. The decision to accept an event is taken by the central trigger processor which receives information from three subsystems.

The Level-1 Calorimeter (L1Calo) trigger takes information from the calorimeters with a coarser granularity. It is discussed in more detail in section 4.4.

The Level-1 Muon (L1Muon) trigger uses information from the resistive-plate chambers in the barrel region and the thin-gap chambers in the end-cap region. The new Level-1 Topological (L1Topo) trigger [84] was installed before Run 2. It finds specific topologies that interesting physics objects leave in the detector. For making a decision, the L1 trigger has less than $2.5 \mu\text{s}$, reducing the rate from 40 MHz to 100 kHz.

The second stage is the high-level trigger which is realized in software running on commercial hardware. It applies algorithms that are similar to the offline reconstruc-

3. Experimental Setup

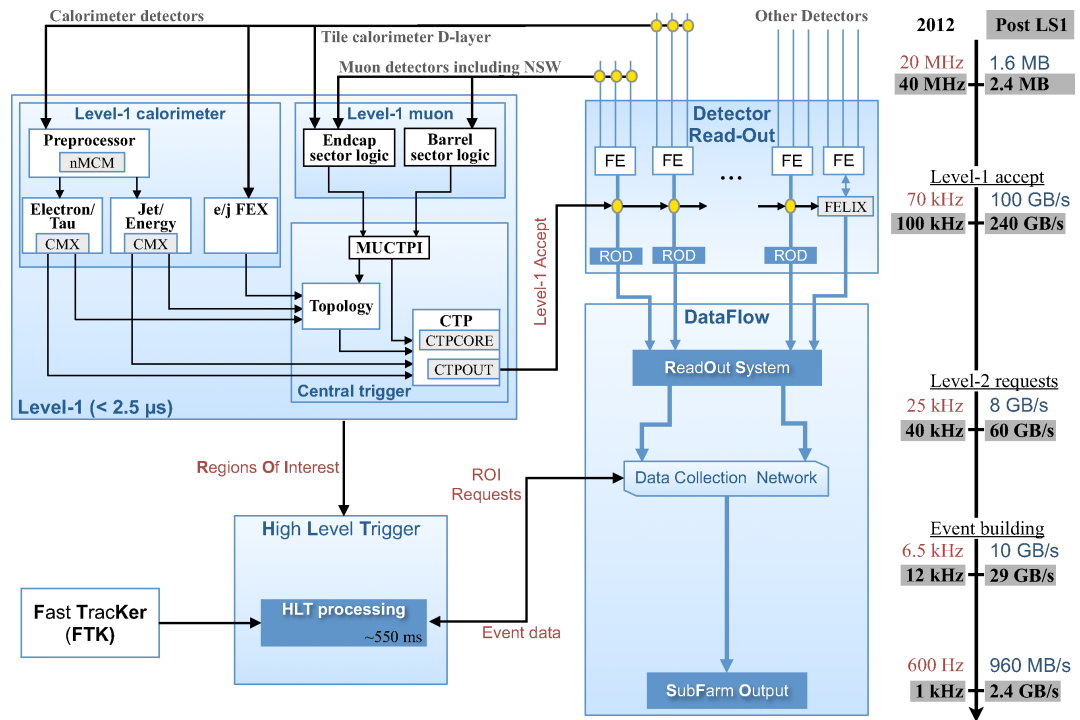


Figure 3.9.: Schematic overview of the Run 2 configuration of the TDAQ system [82].

tion on the regions-of-interest, or the full event information. To take a decision, it has a processing time of 0.2s. The average recording rate of the high-level trigger is 1 kHz.

3.3. Physics at the Large Hadron Collider

As described in section 3.1, at the LHC bunches of protons are brought to collision. A collision between two protons can either be elastic or inelastic. In the case of an elastic collision, both protons stay intact.

Inelastic collisions can be further divided into single and double diffractive, and non-diffractive events. In single diffractive events, one proton gets excited to a higher mass state while the other proton stays intact. This process does not change the quantum numbers of the proton and the excited proton returns to its stable ground state afterward. In the case of a double diffractive event, both protons get excited [85].

For inelastic interactions, it has to be considered that protons are not elementary particles⁵. Therefore, to explain inelastic collisions between protons Feynman introduced the so-called parton model [87]. In the parton model, a proton can be understood as being composed of point-like constituents (quarks q and gluons g), called partons. Thus, an inelastic pp collision can be described by partons colliding. At the interaction points of the LHC, different physics processes can occur when these partons collide depending on the cross-section of the process. In fig. 3.10, an overview of the total production cross-sections for different processes is given.

Measurements show that the total cross-section of inelastic pp collisions increases with the center-of-mass energy, \sqrt{s} [89]. This has been already predicted by Heisenberg in 1952 [90]. In fig. 3.11, measurements from the ATLAS detector and other hadron collider experiments are compared to the predictions of different event generators.

Inelastic pp collision can either be soft or hard depending on the momentum transfer. Usually, the momentum transfer is low, and the soft interactions are predominant. But the hard interactions with high momentum transfer are the ones of interest. Both hard and soft interactions can be explained by QCD, but the degree of understanding of hard and soft interactions is different. Describing hard interactions, the perturbative QCD delivers predictions with high precision. Soft interactions, on the other hand, are less well understood and cannot be described by perturbation theory.

⁵A proton consist of two up and one down quark, called the valence quarks, and an infinite sea of quark-antiquark pairs, called sea quarks [86].

3. Experimental Setup

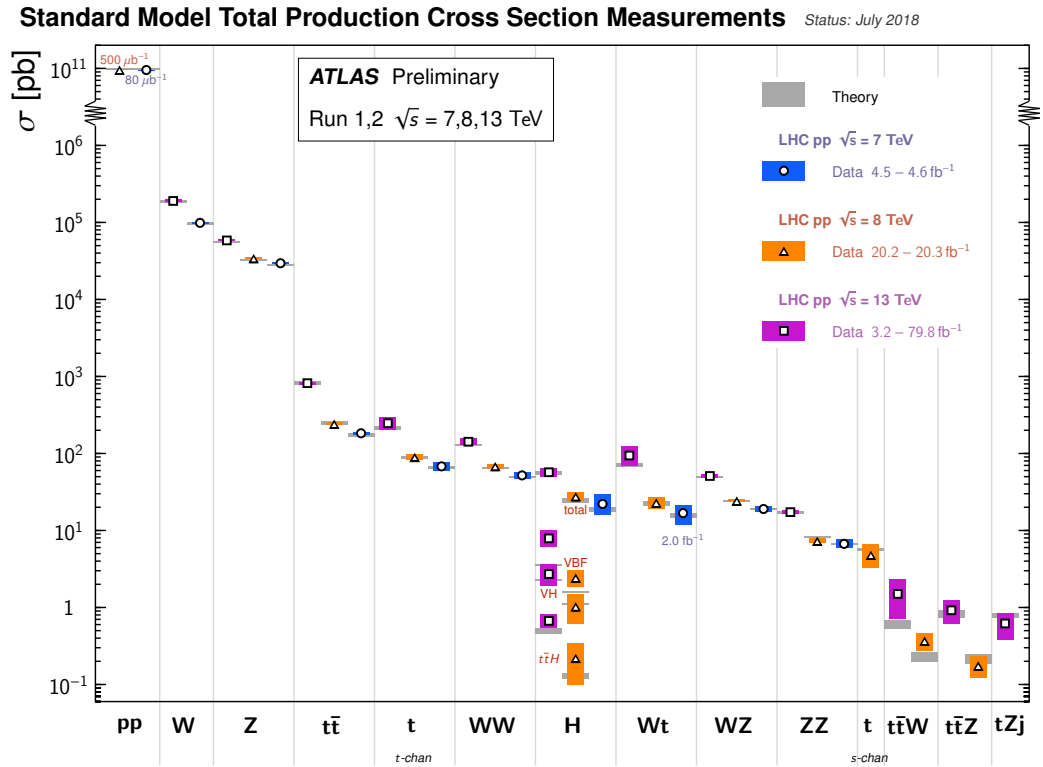


Figure 3.10.: Overview of the Standard Model total production cross-section measurements at the ATLAS detector. Theoretical predictions are compared to the measured cross-sections [88].

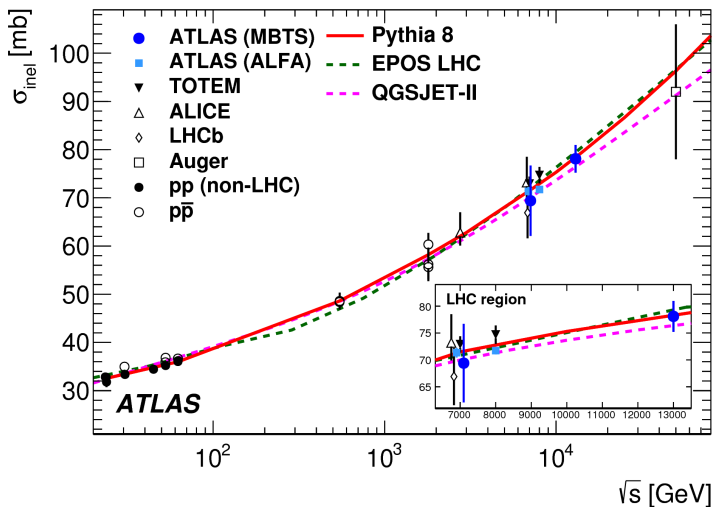


Figure 3.11.: Cross-section of inelastic pp collisions as a function of \sqrt{s} [89]. The measured data from several experiments are compared to various predictions from event generators.

The non-perturbative processes of soft interactions have to be modeled. Many hard interactions do not occur alone but are superimposed by soft interactions. Therefore, it is crucial to understand soft interactions [91].

In fig. 3.12, an exemplary inelastic collision simulated with SHERPA [92] is shown. Besides the hard interaction, other processes occur which are explained in the following.

When objects that carry a color charge are accelerated, Bremsstrahlung can occur. If the emission of a gluon is associated with an incoming parton it is called initial-state radiation, for outgoing partons, it is called final-state radiation [94]. These gluons can form parton showers. Meaning, that the gluons split into $q\bar{q}$ or gg pairs which can, in turn, emit gluons again [95].

Beam remnants are partons that do not take place in the hard interaction. Either they interact with other remnants or keep moving in the beam direction. Interactions between remnants are called multiple parton interactions. Beam remnants and multiple parton interactions are summarized as underlying events [96].

At the interaction points, when the two beams are crossed and the bunches collide, usually more than one pp collision occurs. In fact, the number of pp collisions per bunch crossing denoted with the Greek letter μ was on average 33.7 for the data

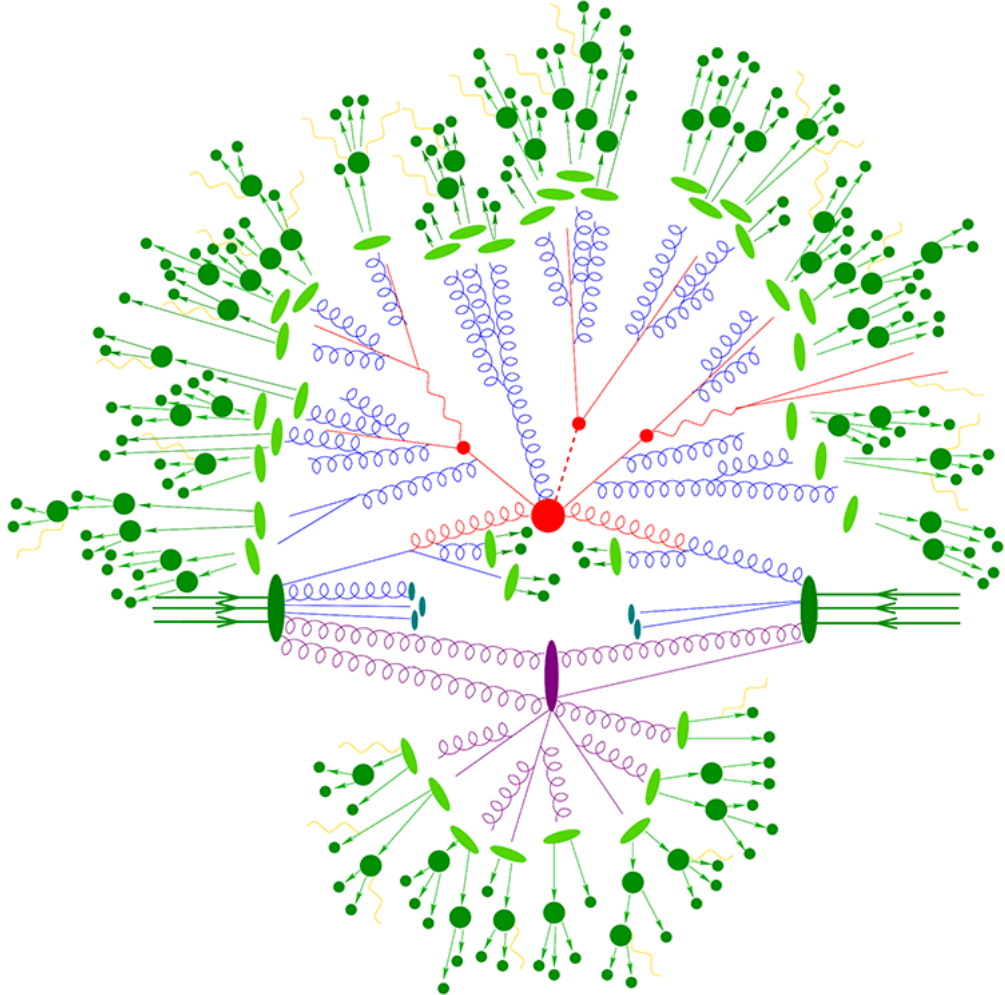


Figure 3.12.: Exemplary inelastic pp collision at the LHC simulated with SHERPA [93]. In red, the hard scattering process of interest is marked. Multiple parton interactions are indicated in purple. Partons can emit Bremsstrahlung (blue) and hadronize (light-green). If a hadron is unstable it decays (dark-green). QED-Bremsstrahlung is marked in yellow.

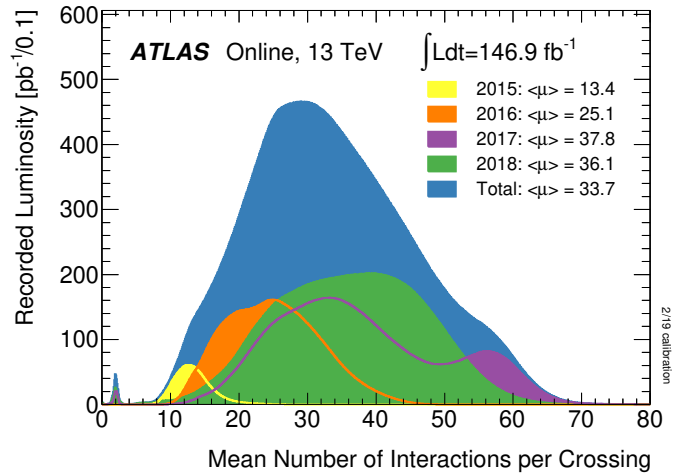


Figure 3.13.: Luminosity-weighted distribution of the average number of interactions per bunch crossing for the years 2015–2018 [97]. Additionally, the integrated luminosity of the reference period and the μ for each year is indicated. All data were recorded at a center-of-mass energy of 13 TeV.

taking in the years 2015–2018 at 13 TeV (see fig. 3.13). These overlapping events are called pile-up. There are two different types of pile-up. If the interactions happen in the same bunch crossing, it is called in-time pile-up. If detector pulses of events from consecutive bunch crossings overlap, it is called out-of-time pile-up. Pile-up, in general, poses a major challenge to the energy reconstruction which is discussed in section 6.2.

A term that is closely related to pile-up is the minimum-bias event. Minimum-bias events are events that fulfill a minimum set of criteria to make sure an inelastic pp collision took place. Therefore, this strongly depends on how the trigger of an experiment is set up. In the case of ATLAS, minimum-bias events are predominantly soft interactions with low transverse momentum [98].

4. The Liquid-Argon Calorimeter

This chapter introduces the LAr calorimeter [76] of the ATLAS detector. The LAr calorimeter consists of the Electromagnetic Barrel Calorimeter (EMB) in the barrel region. Furthermore, in both end-caps, an Electromagnetic End-Cap Calorimeter (EMEC), a Forward Calorimeter (FCal), and a Hadronic End-Cap Calorimeter (HEC) are situated. In section 4.1, the important physics processes for energy measurement are described, followed by the structure of the LAr calorimeter in section 4.2. In section 4.3 and section 4.4, the readout system and the trigger system are introduced, respectively.

4.1. Energy Measurement Working Principal

Calorimeters are used to measure the energies of electromagnetically interacting particles, mainly electrons¹ and photons but also hadrons. They work in a way that the particles are fully absorbed inside the calorimeter, while the energy deposition is measured. An explanation of calorimeters for particle physics can be found in [99]. The following section refers to this document focusing on those parts which are of importance for this thesis.

There are two types of calorimeters, homogeneous and sampling calorimeters. Homogeneous calorimeters are made of a single type of material. The LAr calorimeter is a sampling calorimeter consisting of active and passive material. In a sampling calorimeter, the passive material serves as the absorber. An incident particle interacts (via electromagnetic or strong interaction) with the absorber and produces secondary particles with lower energies. This process repeats itself resulting in a so-called particle shower. The energy deposited in the active material generates a signal which is a measure of the energy of the particle. In the case of a homogeneous calorimeter, a single material serves both purposes.

The LAr calorimeter, as the name states, uses liquid argon as the active material. For the absorber, three different kinds of materials are used, copper, lead, and tungsten.

¹What is said about electrons also applies for positrons.

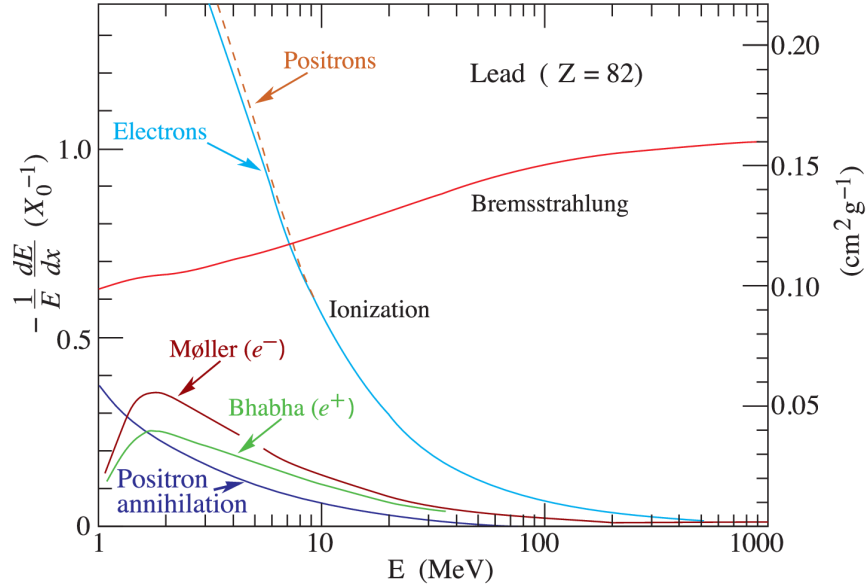


Figure 4.1.: Energy loss per radiation length X_0 of electrons and positrons in lead depending on their energy [100]. For high energies Bremsstrahlung, is dominating while for lower energies ionization is predominant.

Electrons and photons initiate an electromagnetic shower when they interact with the detector. An overview of the interactions between particles and matter can be found in [100]. These interactions are of statistical nature. For high energies, electrons mainly induce Bremsstrahlung. At the critical energy, E_C , this process is superseded by ionization which dominates for low energies. For photons, pair production (e^+e^-) is predominant for high energies, while Compton scattering and the photoelectric effect prevail for low energies.

A parameter which is closely related to the longitudinal and lateral size of an electromagnetic shower is the radiation length, X_0 . It depends on the characteristics of the material [100]. For electrons, X_0 gives the range at which they reduce their energy to $1/e$ of the initial energy. Photons reduce their energy to $1/e$ of the initial energy after traveling a distance of $\frac{9}{7}X_0$.

In fig. 4.1, the energy loss of electrons in lead is shown. In addition, the predominant processes as a function of energy are displayed.

As mentioned above, the detector signal is generated in the active material. When charged particles go through the liquid-argon layer, they ionize it and produce electron-ion pairs. If an electric field is applied, the electrons and ions drift in different directions. The drifting electrons induce a current in the readout electrode. This current produces a triangular signal with a sharp rising edge and a long declining slope. The pulse length corresponds to the drift time of electrons in liquid argon given the electric field [101].

Since a part of the energy is deposited in the absorber material, only a fraction of the energy of the incident particle is measured. The sampling fraction, f_{samp} , accounts for that. It is calculated with

$$f_{\text{samp}} = \frac{E_{\text{active}}}{E_{\text{absorber}} + E_{\text{active}}}, \quad (4.1)$$

where E_{active} is the energy that is deposited in the active material, and E_{absorber} is the energy that is deposited in the absorber. Therefore, to get the actual energy of the particle the measured energy has to be divided by f_{samp} .

The relative energy resolution of a calorimeter can be written as the quadratic sum

$$\frac{\sigma}{E} = \frac{a}{\sqrt{E}} \oplus \frac{b}{E} \oplus c. \quad (4.2)$$

The three terms are in order of appearance, the stochastic term, the noise term, and the constant term.

The stochastic term accounts for statistical fluctuations in the shower development. While the fluctuations are small for homogeneous calorimeters, they pose the major limitation to the energy resolution in sampling calorimeters. The noise term accounts for the electronics noise, the quantization noise, and the pile-up noise. The constant term does not depend on energy. It accounts for contributions from non-uniformities in the calorimeter coming e.g. from mechanical structures or the readout electronics.

4.2. Structure of the Liquid-Argon Calorimeter

The LAr calorimeter is made of three separate cryostats, one barrel and two end-caps. The barrel cryostat houses the EMB. In each end-cap cryostat, an EMEC, a HEC, and an FCal are placed. All parts use liquid argon as active material which is cooled down to an operating temperature of 87 K [102]. In total, the LAr calorimeter has more than 182 000 readout channels. In fig. 4.2, an overview of the LAr calorimeter is shown.

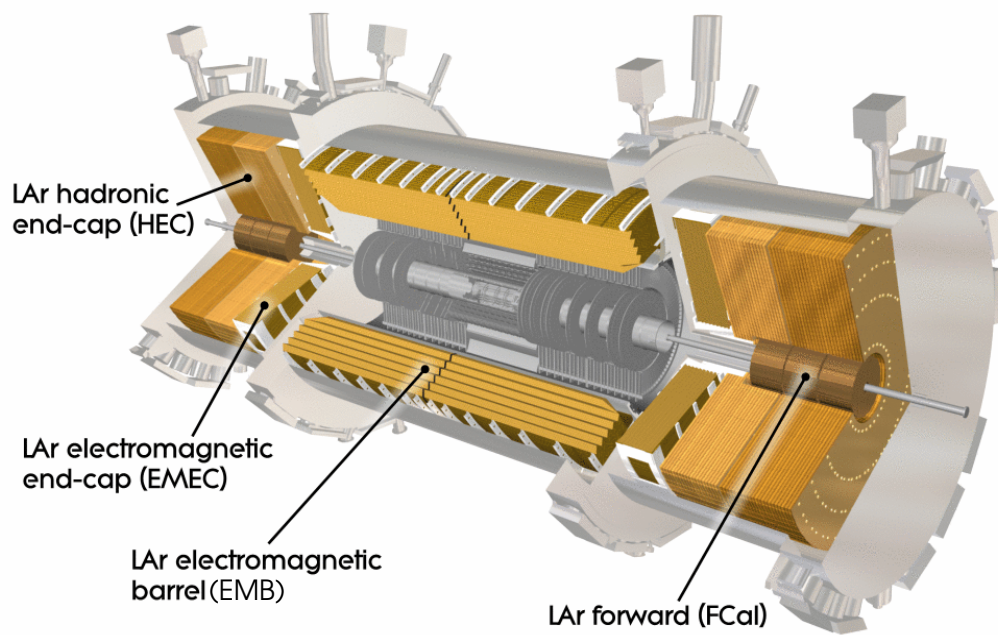


Figure 4.2.: Schematic overview of the LAr calorimeter [103].

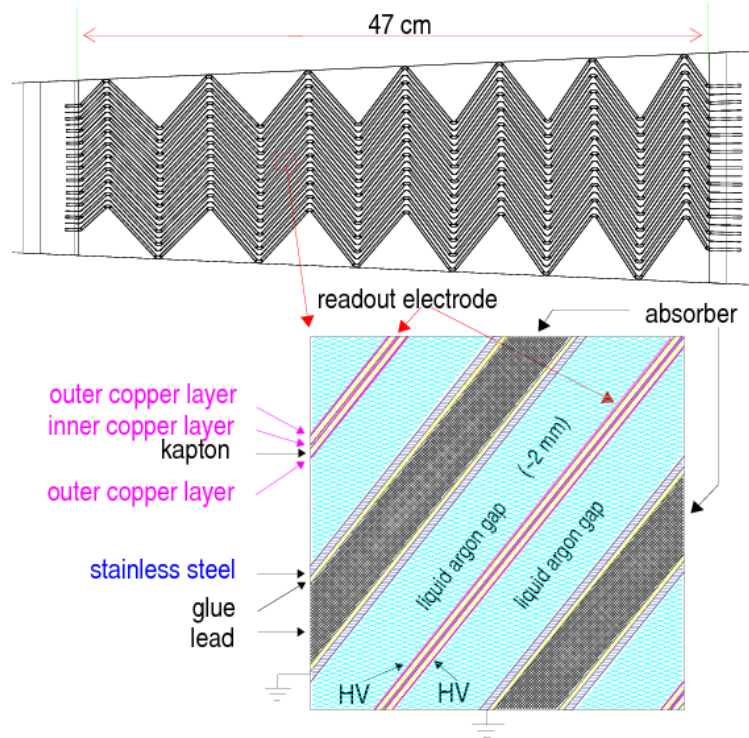


Figure 4.3.: The accordion geometry of the EMB [101]. In the upper part, a slice of the EMB transverse to the beam line is shown. In the lower part, an enlarged section is displayed to show the arrangement of the absorber, the active material, and the electrodes.

In the EMB and the EMECs, the absorber and electrodes are arranged in an accordion geometry. This shape has been chosen to guarantee full ϕ coverage without any cracks. Furthermore, it makes sure that particles cross multiple layers of active and absorber material when traversing the ATLAS detector. In the upper part of fig. 4.3, an overview of the accordion geometry in the EMB is depicted. In the lower part, the structure of the liquid-argon gaps is shown.

4.2.1. Barrel Geometry

The EMB, that is installed in the barrel cryostat, consists of two half barrels. They are separated at $z = 0$ with a small 4 mm crack. In the EMB, lead is used as absorber material. The accordion waves of the EMB are parallel to the axial direction. To

Table 4.1.: Overview of the cell sizes of the different detector layers of the EMB [8].

	Cell Size ($\Delta\eta \times \Delta\phi$)	Coverage
Presampler	0.025×0.1	$ \eta < 1.52$
Front Layer	$0.025/8 \times 0.1$	$ \eta < 1.4$
	0.025×0.025	$1.4 < \eta < 1.475$
Middle Layer	0.025×0.025	$ \eta < 1.4$
	0.075×0.025	$1.4 < \eta < 1.475$
Back Layer	0.075×0.025	$ \eta < 1.35$

keep the gap size between the absorber layers constant, the angles of the accordion structure vary with the radius.

The EMB is separated into three layers in depth. To estimate the energy that is lost in the material in front of the electromagnetic calorimeter, an additional layer, the presampler, is installed. The detector layers differ in the size of the cells that are read out through the electrodes. In fig. 4.4, the segmentation of the barrel in three layers is shown. In table 4.1, a summary of the different cell sizes as a function of η is given.

The depth of the EMB in radiation lengths is between $22 X_0$ and $33 X_0$. In fig. 4.5a, the thickness of the different detector layers of the EMB is shown as a function of η .

4.2.2. End-Cap Geometry

The calorimeters in the end-cap cryostats have different absorber materials. While the EMECs use lead, as the EMB does, for the HECs and the front part of the FCals copper serves as the absorber. In the two back parts of the FCals, tungsten is installed.

The EMECs are separated into two coaxial wheels, an outer wheel ($1.375 < |\eta| < 2.5$) and an inner wheel ($2.5 < |\eta| < 3.2$). Like in the EMB, an accordion geometry is used in the EMECs. But in contrast to the EMB, the accordion waves run parallel to the radial direction and the gap sizes are not constant.

For the outer wheel of the EMEC, there are three different detector layers in depth. In the range of $|\eta| < 1.8$, there is an additional presampler layer. The inner wheel only consists of two detector layers in depth. In table 4.2, a summary of the different cell sizes is given.

The thickness in radiation lengths varies for the EMECs from $24\text{--}38 X_0$ for the outer

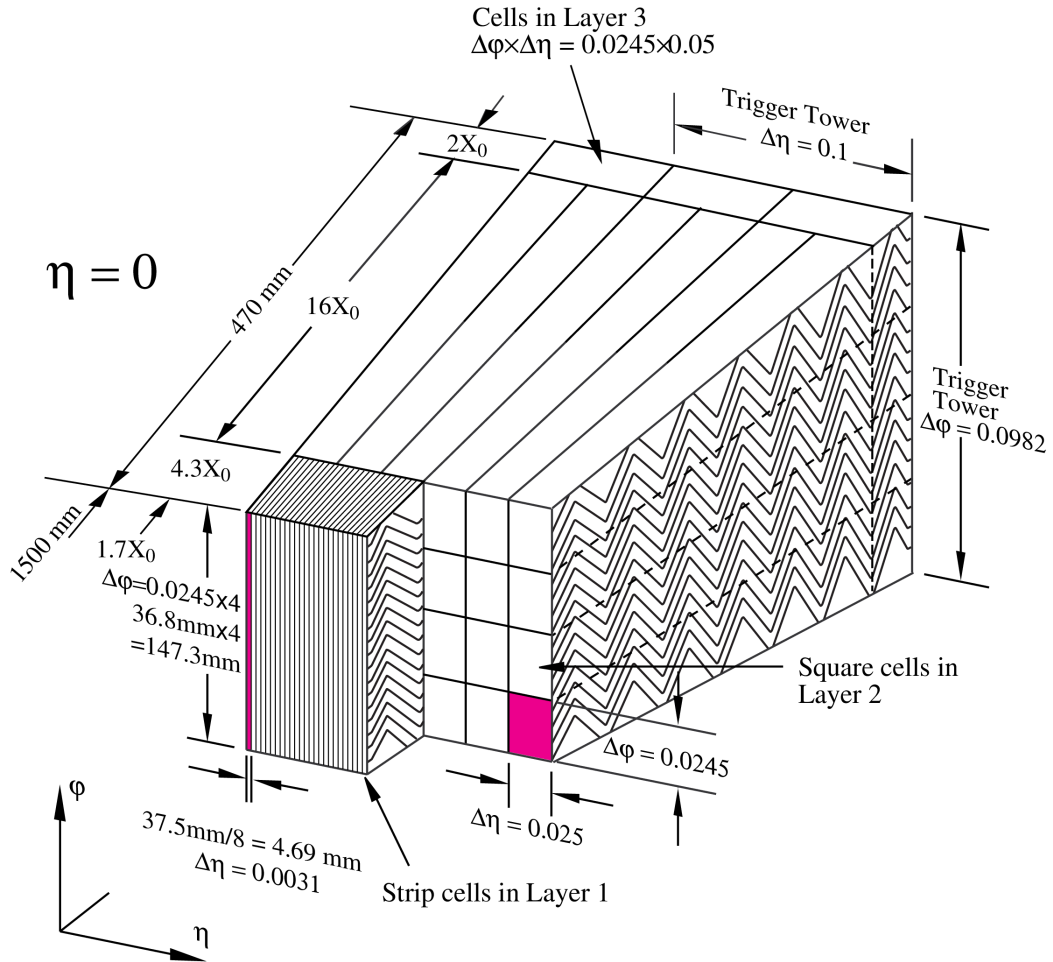


Figure 4.4.: Segmentation of the EMB for $\eta = 0$ in three layers [8]. The different cell sizes and the accordion geometry are indicated.

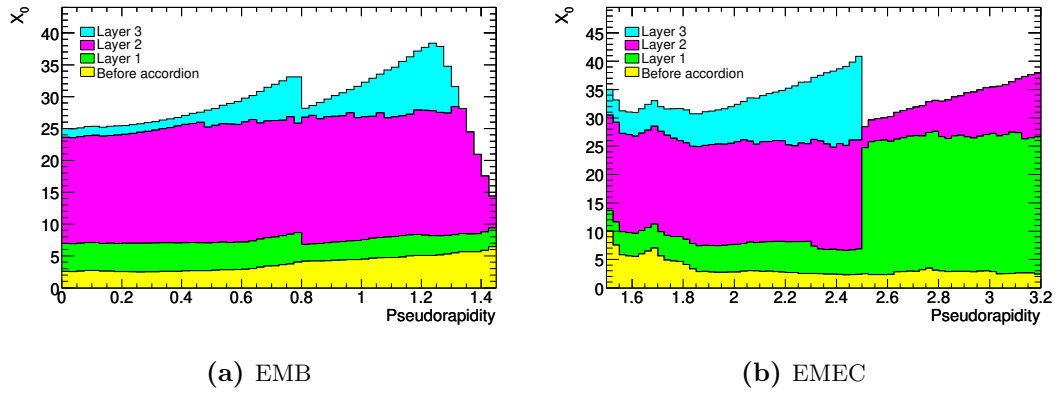


Figure 4.5.: The total amount of material in radiation lengths X_0 for the EMB and the EMEC as a function of η [8]. The three different detector layers are depicted in different colors. The presampler is pooled with the material that is in front of the LAr calorimeter.

Table 4.2.: Overview of the cell sizes of the different detector layers of the EMEC [8].

	Cell Size ($\Delta\eta \times \Delta\phi$)	Coverage
Presampler	0.025×0.1	$1.5 < \eta < 1.8$
Front Layer	0.050×0.1	$1.375 < \eta < 1.425$
	0.025×0.1	$1.425 < \eta < 1.5$
	$0.025/8 \times 0.1$	$1.5 < \eta < 1.8$
	$0.025/6 \times 0.1$	$1.8 < \eta < 2.0$
	$0.025/4 \times 0.1$	$2.0 < \eta < 2.4$
	0.025×0.1	$2.4 < \eta < 2.5$
Middle Layer	0.1×0.1	$2.5 < \eta < 3.2$
	0.050×0.025	$1.375 < \eta < 1.425$
	0.025×0.025	$1.425 < \eta < 2.5$
Back Layer	0.1×0.1	$2.5 < \eta < 3.2$
	0.050×0.025	$1.5 < \eta < 2.5$

wheel and $26\text{--}36 X_0$ for the inner wheel. In fig. 4.5b, the thickness of the different detector layers of the EMEC as a function of η is shown.

4.3. Readout Electronics

The readout electronics of the LAr calorimeter are divided into the front-end electronics and the back-end electronics. In fig. 4.6, an overview of the readout electronics is given.

4.3.1. Front-End Electronics

The front-end electronics [104] of the LAr calorimeter consist of four different boards. They are installed on the detector in the Front-End Crates (FECs).

- The calibration board is used to inject high precision pulses into the readout chain. The calibration pulses do not have the characteristic triangular shape. Still, the shape is close to the detector signal. The difference is the declining slope of the calibration pulse which has an exponential shape. The calibration pulse is created by discharging a capacitor which explains the shape of the signal.
- On the Front-End Boards (FEBs), the detector signals from 128 calorimeter channels go through a chain of analog processing (see fig. 4.7). First, the signal is preamplified and split for the main readout and the trigger readout path.

The signal of the main readout path then gets shaped and sampled with the LHC bunch-crossing frequency of 40 MHz (see fig. 4.8). Afterward, the samples are stored in switched-capacitor arrays and, if accepted by the L1 trigger, digitized and sent to the back-end electronics.

On the trigger readout path, the first two stages of analog summing are realized. In the shaper, four signals are summed up. Further summing is done on the layer-sum boards. The summed signal gets processed further on the next board of the front-end electronics.

- On the Tower-Builder Board (TBB), the final stage of the analog summation of trigger signals is executed². Signals from the layer-sum boards are added together for different detector layers forming a so-called trigger tower. Thus, a

²In the FCals and the HECs no further summation is needed. Thus, instead of TBBs Tower-Driver Boards (TDBs) are used.

4. The Liquid-Argon Calorimeter

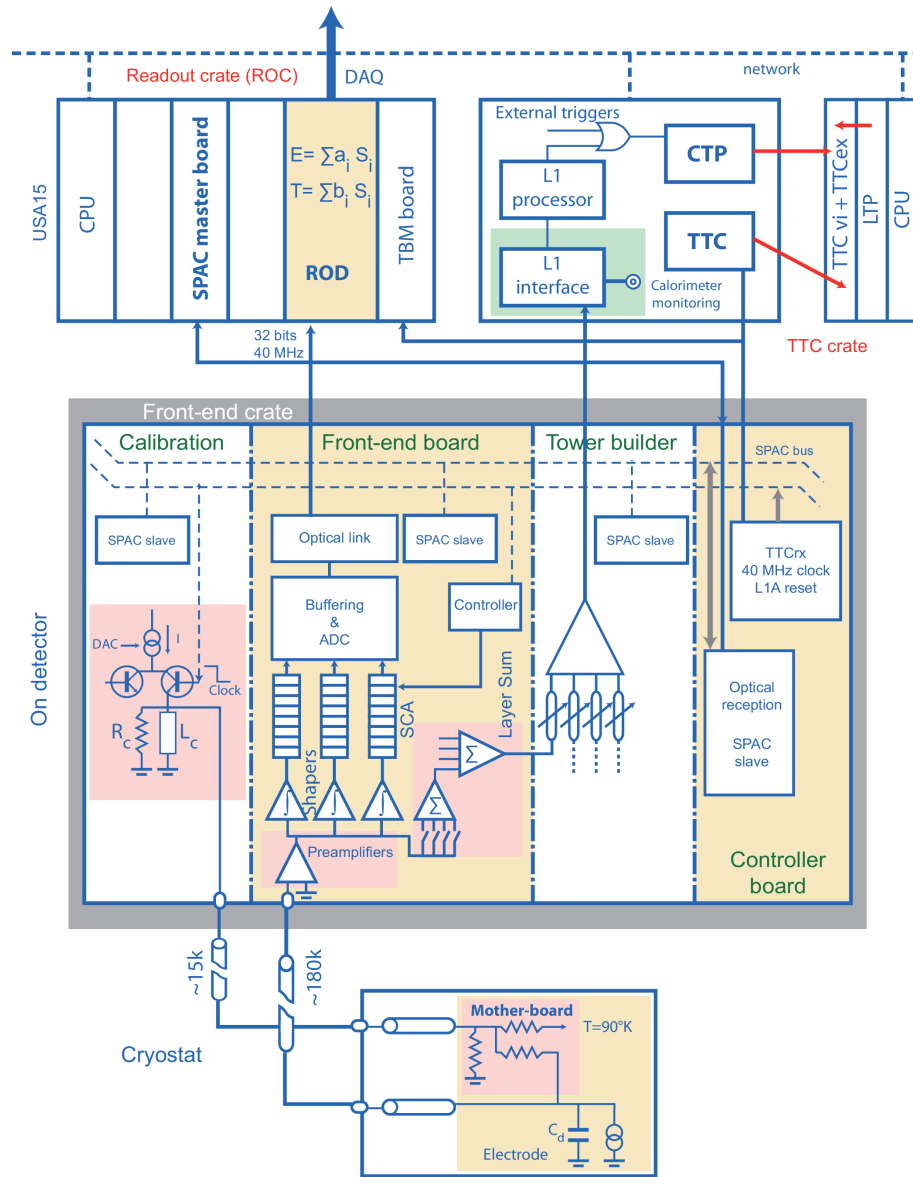


Figure 4.6.: Block diagram of the current LAr calorimeter readout electronics [8]. The lower part is the electronics which are installed in the detector cryostat. In the middle part, the front-end electronics are displayed which are placed on the detector. The back-end electronics in the upper part of the figure are situated off-detector.

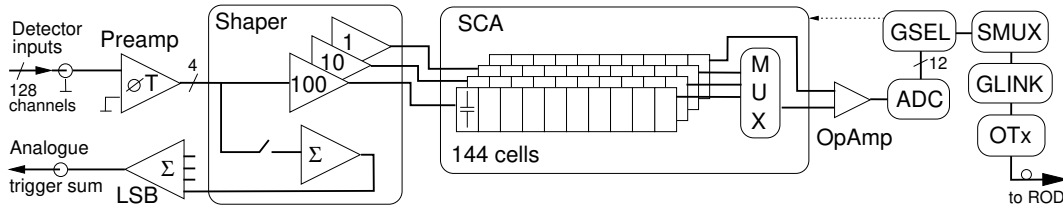


Figure 4.7.: The architecture of the FEB [104]. The dataflow for four readout channels is sketched.

trigger tower is the sum of the signals of an area of $\Delta\eta \times \Delta\phi = 0.1 \times 0.1$ over all detector layers. This trigger-tower signal is then sent to the L1 trigger.

- The controller board receives and distributes the 40 MHz LHC clock, the Level-1 Trigger Accept (L1A) signal, and further calibration and control signals.

4.3.2. Back-End Electronics

The back-end electronics [105] are placed in an off-detector counting room (USA15) 70 m from the ATLAS detector. The boards of the back-end electronics are installed in the readout crates.

- The readout driver performs digital signal processing which is further discussed in chapter 6. After an L1A signal, it receives the signals from eight FEBs being equivalent to 1024 calorimeter channels. The main task is to reconstruct the energy and the time of the hit and to calculate a quality factor for the pulse. This information is then sent to the data acquisition system.
- The trigger, timing, and control system distributes the LHC clock and the L1A signal to the front-end electronics and the readout drivers.
- The L1 trigger receiver interfaces the TBBs to the L1 trigger. As part of the trigger-sum chain, it converts the energy to transverse energy.

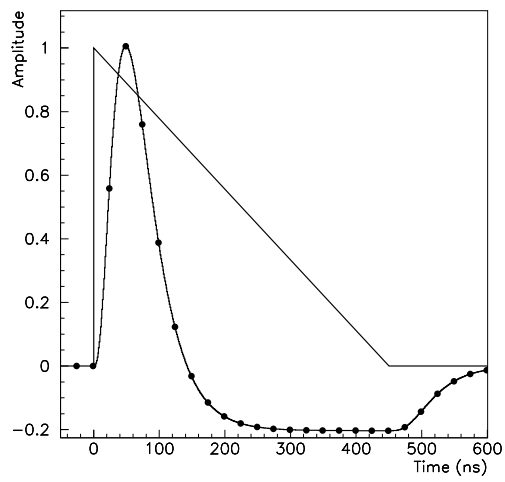


Figure 4.8.: The different stages of the pulse processing [8]. In the analog shaper, the triangular detector pulse shape is changed to a bipolar shape. Afterwards, the pulse shape is sampled with 40 MHz. The samples are indicated with dots on the bipolar pulse shape.

4.4. Level-1 Calorimeter Trigger

The L1Calo trigger [82, 106] gets its input from 7200 analog trigger towers. Different algorithms analyze the signals and send their results to the central trigger processor and to the L1Topo trigger.

During Long Shutdown 1, the L1Calo trigger received a small upgrade. In fig. 4.9, an overview of the structure of the L1Calo trigger during Run 2 is shown.

- During Long Shutdown 1, the pre-processor modules were equipped with new multi-chip modules. The new multi-chip modules digitize the analog trigger tower signals with 80 MHz, use a filter technique to get the bunch-crossing timing and extract the transverse energy. Timing and energy are sent to the next two modules.
- The jet-energy modules identify jets³. For that, they use a sliding window algorithm. Since Run 2, the jet-energy modules do no longer send hit counts of jet objects, but trigger objects. The trigger objects contain location, energy, and type of the identified object.
- The cluster-processor modules work similarly to the jet-energy modules. They identify electrons, photons, and τ leptons above a certain E_T threshold. For this, they use a sliding window algorithm. Like the jet-energy modules, they do no longer send hit counts of e/γ and τ objects, but trigger objects.
- The new common-merger modules take the results from the jet-energy modules and cluster-processor modules and sum them up. The data are then sent to the L1Topo trigger. In addition, the new common-merger modules send hit counts to the central trigger processor.

³In the process of hadronization quarks and gluons from pp collision form cones of mostly hadrons, which are called jets.

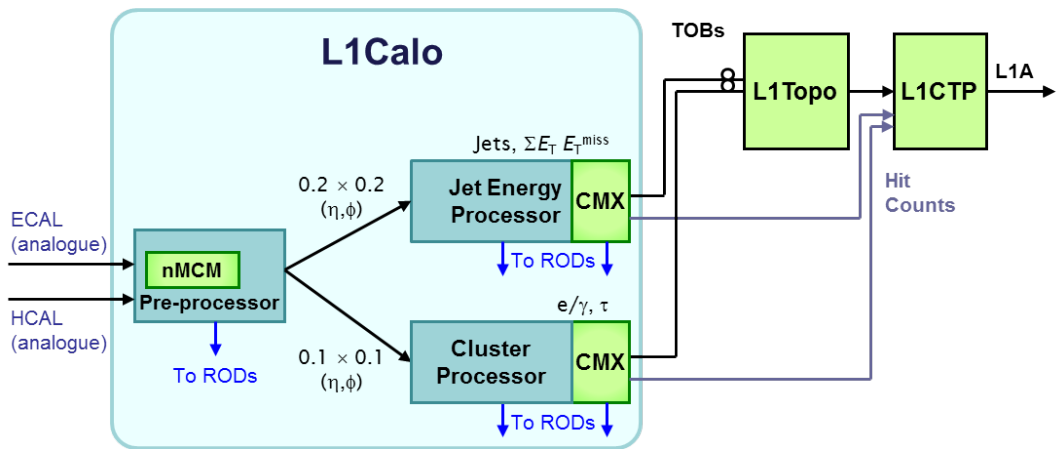


Figure 4.9.: Block diagram of L1Calo trigger [82]. The new components that were introduced before Run 2 are indicated in green.

5. Upgrade Plans

The first runs of the LHC were already very successful. Namely, the observation of the Higgs boson is without dispute the most famous achievement.

Despite this, open questions remain that the Standard Model cannot explain. In order to probe the Standard Model and to identify possible extensions, precision measurements of the Standard Model parameters and processes are performed, as well as searches for new particles and phenomena. To address these goals, a large number of recorded pp collisions is decisive. This will be achieved by an increase of luminosity. To deliver a higher luminosity, an upgrade of the LHC is planned. The key points of this upgrade are outlined in section 5.1.

The upgrade of the LHC brings new challenges for the experiments, as an increase in luminosity leads to an increase of pile-up events. To cope with these challenges, each experiment has its own upgrade agenda. In section 5.2, the different Phase-I upgrades of the ATLAS detector are introduced briefly. A more detailed overview of the Phase-I upgrade of the LAr calorimeter readout electronics is discussed in section 5.3. In section 5.4, an introduction of the demonstrator of the future readout electronics is given.

5.1. Upgrades of the Large Hadron Collider

The LHC was shut down in December 2018. It undergoes several upgrades during the period of the Long Shutdown 2 (2019–2020). The linear accelerator Linac 4 will be integrated into the injector chain and will replace Linac 2. This will lead to a higher injection energy to the Proton Synchrotron Booster. The Proton Synchrotron Booster itself receives an upgrade in the form of a new injection and acceleration system. The last accelerator before the LHC, the Super Proton Synchrotron, gets a new radio-frequency system. Furthermore, a replacement of 20 magnets is planned. In addition, the diodes in the interconnections between the dipole magnets will be consolidated [107].

After the Long Shutdown 2, Run 3 is scheduled for the years 2021–2023. During this period, it is foreseen that the LHC will reach its design center-of-mass energy

5. Upgrade Plans

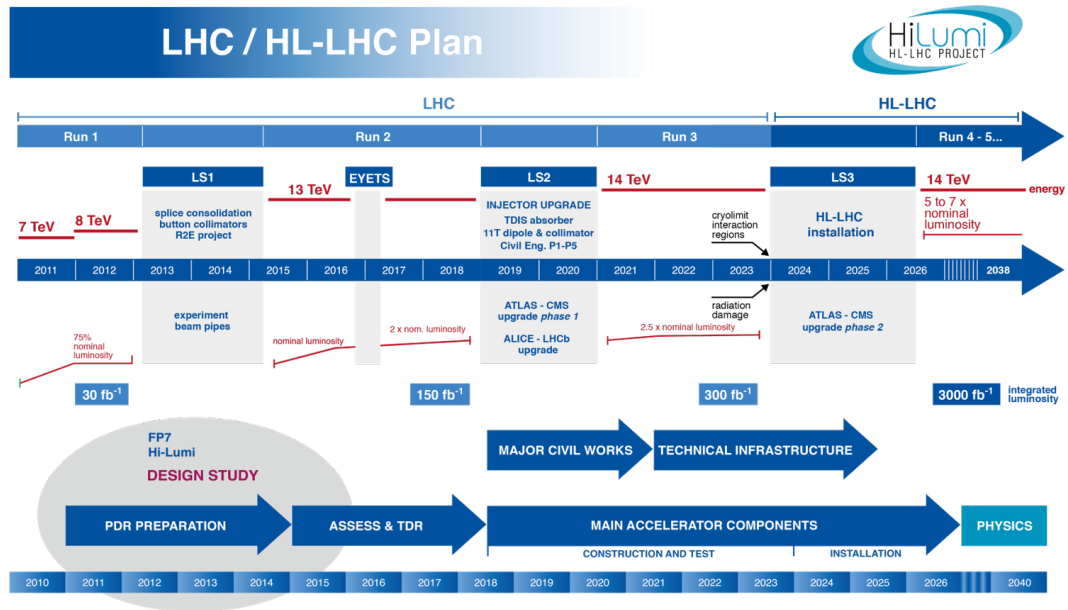


Figure 5.1.: Overview of the LHC operation and upgrade plan [110].

of 14 TeV in pp collisions. The instantaneous luminosity will be about 2.2 times the design luminosity. By the end of Run 3, an integrated luminosity of $L_{\text{int}} = 300 \text{ fb}^{-1}$ is expected [108].

For the years 2024–2026, the Long Shutdown 3 is planned. The LHC will receive a major upgrade, resulting in the era of the High Luminosity LHC (HL-LHC) [109] from 2027–2037. The luminosity will be further increased to 5–7.5 times the design instantaneous luminosity. This will lead to an integrated luminosity of $L_{\text{int}} = 250\text{--}320 \text{ fb}^{-1}$ per year and a total foreseen integrated luminosity of $L_{\text{int}} = 4000 \text{ fb}^{-1}$ for the 12 years of operation of the HL-LHC [108]. In fig. 5.1, an overview of the longterm schedule of the LHC is shown.

5.2. The Phase-I Upgrade of the ATLAS Detector

Though the increase in luminosity provides potential for the physics program, it is also a challenge. An increase in luminosity leads to an increase in the average number of interactions per bunch crossing, $\langle\mu\rangle$, enhancing the effects of pile-up. To cope with that and to maintain trigger thresholds that are close to the ones of the initial runs, an upgrade of the ATLAS detector is inevitable. Therefore, during the Long Shutdown 2, several upgrades focusing on the trigger readout will be installed [11].

- In August 2020, the first of two new small wheels will replace an existing one in the muon spectrometer. During the year-end technical stop of 2021, the second new small wheel will be installed [111]. They will provide the L1Muon trigger with precision tracking to reduce the fake trigger rate [112].
- For the LAr calorimeter, new trigger readout electronics will be installed to provide information to the L1 trigger with finer granularity [113]. In section 5.3, the upgrade of the LAr calorimeter is described in more detail.
- To cope with the above-mentioned upgrades, the TDAQ system itself needs to be upgraded. The L1Muon trigger will get signals from the new small wheels of the muon spectrometer. For the L1Calo trigger, new feature extractors will be installed to cope with the finer granularity from the LAr calorimeter readout [82].

5.3. Upgrade of the Liquid-Argon Calorimeter

The Phase-I upgrade of the LAr calorimeter focuses on the upgrade of the trigger readout electronics. The intention is to provide the L1 trigger with information with a finer granularity compared to the current scheme. In fig. 5.2, an overview of the future readout electronics of the LAr calorimeter is shown. In [113], a detailed description of the upgrade plans can be found.

5.3.1. Supercells

The current trigger readout is based on the approach of trigger towers. This means that the energy in an area of $\Delta\eta \times \Delta\phi = 0.1 \times 0.1$ is summed up across all LAr calorimeter layers. After the Phase-I upgrade, the trigger is provided with data from so-called supercells. The supercells follow a finer segmentation scheme. The

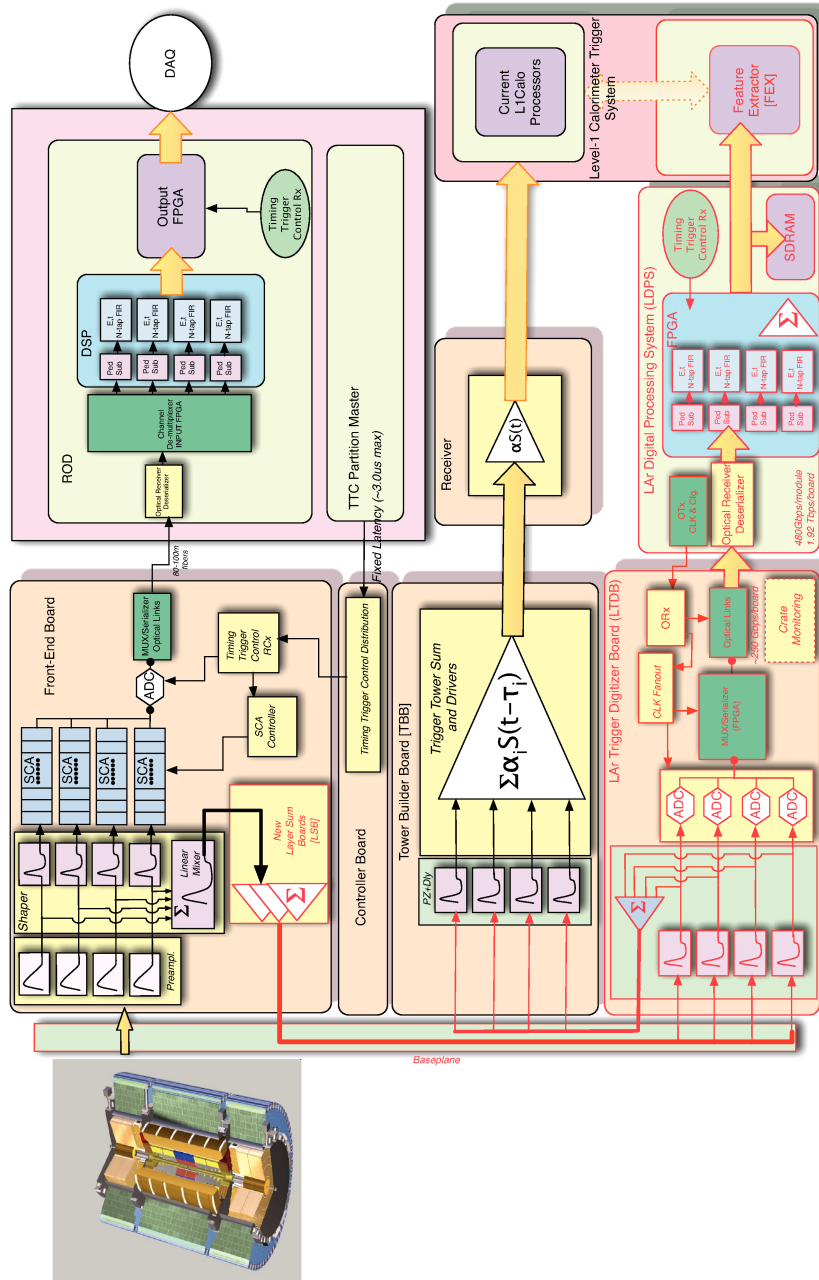


Figure 5.2.: The Phase-I upgrade readout electronics of the LAr calorimeter [113]. The components that will be upgraded or installed are depicted in red. The front-end electronics are on the left side of the block diagram while the back-end electronics are on the right side.

Table 5.1.: Comparison of the current trigger tower granularity and the future supercell granularity in the EMB. The respective sizes are given in $\Delta\eta$ and $\Delta\phi$. In addition, the number of elementary cells, n_η and n_ϕ , that are grouped together to form a trigger tower and a supercell are listed [113].

Layer	EC	TT		SC	
	$\Delta\eta \times \Delta\phi$	$n_\eta \times n_\phi$	$\Delta\eta \times \Delta\phi$	$n_\eta \times n_\phi$	$\Delta\eta \times \Delta\phi$
PS	0.025×0.1	4×1		4×1	0.1×0.1
Front	$0.003\ 125 \times 0.1$	32×1	0.1×0.1	8×1	0.025×0.1
Middle	0.025×0.025	4×4		1×4	0.025×0.1
Back	0.05×0.025	2×4		2×4	0.1×0.1

information will be separately provided for each detector layer. In addition, the front layer and the middle layer will have a higher granularity. This results in a tenfold increase in granularity. In table 5.1, the different sizes of trigger towers and supercells in terms of elementary cells are summarized for the EMB. In fig. 5.3, the modifications between those two concepts are shown.

5.3.2. Upgrade of the Front-End Electronics

In the front-end electronics, in fig. 5.3 the layer-sum boards will be replaced with an upgraded version. The same applies to the base planes. In addition, new LAr Trigger Digitizer Boards (LTDBs) will be installed.

Layer Sum Board

The current layer-sum boards produce $\Delta\eta \times \Delta\phi = 0.1 \times 0.1$ sums per detector layer for the trigger towers. As for the supercells, a finer granularity in the front layers and the middle layers is needed, they will be replaced with new layer-sum boards.

Base Plane

The new base planes have to keep the FEB slots intact while providing slots for the LTDB. In addition, they have to cope with the transmission of an increased number of signals from FEB to LTDB compared to the current trigger readout system.

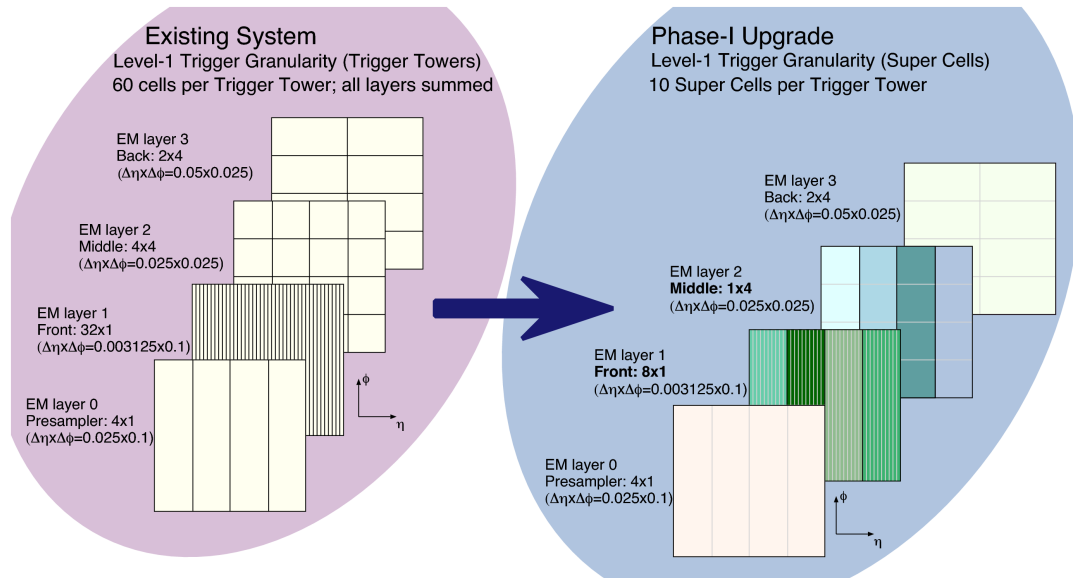


Figure 5.3.: Comparison of the granularity of the trigger tower and the supercell concept. For the trigger tower on the left, the energies are summed up across all four layers. The new supercells will be separately read out per detector layer and the segmentation in the front layer and the middle layer will be finer [113].

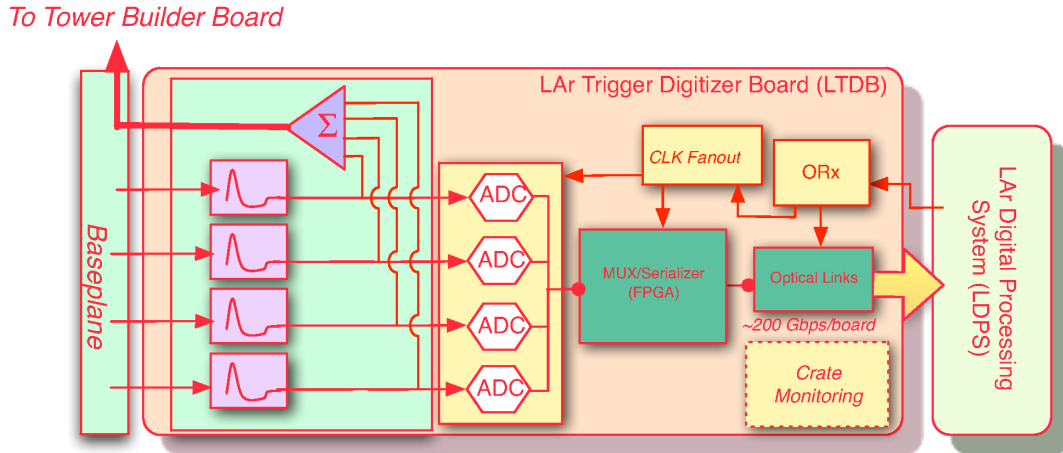


Figure 5.4.: Block diagram of the new LTDB [113]. The signals transmitted by the base plane enter on the left. The analog part is marked in light green. Everything right of the Analog-to-Digital Converters (ADCs) accounts for the digital part of the LTDB.

LAr Trigger Digitizer Board

The new LTDB receives the signals of up to 320 supercells. It has to fulfill two tasks, building analog sums for the TBBs, and digitizing the supercell signals. Hence, the LTDB has an analog and a digital part. In fig. 5.4, an overview of the LTDB is shown.

The electronics of the analog part have to provide signals that use the full range of the 12 bit ADC, while at the same time keeping the signal-to-noise ratio at a reasonable level. Therefore, a suitable gain, shaping, and offset needs to be chosen. In addition, the functionality of the legacy trigger chain must be maintained. In the case, that the supercell has the same size as the trigger tower the signals are sent to the LTDB and to the TBB/TDB. If the signals have a finer granularity than the trigger tower, they are summed in groups of four according to the corresponding trigger tower.

In the digital part, the signals will be digitized with a sampling rate of 40 MHz. To maintain the signal-to-noise ratio the quantization error should not exceed the intrinsic electronics noise of the preamplifiers, linear mixers, and summing amplifiers. The digitized signals will then be transmitted via optical fibers to the back-end electronics.

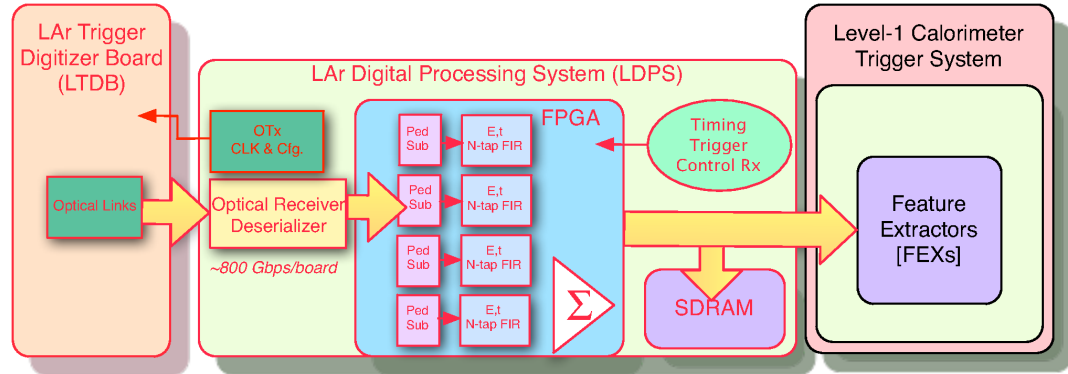


Figure 5.5.: Block diagram of the new LDPS [113]. The signals are received from the LTDBs from the left. At the core of the LDPS is the FPGA which reconstructs the energy for each bunch crossing. The reconstructed energy is then sent to the L1Calo trigger.

5.3.3. Upgrade of the Back-End Electronics

The new LAr Digital Processing System (LDPS) marks the upgrade of the back-end electronics. In fig. 5.5, a block diagram of the architecture is shown. The LDPS receives signals from 124 LTDBs. At the core of the new system, powerful Field Programmable Gate Arrays (FPGAs)¹ extract the transverse energy of each supercell. One FPGA will process the data of up to 320 supercells. For each bunch crossing, the LDPS sends the reconstructed energy to the L1Calo trigger. Hence, it is crucial that the LDPS can efficiently receive and transmit large data streams. In addition, the LDPS buffers the data for potential usage by the high-level trigger and the data acquisition system. Special, so-called FELIX cards distribute the trigger, timing, and control signals to the LTDBs and the LAr Digital Processing Blades (LDPBs). Furthermore, the LDPS has to be integrated into the data acquisition system.

The LDPS consists of 31 LDPBs. Each of those is composed of four advanced-mezzanine cards. Every advanced-mezzanine card is equipped with one FPGA. The whole system is installed next to the legacy trigger electronics in the USA15 counting room.

¹An FPGA can be understood as a set of logical blocks (like memory, look-up tables, and digital signal processors) with reprogrammable interconnections.

5.3.4. Upgrade of the Level-1 Calorimeter Trigger

The upgrade of the L1Calo trigger focuses on utilizing the finer granularity which is provided by the supercell readout scheme. To process the supercell data two new subsystems, the electromagnetic feature extractor and the jet feature extractor, will be installed. In addition to the finer granularity, the feature extractors will be able to handle the already digitized signal.

The upgraded system will operate similar to the legacy system of the L1Calo trigger. The electromagnetic feature extractor will identify e/γ and τ candidates, while the jet feature extractor will identify energetic jet candidates and calculate E_T^{sum} and E_T^{miss} .

For the time after Long Shutdown 2, it is planned to run the feature extractors in parallel to the current system. To keep the cluster processors and the jet/energy-sum processors working, they will still receive their data from the TBBs. For further explanations of the legacy system refer to section 4.4.

In fig. 5.6, the architecture of the upgraded system is shown. In [82], a detailed description of the upgrade can be found.

5.3.5. Shower Shape Variables

Due to the finer granularity, the feature extractors will be able to use more sophisticated algorithms to identify a signal event and distinguish it from a background event. For the identification of electrons², three variables have been investigated in [113]. These variables are used similarly in the offline identification of electrons. The studies are made with the ATLAS detector simulation [114]. Electrons from $Z \rightarrow e^+e^-$ decays were taken as signal events. Hadronic jets serve as background. To get Run 3 conditions ($\langle\mu\rangle = 80$), the signal was overlaid by minimum-bias events generated with PYTHIA [115]. The interaction of the particles with the detector is simulated with GEANT4 [116].

In the following, the three shower-shape variables are introduced together with the results of the studies in [113].

The first shower-shape variable is the energy ratio, R_η . To calculate it, the starting point is the supercell with the highest transverse energy deposition in the middle layer. In the next step, the transverse energies are summed up in clusters around that very same supercell. R_η is defined as the ratio between the transverse energies

²The same holds for photons though they wont be mentioned in the following.

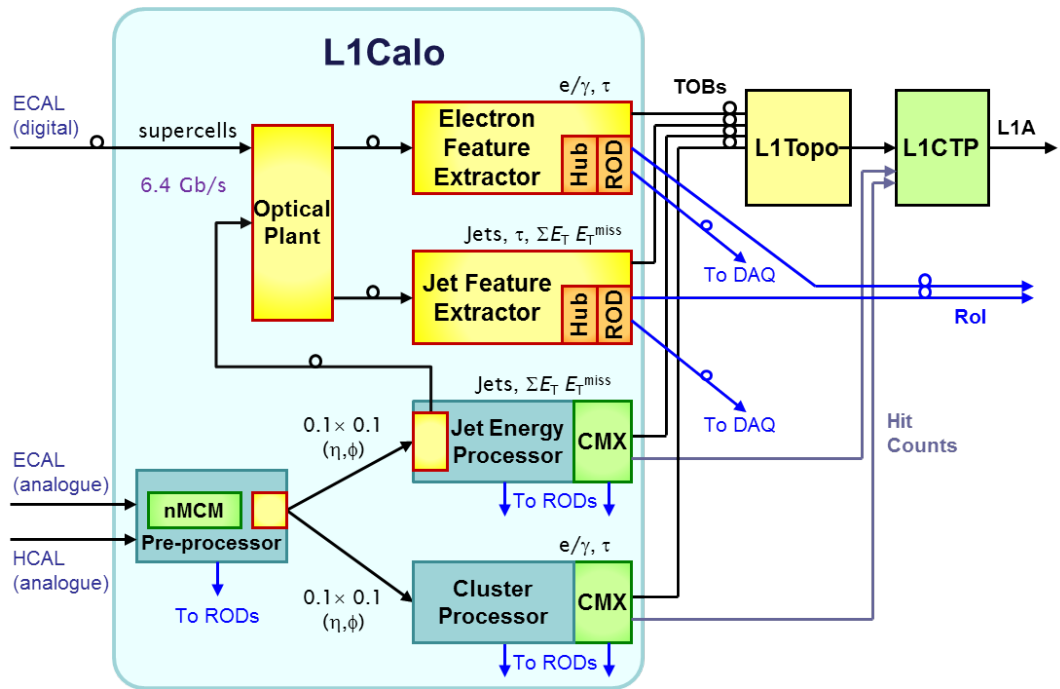


Figure 5.6.: Block diagram of the L1Calo trigger Phase-I upgrade [82]. The new parts are marked in yellow and orange.

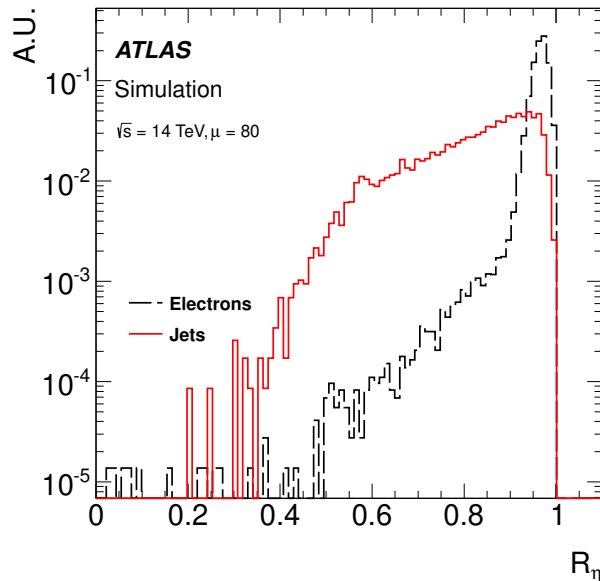


Figure 5.7.: R_η distributions for electrons and background jets with $p_T > 20$ GeV [113]. Since electrons produce a narrow shower in the ATLAS detector, the distribution is close to unity. As expected, the distribution of background jets is broader.

in a 3×2 cluster of supercells and a 7×2 cluster:

$$R_\eta = \frac{E_{T, \Delta\eta \times \Delta\phi = 0.075 \times 0.2}^{(2)}}{E_{T, \Delta\eta \times \Delta\phi = 0.175 \times 0.2}^{(2)}}. \quad (5.1)$$

In fig. 5.7, the distribution for electrons and background jets are compared. The different shower widths of the two processes help to distinguish them. Electrons produce a narrower shower depositing most of their energy in the 3×2 cluster of supercells. That results in a R_η distribution close to unity. The background jets, on the other hand, produce a much broader shower with more energy deposited in the supercells around the 3×2 cluster.

The second shower-shape variable investigated is the energy fraction in the back layer, f_3 . It is the ratio between the transverse energy deposited in the back layer in an area of $\Delta\eta \times \Delta\phi = 0.2 \times 0.2$ and the energy in an electromagnetic cluster in the

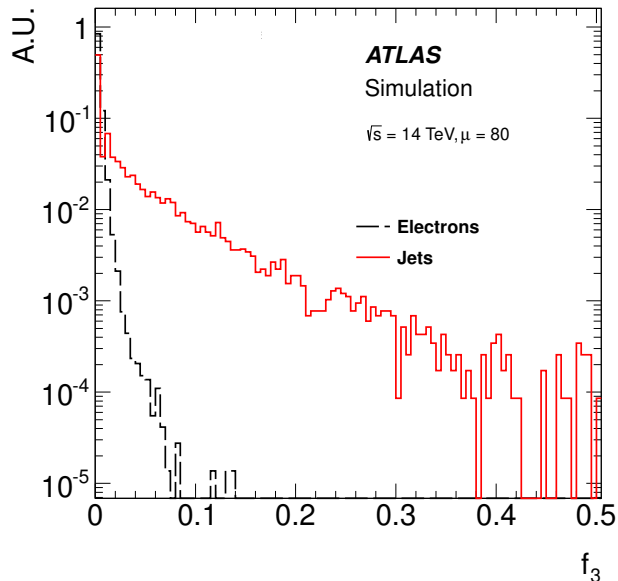


Figure 5.8.: f_3 distributions for electrons and background jets with $p_T > 20 \text{ GeV}$ [113]. Since electrons deposit their energy mainly in the front layer and the middle layer only a small fraction is measured in the back layer. Hadronic jets on the other hand are expected to extend to the Tile calorimeter depositing a bigger fraction of their energy in the back layer.

front layer, the middle layer, and the back layer. For the front layer and the middle layer, the clusters have a size of $\Delta\eta \times \Delta\phi = 0.075 \times 0.2$. f_3 is defined as:

$$f_3 = \frac{E_{T, \Delta\eta \times \Delta\phi=0.2 \times 0.2}^{(3)}}{E_{T, \Delta\eta \times \Delta\phi=0.075 \times 0.2}^{(1)} + E_{T, \Delta\eta \times \Delta\phi=0.075 \times 0.2}^{(2)} + E_{T, \Delta\eta \times \Delta\phi=0.2 \times 0.2}^{(3)}}. \quad (5.2)$$

In fig. 5.8, the distribution for electrons and background jets are compared. The longitudinal development of electromagnetic and hadronic showers is different as the hadronic showers of the background jets develop into the Tile calorimeter. That results in the deposition of more energy in the back layer. Electrons, on the other hand, will deposit the main fraction of their energy in the front layer and the middle layer.

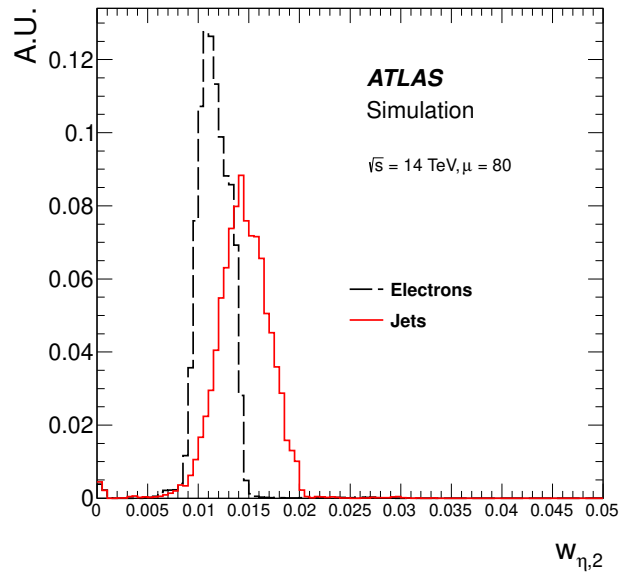


Figure 5.9.: $w_{\eta,2}$ distributions for electrons and background jets with $p_T > 20$ GeV [113]. The smaller lateral development of electromagnetic showers compared to hadronic showers is visible.

The last investigated shower-shape variable is the shower width, $w_{\eta,2}$. It measures the width of the energy distribution in the middle layer in a 3×2 cluster of supercells. It is defined as:

$$w_{\eta,2} = \sqrt{\frac{\sum (E_T^{(2)} \times \eta^2)_{\Delta\eta \times \Delta\phi = 0.075 \times 0.2}}{E_{T,\Delta\eta \times \Delta\phi = 0.075 \times 0.2}^{(2)}} - \left(\frac{\sum (E_T^{(2)} \times \eta)_{\Delta\eta \times \Delta\phi = 0.075 \times 0.2}}{E_{T,\Delta\eta \times \Delta\phi = 0.075 \times 0.2}^{(2)}} \right)^2}. \quad (5.3)$$

In fig. 5.9, the distribution for electrons and background jets are compared. The spread of the transverse energy from an electron shower is small compared to the spread of a jet. The explanation is caused by the smaller lateral development of electromagnetic showers, similarly to R_η .

In fig. 5.10, the effect on the trigger rates of successively applying these variables is shown. The objective is to keep a high signal detection efficiency while getting

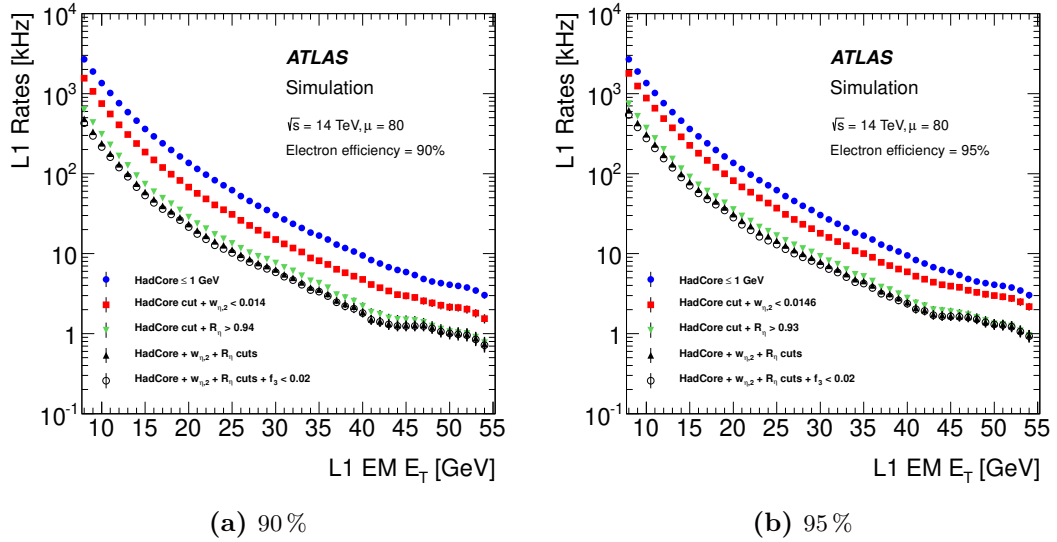


Figure 5.10.: Trigger rates for $\langle\mu\rangle = 80$ as a function of E_T with (a) 90 % and (b) 95 % trigger efficiency [113]. The signal events are electrons with $p_T > 20$ GeV from simulated $Z \rightarrow e^+e^-$ decays.

the E_T threshold as low as possible for a given trigger rate of about 20 kHz. The optimized cut parameters on the shower-shape variable are $R_\eta \geq 0.93$ (0.94), $w_{\eta,2} < 0.0146$ (0.014), and $f_3 \leq 0.02$ (0.02). Additionally, a 1 GeV cut on the HadCore variable was applied. The name HadCore refers to a cluster of 2×2 trigger towers in the Tile calorimeter right behind the electromagnetic shower. For a desired trigger efficiency of 95 % (90 %) at a trigger rate of 20 kHz that leads to an E_T threshold of 21.5 GeV (20 GeV).

5.4. Demonstrator System of the Phase-I Upgrade of the Trigger Readout Electronics

To assess technical issues and evaluate the performance, a demonstrator system of the Phase-I trigger readout electronics has been built. The focus was on studying whether the electronics disturb the current readout system and if they add extra noise, and on gaining experience about the supercell pulse shapes and timing [117].

The LAr demonstrator system consists of two pre-prototype LTDBs which are named after the institutes that built the boards. They are made of non-radiation hard

5.4. Demonstrator System of the Phase-I Upgrade of the Trigger Readout Electronics

commercial components. The BNL³ board is based on a digital motherboard and an analog mezzanine, while the LAL/Saclay⁴ board is based on an analog motherboard and a digital mezzanine. Each LTDB demonstrator board digitizes up to 320 supercell signals. They have been extensively tested at the electronic-maintenance facility at CERN before installation during the Long Shutdown 1 in 2014. The coverage of the two boards is $0 < \eta < 1.4$, and $\frac{9}{16} \cdot \pi < \phi < \frac{11}{16} \cdot \pi$ [117].

Two ATCA Test Boards for Baseline Acquisition (ABBAs) [118] serve as LDPBs. Both ABBAs are equipped with two FPGAs. Each FPGA receives its data from the supercells in one specific ϕ -slice, i_ϕ , in the EMB⁵. The corresponding ϕ -slices are $i_\phi = 18, 19, 20$ and 21 .

During Run 2 calibration pulses and noise measurements were performed. The results of these measurements are in accordance with the expected outcomes (see figs. 5.11 and 5.12).

During the year-end technical stop of 2017/2018, the two pre-prototype LTDBs and the two ABBAs were decommissioned. As a replacement, two pre-production LTDBs [119] were installed at the beginning of 2018. To replace the ABBAs, a Liquid-Argon Carrier (LArC) board and two LAr Trigger prOcessing MEzzanines (LATOMEs) were installed in mid-2018.

³Brookhaven National Laboratory

⁴Laboratoire de l'Accelérateur Lineaire and Saclay

⁵The EMB is separated in 64 ϕ -slices. Each cover a range of $\frac{\pi}{32}$ in ϕ .

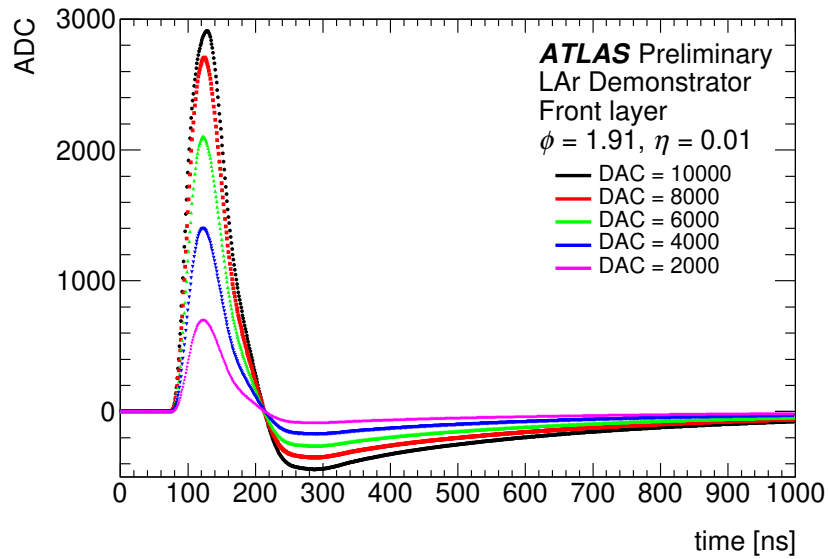


Figure 5.11.: Measured pulse shapes of a front layer supercell of the LAr demonstrator system [117]. As signals, calibration pulses were injected with different amplitudes/DAC values. The pulse shapes meet the expectations. The amplitude of the pulse shapes behave linearly up to DAC values of 8000. For higher DAC values, the analog part of the LAr demonstrator system saturates.

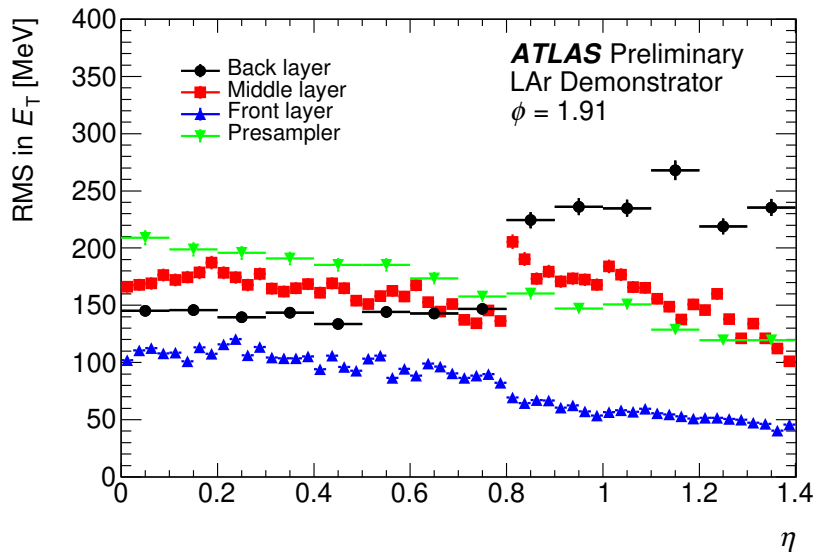


Figure 5.12.: Measured noise level in transverse energy as a function of η of the LAr demonstrator system supercells [117]. The noise level per supercell is between 100–250 MeV. This is in accordance with the expected values which are the quadratic mean of the noise of the corresponding elementary cells. The offset at $\eta = 0.8$ is due to the change of the absorber thickness, electrodes, and calibration resistors.

6. Digital Processing of Liquid-Argon Calorimeter Signals

The Phase-I upgrade of the LAr calorimeter foresees the installation of new trigger readout electronics. The new electronics allow the trigger to use more sophisticated algorithms to distinguish between signal and background. These algorithms need to have precise information about the energy deposition in the supercells. To obtain this information, digital filter algorithms are used.

In section 6.1, the LAr calorimeter pulse shapes are presented. The different sources of noise that lead to a distortion of the detector signals are discussed in section 6.2. This is followed by a few general remarks about digital filter algorithms in section 6.3. Afterward, two different filter algorithms are introduced. Section 6.4 explains the computation of the Optimal Filter coefficients. Section 6.5 does the same for the Wiener filter coefficients. An extension to the Wiener filter, the forward correction, is presented in section 6.6.

6.1. Pulse Shapes of the Liquid-Argon Calorimeter

When particles ionize the liquid argon, they produce a triangular current pulse as described in section 4.1. The transformation of this detector pulse to the digital samples that are used for energy reconstruction consists of multiple steps: preamplification, analog shaping, and digitization. The process is shown in fig. 6.1 as an example.

The triangular detector pulse shape has a very short rise time of a few nanoseconds, followed by a linear decay over about 450 ns. First, this signal gets amplified in the preamplifier. Next is the $CR-(RC)^2$ shaper which acts as a bandpass and transforms the unipolar triangular detector pulse shape into a bipolar pulse shape. The peak of the bipolar pulse shape is slightly shifted with respect to the triangular pulse shape. The bipolar pulse shape has a short positive lobe which continues in the negative range with a long undershoot. The undershoot has a depth of about 20% of the peak amplitude. Peak and undershoot of the bipolar pulse shape integrate to zero.

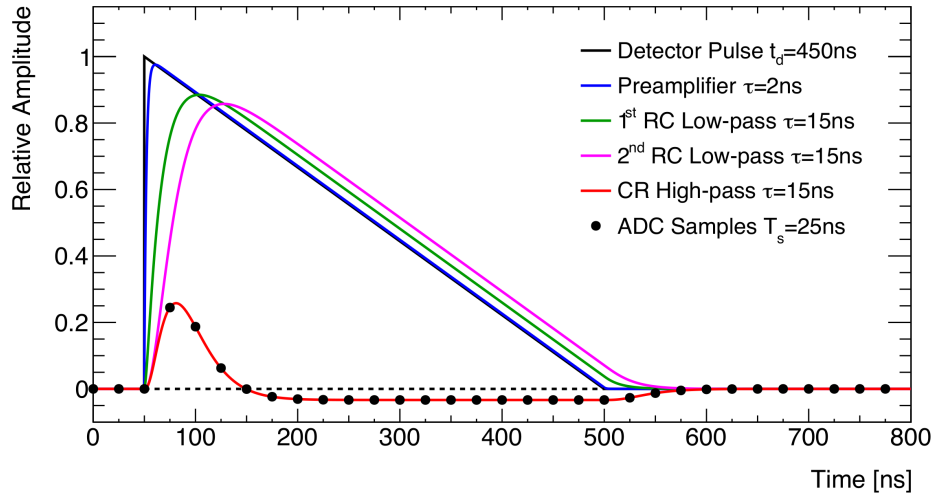


Figure 6.1.: The shaping of the detector pulse of the LAr calorimeter. First, the triangular pulse shape (black) gets preamplified (blue). Then, it is shaped through two RC circuits (green and magenta) and a CR circuit (red). The digitized samples are indicated with black dots.

The pulse is then digitized by the ADC at a sampling rate of 40 MHz before being sent to the digital signal processing. Both the detector pulse and the bipolar pulse have a length of about 500 ns, which is much greater than the bunch crossing time of 25 ns.

The actual pulse shape differs between the four detector layers of the LAr calorimeter. In fig. 6.2, examples of measured pulse shapes are shown. The signals are produced with cosmic muons and are in good agreement with the simulated pulse shapes.

6.1. Pulse Shapes of the Liquid-Argon Calorimeter

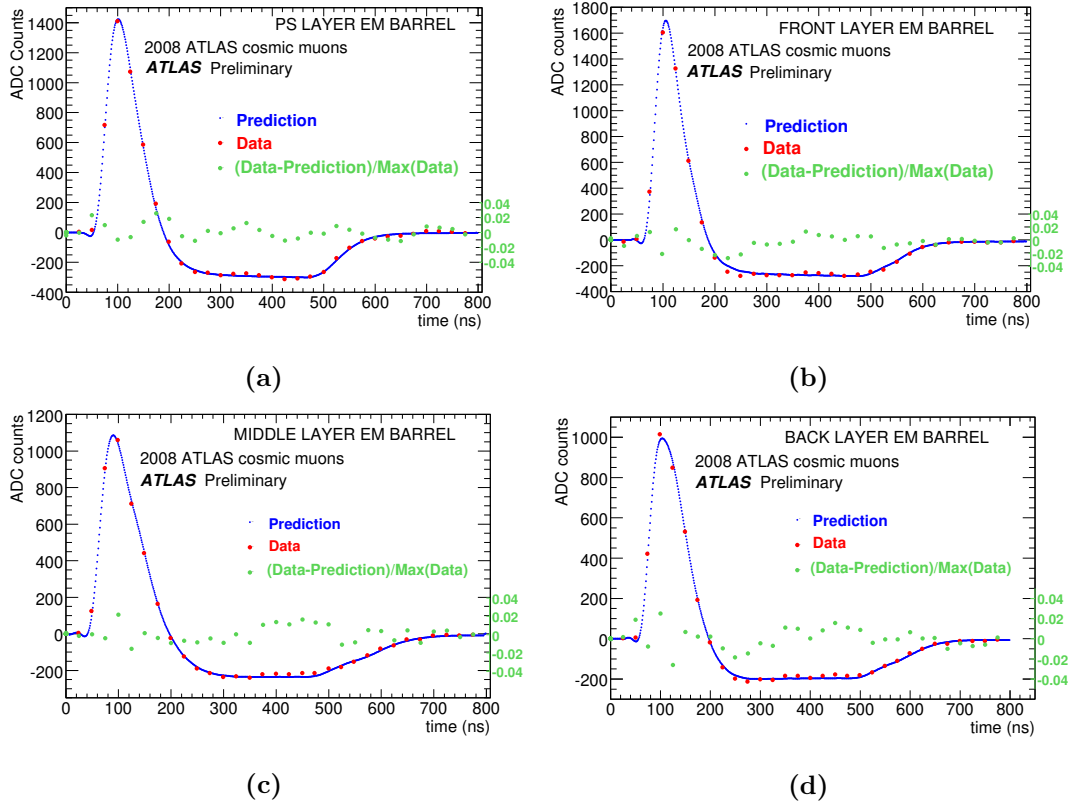


Figure 6.2.: Comparison of measured (red) and simulated (blue) pulse shapes of the EMB [120]. The difference is indicated in green.

6.2. Sources of Noise

The two sources for signal distortion are electronics and pile-up noise.

Electronics noise itself has two sources. The thermal motion of electrons in electrical conductors leads to thermal noise before and in the preamplifier. The second source is the quantization noise of the ADC. In the ADC, the input signal is first sampled, turning the continuous-time signal in a discrete-time signal. Then, the discrete-time signal is quantized, which means that the input value is rounded to the nearest quantization level¹, leading to an irrevocable error [121].

As discussed in section 3.3, besides the interaction of interest, multiple additional pp collisions may occur during a bunch crossing. These additional interactions are called pile-up interactions. With an increase in the luminosity, the average number of pp collisions, μ , increases. Hence, this leads to an increase in pile-up effects. There are two types of pile-up, in-time pile-up and out-of-time pile-up.

In-time pile-up is the effect of multiple interactions during one bunch crossing. If particles from different interactions deposit their energy in the same cell, the energy depositions overlap. This looks like an energy deposition from a single event since it is not possible to distinguish between the various depositions.

Out-of-time pile-up, on the other hand, comes from additional interactions in bunch crossings before and after the interaction of interest. As discussed in section 6.1, the pulse shapes are spread over several bunch crossings due to their length. Therefore, it is possible, that the signals of interactions from consecutive bunch crossings overlap.

Due to the structure of the bunch train² (see section 3.1), pile-up leads to a shift in the baseline of the ADC. At the beginning of a bunch train, the positive contributions of the bipolar pulse shape raise the baseline, resulting in a positive baseline shift. After a few bunch crossings, the negative contributions of the undershoot compensate for the positive contributions and the baseline returns to its pedestal value. After the end of the bunch train, the negative contributions of the undershoot lower the baseline, resulting in a negative baseline shift. If the time between two bunch trains is shorter than the length of the undershoot, this affects the following bunch train. In fig. 6.3, an example of this baseline shift is depicted schematically.

¹An n bit ADC has 2^n quantization levels.

²A continuous sequence of filled bunches is called *bunch train*.

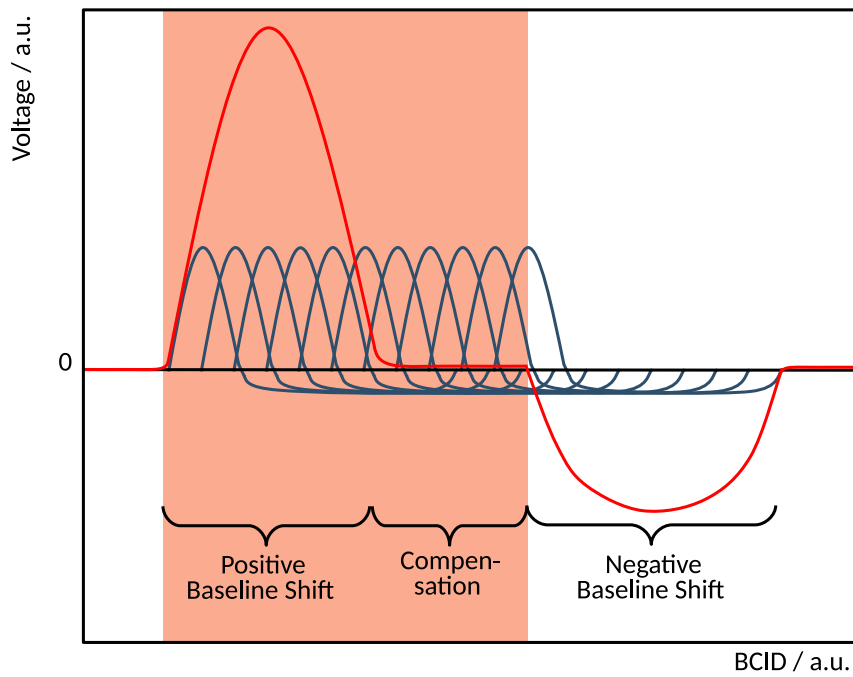


Figure 6.3.: Schematic depiction of the baseline shift (red) due to pile-up. The bunch train is highlighted in orange. The contributions of the pile-up are drawn in blue. Modified version taken from [122].

6.3. Digital Filter Algorithms

In signal processing, the term filtering refers to an operation that modifies an input signal. It aims to remove unwanted signal components, e.g. to reduce the noise [123].

Filter algorithms are characterized by their impulse response. It is the output of the filter to a unit sample excitation described by the Kronecker δ -function:

$$\delta(n) = \begin{cases} 0, & \text{if } n \neq 0, \\ 1, & \text{if } n = 0. \end{cases} \quad (6.1)$$

6.3.1. Finite Impulse Response Filter

The Finite Impulse Response (FIR) filter is characterized by an impulse response of finite duration. From a mathematical point of view, the FIR filter is a linear combination of the M last samples $x(n)$ of the input signal:

$$y(n) = \sum_{k=0}^{M-1} b_k x(n-k), \quad (6.2)$$

where $y(n)$ is the output signal of the filter, b_k is the k -th value of the impulse response, also called filter coefficient, and M is the length or order of the filter. When excited by a δ -function, the response of the FIR filter is identical to the filter coefficients b_k . Because of this finite response, FIR filters are intrinsically stable [123].

6.3.2. Infinite Impulse Response Filter

The Infinite Impulse Response (IIR) filter has an impulse response of infinite duration. Similar to the FIR filter, the output is a linear combination of M input samples. But in addition, N output samples are fed back into the calculation:

$$y(n) = \frac{1}{a_0} \left(\sum_{k=0}^M b_k x(n-k) - \sum_{k=1}^N a_k y(n-k) \right) \quad (6.3)$$

where M is the feed-forward filter order, b_k are the feed-forward filter coefficients, N is the feed-back filter order, and a_k are the feed-back filter coefficients. When excited by a δ -function, the response of the IIR filter does not return to zero [123].

6.4. Optimal Filter

The Optimal Filter is a FIR filter [124]. It is currently used to obtain information about the amplitude and the timing of the LAr calorimeter pulses. The design of the Optimal Filter was described by Cleland and Stern in 1993. The filter coefficients of the Optimal Filter are determined in such a way that the signal-to-noise ratio is maximized. To determine the filter coefficients, knowledge about the pulse shape of the detector signal and the autocorrelation matrix of the total noise is required.

Starting from a signal with known pulse shape, g , but unknown amplitude, A , and unknown time deviation, τ , (in relation to the bunch-crossing time), the measured samples of the signal are:

$$S_i = Ag(t_i - \tau). \quad (6.4)$$

Applying a Taylor expansion to linearize the dependence on τ leads to:

$$S_i = Ag_i - A\tau g'_i + n_i, \quad (6.5)$$

with the noise contribution, n_i . The notational convention $g(t_i) = g_i$ was used. To determine the amplitude and the time deviation from the samples, S_i , two FIR filters with coefficients, a_i and b_i , are used:

$$u = \sum_i a_i S_i, \quad (6.6)$$

$$v = \sum_i b_i S_i. \quad (6.7)$$

To determine a_i and b_i , the expectation value of u is required to be A and the expectation value of v to be $A\tau$:

$$A = \langle u \rangle = \sum_i (Aa_i g_i - A\tau a_i g'_i + \langle n_i \rangle), \quad (6.8)$$

$$A\tau = \langle v \rangle = \sum_i (Ab_i g_i - A\tau b_i g'_i + \langle n_i \rangle). \quad (6.9)$$

Assuming unbiased noise ($\langle n_i \rangle = 0$), leads to the following constraints on the coefficients:

$$\sum_i a_i g_i = 1, \quad \sum_i a_i g'_i = 0, \quad (6.10)$$

$$\sum_i b_i g_i = 0, \quad \sum_i b_i g'_i = -1. \quad (6.11)$$

The variances of u and v are given by:

$$\begin{aligned}\text{Var}(u) &= \sum_{ij} a_i a_j \langle n_i n_j \rangle \\ &= \sum_{ij} a_i a_j R_{ij},\end{aligned}\tag{6.12}$$

and

$$\begin{aligned}\text{Var}(v) &= \sum_{ij} b_i b_j \langle n_i n_j \rangle \\ &= \sum_{ij} b_i b_j R_{ij},\end{aligned}\tag{6.13}$$

with the expectation value $\langle n_i n_j \rangle = R_{ij}$, the autocorrelation function of the noise evaluated at time $t_i - t_j$. The autocorrelation matrix \mathbf{R} of the total noise is composed of the autocorrelation of the electronics noise \mathbf{R}_t and the autocorrelation of the pile-up noise \mathbf{R}_p . The summation of their components gives:

$$\langle n_i n_j \rangle = R(t_i - t_j) = R_t(t_i - t_j) + R_p(t_i - t_j) = R_{ij}.\tag{6.14}$$

The variances of u and v are minimized, while satisfying the constraints of eqs. (6.10) and (6.11). Introducing the Lagrange multipliers λ , κ , μ , and ρ leads to two functions:

$$I_u = \sum_{ij} a_i a_j R_{ij} - \lambda \left(\sum_i a_i g_i - 1 \right) - \kappa \sum_i a_i g'_i,\tag{6.15}$$

$$I_v = \sum_{ij} b_i b_j R_{ij} - \mu \sum_i b_i g_i - \rho \left(\sum_i b_i g'_i + 1 \right).\tag{6.16}$$

Setting the partial derivatives with respect to a_i and b_i to zero:

$$\frac{\partial I_u}{\partial a_i} = \sum_j a_j R_{ij} - \lambda g_i - \kappa g'_i = 0,\tag{6.17}$$

$$\frac{\partial I_v}{\partial b_i} = \sum_j b_j R_{ij} - \mu g_i - \rho g'_i = 0.\tag{6.18}$$

This leads to a set of linear equations, which can be expressed in matrix form using $\mathbf{a} \equiv (a_0, \dots, a_{N-1})^T$ and $\mathbf{b} \equiv (b_0, \dots, b_{N-1})^T$ with the expected pulse shape

$\mathbf{g} = (g_0, \dots, g_{N-1})^T$ and its derivatives \mathbf{g}' and the inverse of the autocorrelation function $\mathbf{V} = \mathbf{R}^{-1}$:

$$\mathbf{a} = \lambda \mathbf{V} \mathbf{g} + \kappa \mathbf{V} \mathbf{g}', \quad (6.19)$$

$$\mathbf{b} = \mu \mathbf{V} \mathbf{g} + \rho \mathbf{V} \mathbf{g}'. \quad (6.20)$$

Using the constraints of eqs. (6.10) and (6.11), one can determine the Lagrange multipliers:

$$\mathbf{g} \mathbf{a} = \lambda \mathbf{g}^T \mathbf{V} \mathbf{g} + \kappa \mathbf{g}^T \mathbf{V} \mathbf{g}' = \lambda Q_1 + \kappa Q_3 = 1, \quad (6.21)$$

$$\mathbf{g}' \mathbf{a} = \lambda \mathbf{g}'^T \mathbf{V} \mathbf{g} + \kappa \mathbf{g}'^T \mathbf{V} \mathbf{g}' = \lambda Q_3 + \kappa Q_2 = 0, \quad (6.22)$$

$$\mathbf{g} \mathbf{b} = \mu \mathbf{g}^T \mathbf{V} \mathbf{g} + \rho \mathbf{g}^T \mathbf{V} \mathbf{g}' = \mu Q_1 + \rho Q_3 = 0, \quad (6.23)$$

$$\mathbf{g}' \mathbf{b} = \mu \mathbf{g}'^T \mathbf{V} \mathbf{g} + \rho \mathbf{g}'^T \mathbf{V} \mathbf{g}' = \mu Q_3 + \rho Q_2 = -1, \quad (6.24)$$

where the following abbreviations are used:

$$Q_1 = \mathbf{g}^T \mathbf{V} \mathbf{g}, \quad (6.25)$$

$$Q_2 = \mathbf{g}'^T \mathbf{V} \mathbf{g}', \quad (6.26)$$

$$Q_3 = \mathbf{g}^T \mathbf{V} \mathbf{g}' = \mathbf{g}'^T \mathbf{V} \mathbf{g}. \quad (6.27)$$

The solutions of the Lagrange multipliers are:

$$\lambda = \frac{Q_2}{\Delta}, \quad \kappa = -\frac{Q_3}{\Delta}, \quad (6.28)$$

$$\mu = \frac{Q_3}{\Delta}, \quad \rho = -\frac{Q_1}{\Delta}, \quad (6.29)$$

where $\Delta = Q_1 Q_2 - Q_3^2$.

Using the Lagrange multipliers together with the known pulse shape, \mathbf{g} , and the measured autocorrelation matrix, \mathbf{R} , the eqs. (6.19) and (6.20) are fully determined and the coefficients, a_i and b_i , of the Optimal Filter can be calculated. Hence, the amplitude, A , and the time deviation, τ , can be computed from the signal samples, S_i :

$$\hat{A}(n) = \sum_{i=0}^{M-1} a_i \cdot S(n+i-M), \quad (6.30)$$

$$\hat{\tau}(n) = \frac{1}{A(n)} \sum_{i=0}^{M-1} b_i \cdot S(n+i-M). \quad (6.31)$$

6.5. Wiener Filter

The Wiener filter is a least square error filter [121, 123]. The filter coefficients are chosen to minimize the error between an input signal, S , and a desired output signal, A . In the following, the calculation of the filter coefficients is described for an FIR filter. A Wiener filter, however, can also be realized as IIR filter.

The relation between an input signal, S , and the output signal, \hat{A} , of a Wiener filter with filter depth, M , is described by:

$$\hat{A}(n) = \sum_{i=0}^{M-1} a_i S(n-i) = \mathbf{a}^T \mathbf{S}, \quad (6.32)$$

where a_i are the filter coefficients. Both the filter coefficients and the input signal can be written as a vector: $\mathbf{a}^T = (a_0, \dots, a_{M-1})$ and $\mathbf{S}^T = (S(n), \dots, S(n-M+1))$. The error of the Wiener filter is defined as the difference between the desired output signal, $A(n)$, and the actual output signal, \hat{A} :

$$e_{\text{WF}}(n) = A(n) - \hat{A}(n) = A(n) - \mathbf{a}^T \mathbf{S}. \quad (6.33)$$

The desired output corresponds to the transverse energy, E_T , deposited in the LAr calorimeter. The next step is to minimize the average squared error by variation of the filter coefficients, \mathbf{a} :

$$\langle e_{\text{WF}}^2(n) \rangle = \langle (A(n) - \mathbf{a}^T \mathbf{S})^2 \rangle \quad (6.34)$$

$$= \langle A(n)^2 \rangle - 2\mathbf{a}^T \langle A(n) \mathbf{S} \rangle + \mathbf{a}^T \langle \mathbf{S} \mathbf{S}^T \rangle \mathbf{a} \quad (6.35)$$

$$= r_{AA}(0) - 2\mathbf{a}^T \mathbf{r}_{Ax} + \mathbf{a}^T \mathbf{R}_{xx} \mathbf{a}. \quad (6.36)$$

Here, $\mathbf{R}_{xx} = \langle \mathbf{S} \mathbf{S}^T \rangle$ denotes the $M \times M$ autocorrelation of the samples $S(n)$ and $\mathbf{r}_{Ax} = \langle A(n) \mathbf{S} \rangle$, the cross-correlation vector between the input signal and the desired output signal. The partial derivatives of the error $\langle e_{\text{WF}}^2(n) \rangle$ are set to zero with respect to the filter coefficients for all n :

$$\frac{\partial}{\partial \mathbf{a}} \langle e_{\text{WF}}^2(n) \rangle = 0 = -2\mathbf{r}_{Ax} + 2\mathbf{a}^T \mathbf{R}_{xx}. \quad (6.37)$$

Rearranging this equation leads to:

$$\mathbf{a}^T = \mathbf{R}_{xx}^{-1} \mathbf{r}_{Ax}. \quad (6.38)$$

With this, the filter coefficients of the Wiener filter can be calculated.

In general, A can have any shape. In this thesis, different desired output signal shapes are used. The base of all shapes is a single δ -peak. The amplitude of this peak corresponds to the deposited transverse energy. This peak can optionally be prepended with a pre-peak sample with half the amplitude of the peak or appended with a post-peak sample with half the amplitude of the peak. It is also possible to use both a pre-peak and a post-peak sample.

6.6. Wiener Filter with Forward Correction

An extension of the Wiener filter is the Wiener Filter with Forward Correction (WF_{FC}). The motivation behind it is to correct the undershoot of the bipolar pulse shape, as it can bias the pulse shapes of following signals. If the initial signal comes from a large energy deposition, the resulting pulse shape has a deep undershoot. In the worst case, the pulse shape of a following signal falls completely below the pedestal value.

The WF_{FC} consists of a Wiener filter with a peak and post-peak as desired output signal and the forward correction. The forward correction works in several steps:

1. If a correction exists for the analyzed sample, it gets applied.
2. The peak detection checks if a sequence of a peak followed by a post-peak is present. The criterion of the ratio of peak to post-peak is eased by a margin. For the ratio between post-peak and peak applies:

$$\frac{A_{\text{peak}}}{A_{\text{post-peak}}} = \frac{1}{2} - m. \quad (6.39)$$

The margin is usually set to $m = 0.15$ [125].

3. If the desired sequence is detected, the post-peak sample is reduced by half the peak amplitude. In addition, the calculation of the forward correction is initiated.
4. The correction is calculated based on the amplitude of the peak. The falling and rising edge of the undershoot are corrected by one FIR filter each. In the flat part of the undershoot, the correction is a constant term.

6. Digital Processing of Liquid-Argon Calorimeter Signals

As the WF_{FC} uses feedback from its output for its calculation, it is not an FIR filter but an IIR filter.

The implementation and stability of the WF_{FC} has been tested on an FPGA [126]. Furthermore, the WF_{FC} have been studied in multiple simulations [125, 127, 128].

7. Preparation of Liquid-Argon Demonstrator Data

This chapter summarizes the fundamentals of the LAr demonstrator analysis. In section 7.1, the trigger coverage is described. A short overview of the used datasets is given in section 7.2. In section 7.3, the process of energy reconstruction is explained.

Before an analysis, the pedestal value and the sample of the peak of the pulse are determined for each supercell. This preprocessing of the LAr demonstrator datasets is introduced in section 7.4. In section 7.5, irregular signals that are recorded in some events are shown.

7.1. Trigger Coverage

Two dedicated trigger items for the LAr demonstrator have been included in the L1Topo trigger. The objective was to record electromagnetic and hadronic showers with a high E_T within the region of the LAr demonstrator.

The trigger items select electromagnetic showers with $E_T > 20$ GeV and hadronic showers with $E_T > 100$ GeV in a region of $0 < \eta < 1.5$ ($0 < \eta < 1.4$ for hadronic showers) and $\frac{16}{32} \cdot \pi < \phi < \frac{23}{32} \cdot \pi$ in the EMB [129]. Due to the prescaling of the trigger items, the resulting trigger rate is about 1 Hz.

When the condition of a trigger item is met, the L1Topo trigger sends the L1A signal and the Trigger Type (TType) to the trigger, timing, and control system, which distributes it to the ABBAs to read out the data.

The L1A signal has just a single bit. The TType has 8 bit, see table 7.1. Out of the eight bits, the following three are important for the readout of the LAr demonstrator:

- If **bit 7** is set, the ATLAS detector is in physics mode, in contrast to the calibration mode.
- If **bit 4** is set, the trigger was caused by an energy deposition in the LAr demonstrator region.

7. Preparation of Liquid-Argon Demonstrator Data

Table 7.1.: The bits of the TType and their meaning [130].

Sub-Trigger	Physics	ALFA ¹	FTK ²	LAr demonstrator
bit	7	6	5	4
Sub-Trigger	Muons	Calorimeter	ZeroBias ³	Random
bit	3	2	1	0

- If **bit 2** is set, the trigger was caused by an energy deposition in the calorimeter.

The requirement for the ABBAs to be read out is that bit 7 and bit 4 are set. Hence, any combination including these two bits is sufficient. The majority of the recorded events have 0x90 and 0x94 as TType.

In fig. 7.1a, an exemplary distribution of the transverse momentum, p_T , of recorded electrons during run⁴ 334 487 (recorded 30 July 2017) is shown. In fig. 7.1b, the η and ϕ distribution of the recorded electrons with $p_T > 20$ GeV is shown.

¹ALFA [131] stands for *Absolute Luminosity for ATLAS*. The ALFA detector is located 240 m from the interaction point of the ATLAS detector and is designed to measure elastic pp collisions at small angles.

²The Fast Tracker (FTK) [132] project has been canceled recently [133].

³A recorded event of a bunch crossing with no further requirements.

⁴In the following, the term *run* refers to a period of data taking.

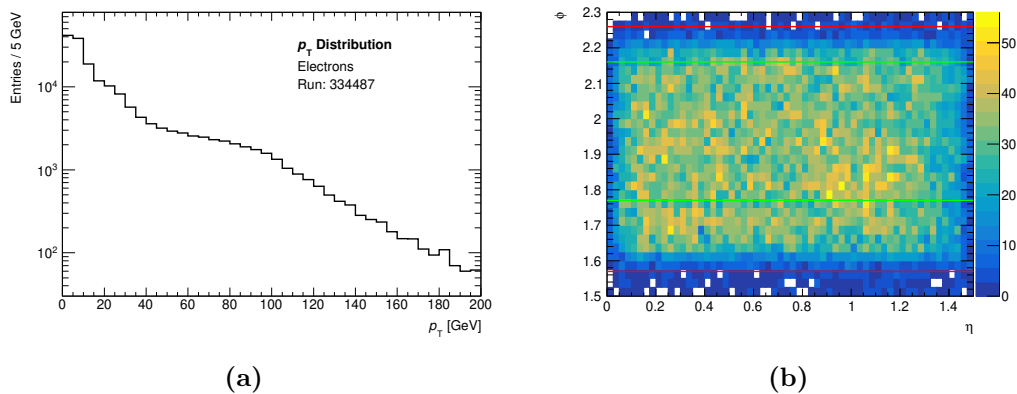


Figure 7.1.: In the left figure, the p_T distribution of the electrons recorded by the LAr demonstrator for run 334 487 is displayed. The right figure shows the η and ϕ distribution of the electrons ($p_T > 20$ GeV). Both the trigger coverage (red) and the region of the LAr demonstrator (green) are highlighted. The information on the electrons are included in the dataset of the main readout (see section 8.1).

7.2. The Datasets

7.2.1. Dataset of the Main Readout

The datasets of the main readout are already processed by the ATLAS reconstruction software. The process is briefly explained.

From the raw data of the main readout so-called Event Summary Data (ESD) files are produced. ESD files contain the detailed output of the reconstructed events. In the next step, Analysis Object Data (AOD) files are produced from the ESD files. AOD files contain reduced information of the reconstructed event, which is sufficient for most analyses. During this process, only cells that are neighboring the cell with the highest energy deposition are kept [134–136].

The AOD files are converted to ROOT⁵ [137] files. This conversion process is also used to build the supercells by summing up the corresponding elementary cells. The mentioned reduction in information leads to a potential underestimation of the energies of the supercells at the edges of the energy deposition.

The ROOT files of the main readout contain several quantities. For the analysis, the following quantities are important:

- **BCID:** The number of possible bunch crossings is 3564 (see section 3.1). The

⁵ROOT is a data analysis framework developed by CERN.

Bunch-Crossing Identification (BCID) denotes every bunch with the corresponding number (0–3563). It is not unique, as it gets reset after one bunch revolution.

- **BCTime**: The time in seconds starting from 1 January 1900 (epoch of the Network Time Protocol [138]).
- **BCTimeNS**: The offset to the last full second of the BCTime in nanoseconds.
- **L1ID**: The Level-1 Identification (L1ID) is a 32-bit number. It consists of a 24-bit event counter which is increased for each L1A signal. The event counter gets periodically reset. These resets are registered by the 8-bit event counter reset counter [139].
- **SC E**: The energy of the supercell in MeV.
- **SC Et**: The transverse energy of the supercell in MeV.
- **SC Eta**: The η -coordinate of the supercell.
- **SC ID**: The supercell identifier is a 32-bit number that holds information about the position of the readout channel in the ATLAS detector. Each readout channel in the ATLAS detector is related to a unique identifier. More information can be found in [140].
- **SC Phi**: The ϕ -coordinate of the supercell.
- **SC Sampling**: The detector layer of the supercell.
- **TType**: See section 7.1.
- **Trigger Item**: See section 7.1.
- **Different Reconstruction Variables**: Information on the reconstructed particles, which is explained in section 8.1.

7.2.2. Dataset of the LAr Demonstrator

The data that are read out from the ABBAs are recorded in ROOT files. While usually only four samples of the peak of the pulse are recorded in the main readout of the LAr calorimeter, the ABBAs allow recording of 50 samples. The pulses are recorded in a way that the peak is around the 22nd sample.

Table 7.2.: The relation between the source ID, the ABBA FPGA, the ϕ -slice, i_ϕ , and the LTDB type [130]. The first item of the ABBA FPGA is the last number of the IP address, the second item is the UDP port. The LTDBs types are named after the institutes that built the boards: Brookhaven National Laboratory (BNL) and Laboratoire de l'Accelérateur Lineaire and Saclay (LAL/Saclay).

Source ID	ABBA FPGA	i_ϕ	LTDB
0x410512	19:2	18	BNL
0x410511	20:2	19	BNL
0x410521	19:1	20	LAL/Saclay
0x410522	18:2	21	LAL/Saclay

The ROOT files of the LAr demonstrator contain several quantities. For the analysis the following quantities are important:

- **ADC:** For each channel, the raw ADC samples are stored.
- **BCID:** See section 7.2.1.
- **L1ID:** See section 7.2.1.
- **SourceID:** The identifier is a 32-bit number that relates to an FPGA on the ABBA. More details on the relation are in table 7.2.
- **TimeStamp:** See BCTime in section 7.2.1.
- **TimeStampOffset:** See BCTimeNS in section 7.2.1.
- **TType:** See section 7.1.

7.3. Energy Reconstruction

Different filter algorithms are used to reconstruct the energy from the ADC samples⁶. Besides the filter coefficients, further constants⁷ for each supercell are needed: the pedestal value, p , the conversion factor, f_{conv} , to calculate the energy in MeV from the ADC counts, and the high voltage correction factor, f_{HV} . If the high voltage of a

⁶If not stated otherwise an Optimal Filter is used for the energy reconstruction.

⁷More information about these constants can be found in appendix A.1.

cell does not correspond to the nominal value a correction factor is applied. For cells with the nominal high voltage, this factor is 1.

The filter coefficients of the Optimal Filter are derived with the ATHENA⁸ [141] framework. Together with the pedestal values, the conversion factors, and the high voltage correction factors, they are taken from [142]. Because these constants were determined for run 334 487, the majority of the studies in this thesis uses this run.

The actual reconstruction of the energy from the ADC samples, S_i , involves several steps:

1. The pedestal value, p , is subtracted from each sample.
2. Each sample is multiplied with the conversion factor, f_{conv} , to translate the ADC counts to MeV.
3. Each sample is multiplied with the high voltage correction factor, f_{HV} . These first steps lead to:

$$S_{i,\text{mod}} = (S_i - p) \cdot f_{\text{conv}} \cdot f_{\text{HV}}. \quad (7.1)$$

4. A filter algorithm is applied to the modified ADC samples, $S_{i,\text{mod}}$.

In fig. 7.2, an example of the response of an Optimal Filter applied on a sampled pulse shape is shown. Because the Optimal Filter is set up with 5 filter coefficients, the resulting filter response consists of 46 samples.

⁸The ATHENA framework is the official ATLAS software.

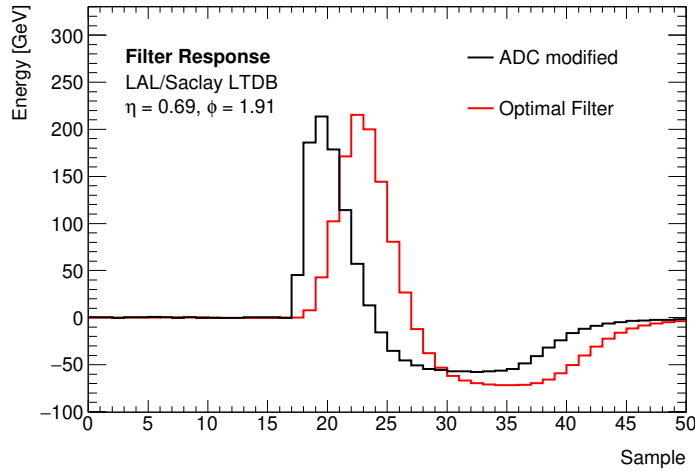


Figure 7.2.: In black the ADC samples are displayed. The samples are already modified (pedestal value subtracted, ADC to MeV conversion factor and high voltage correction factor applied). The response of an Optimal Filter is drawn in red. It is shifted by 5 samples for reasons of comparability to the ADC samples.

7.4. Preparation for the Data Analysis

7.4.1. Pedestal Value Adjustment

For the energy reconstruction, it is important to know the value of the pedestal for each supercell. But studies of the pedestal values indicate that they are not fully stable and may change from run to run. Hence, the predetermined pedestal values of each supercell are checked before analyzing the data. If necessary, the pedestal values are adjusted.

The process of checking the pedestal values has two steps. It is done on the unmodified ADC samples. First, the mean, \bar{S} , and the standard deviation, $\sigma_{\bar{S}}$, of the 50 samples of one event are determined. If $\sigma_{\bar{S}} < 1$ for the BNL LTDB and $\sigma_{\bar{S}} < 1.5$ for the LAL/Saclay LTDB, the difference, $\Delta_{\bar{S},p}$, between the mean and the predetermined pedestal value is recorded, else it is discarded. This process is done for each event of a run.

In the second step, the mean, $\bar{\Delta}_{\bar{S},p}$, and the standard deviation, σ_{Δ} , of the recorded

$\Delta_{\bar{s},p}$ values are calculated for each supercell. Because the number of recorded $\Delta_{\bar{s},p}$ values may vary for the different supercells, the maximum number of entries for a single supercell in each detector layer is determined. The predetermined pedestal value is adjusted by $\bar{\Delta}_{\bar{s},p}$ if the following conditions are met:

- At least 5% of the maximum number of recorded $\Delta_{\bar{s},p}$ values by a supercell in the same detector layer,
- and $\sigma_{\Delta} < 1$.

In addition, it is checked if $\sigma_{\Delta} < 2$, else the supercell is excluded from analysis, as the pedestal is expected to be unstable. Furthermore, supercells with a $\bar{\Delta}_{\bar{s},p} > 100$ ADC counts are excluded.

7.4.2. Peak Sample Identification

In addition to the pedestal values, the usual sample of the peak, S_{peak} , is determined for each supercell. The supercells are expected to have the peak of the recorded pulse shape in a certain, fixed sample. This peak is supposed to be in the 22nd sample. Again, studies indicate that it does not hold up for each supercell and may change from run to run due to the instability of the prototype electronics.

The process of determining the sample of the peak takes only events with an energy that is above 2 GeV into account. To ensure that higher energy depositions have a bigger impact on the determination of the sample of the peak, the sample weighted with the height, h , of the peak is recorded for each event. The height is the ADC count minus the corresponding pedestal value:

$$h = S_i - p. \tag{7.2}$$

This process results in a histogram for each supercell (see fig. 7.3). Though the largest sum is in sample 20, a small part of the depositions is in sample 21. Hence, it has to be considered that the peak sample may vary.

The histograms are analyzed for each supercell. If the histogram has at least 5% of the maximum number of recorded $\Delta_{\bar{s},p}$ values by a supercell in the same detector layer, the bin of the histogram with the largest sum is set as S_{peak} of the supercell. Else, S_{peak} is not set.

Next, the most frequent peak sample per LTDB is determined. If S_{peak} is not set, its peak sample is set to the most frequent one.

Figure 7.4 shows the histogram of the S_{peak} for each LTDB for run 334487. The most supercells have an S_{peak} around sample 20.

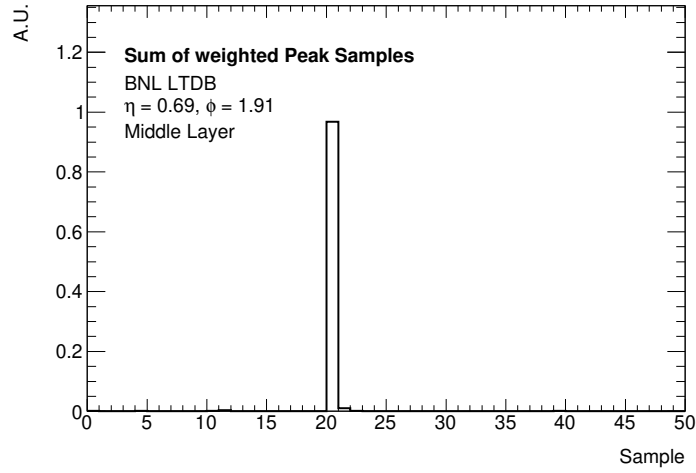


Figure 7.3.: For each supercell, the sample of the peak weighted with the height is recorded. As an example, the distribution for a supercell for run 334487 is shown.

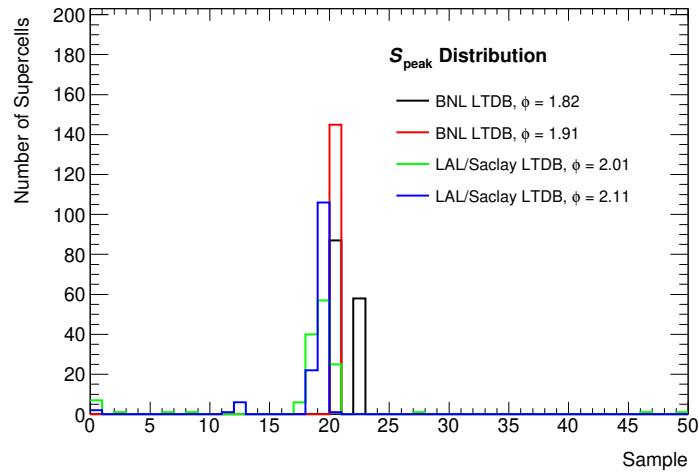


Figure 7.4.: Distribution of S_{peak} of the supercells for each LTDB for run 334487. The majority of the peak samples is around sample 20.

7.5. Irregular Signals

Some issues in the LAr demonstrator data lead to an exclusion of an event. In the worst case, a supercell is excluded for the full run. In general, there are known problematic supercells (see [130]) that are excluded from the analysis. But in some cases, problems occur during the runs and lead to irregularities in the data. These irregularities need to be identified to exclude the events from the analysis. In the following, some detected issues are introduced.

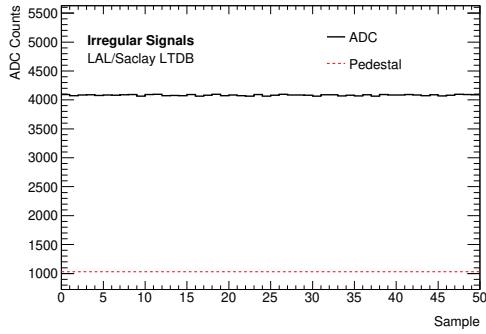
- The baseline is shifted and takes on an (almost) constant value which is either much higher or lower than the pedestal (see fig. 7.5).
- Figure 7.6a shows an irregular response of the analog shaper to a delta peak. The delta peak is injected in the readout chain before the shaper.
- Every 3564 bunch crossings⁹, the LTDBs are expected to send the so-called K comma symbol¹⁰ to the ABBAs. This K code is sent to synchronize the sender and the receiver. If the ABBA does not receive the K code the fiber between the LTDB and the ABBA is unlocked. Therefore, the ABBA overwrites the received data with an unlocked pattern [130].

An example of the unlocked pattern is shown in fig. 7.6b.

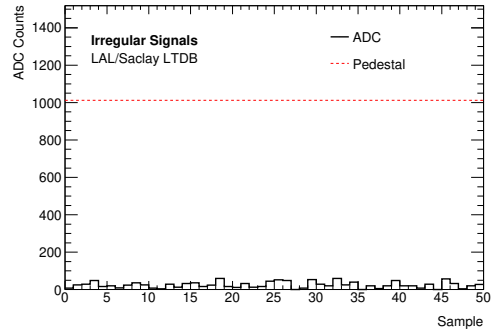
- The entire pulse of an energy deposition has to be recorded for the energy reconstruction to work. If a pulse is at the beginning or the end of 50 samples, the energy can not be reconstructed. Some examples are displayed in fig. 7.7.
- There are many other anomalies in the recorded data. Some are shown in fig. 7.8.

⁹3564 bunch crossings correspond to one bunch revelation.

¹⁰Also referred to as *K code*.

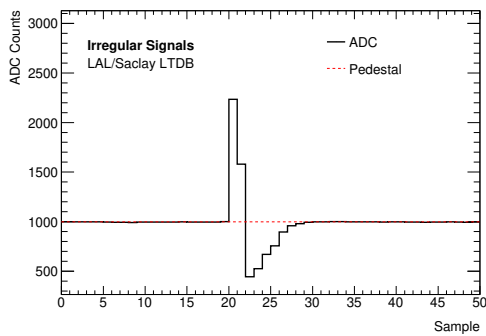


(a)

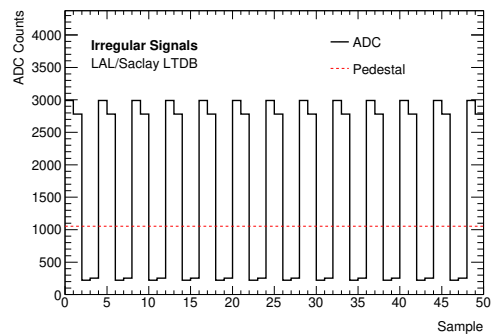


(b)

Figure 7.5.: A shifted baseline with a value much higher or lower than the pedestal value.



(a)



(b)

Figure 7.6.: In the left figure, the response of the analog shaper to an injected delta peak is displayed. The right figure shows the unlocked-fiber pattern of the ABBA. These events are excluded from further analysis.

7. Preparation of Liquid-Argon Demonstrator Data

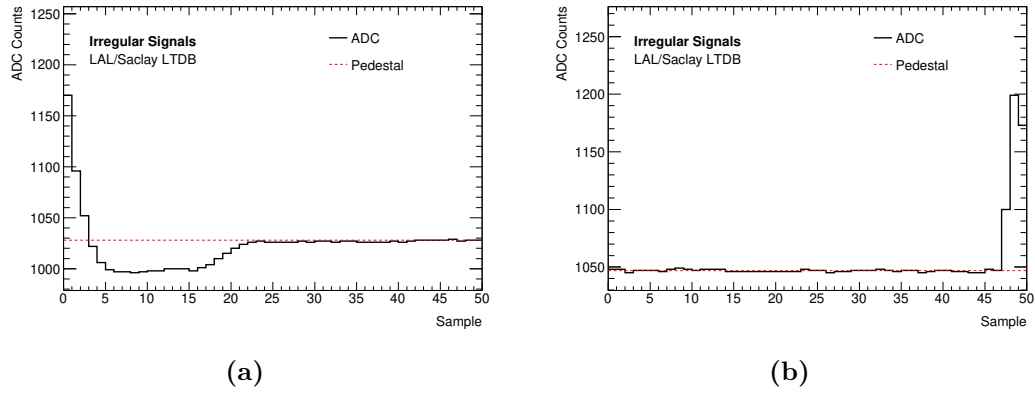


Figure 7.7.: Pulses at the beginning or the end of the 50 samples that are not fully recorded. These pulses are excluded from further analysis.

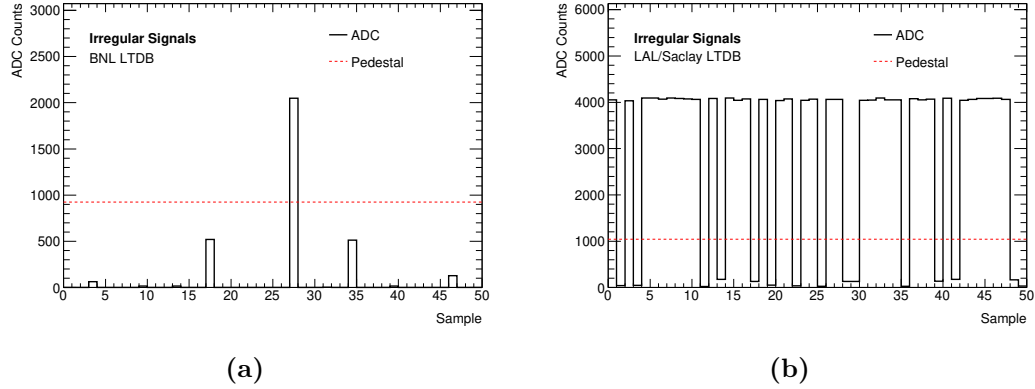


Figure 7.8.: Anomalies in the recorded data. Such events are excluded from further analysis.

8. Studies of the Shower-Shape Variables

The following chapter presents a study of the background rejection power of the shower-shape variables introduced in section 5.3.5.

While both the LAr demonstrator and the main readout cover the same energy range, the main readout has a dynamic gain selection. With the highest of the three different gains, a high precision is achieved at lower energies. For this reason, the results of the main readout serve as a reference.

In section 8.1, definitions for the particle identification are introduced. Section 8.2 explains the matching process between the LAr demonstrator and the main readout datasets. After this, the energy distribution of the supercell with the highest energy deposition in the middle layer, the *hottest* supercell, is studied in section 8.3. In sections 8.4 to 8.6, the performance of the shower-shape variables is investigated, with each section focusing on one variable. In section 8.7, the results of this study are compared with the results from simulations presented in [113].

8.1. Particle Identification

To study the background rejection power of the three shower-shape variables, the particle that produced the shower must be known. The main readout data files that are produced by the ATLAS reconstruction software contain further information on identified particles. Possible particle types are electrons, photons, muons, tau leptons, and hadronic jets. For each type, the transverse momentum, p_T , the transverse energy, E_T , and the ϕ and η coordinates are included. As the studies focus on electrons and jets, the other particle types are not discussed further.

For each electron candidate, the pass/fail status with respect to the three sets of criteria are recorded. A full description of the sets can be found in [143]. In the following, a short summary is presented. The three sets of cut criteria are in order of increasing background rejection power:

- The **loose** set cuts on hadronic leakage variables that compare the ratio between

E_T in the Tile calorimeter and E_T in the LAr calorimeter. Cuts on shower-shape variables for the middle layer are included as well.

- The **medium** set contains all cuts from the loose set. It also includes cuts on shower-shape variables for the presampler, cuts on track quality variables¹, and cuts on the track-cluster matching.
- The **tight** set contains all cuts from the medium set. It also includes further cuts on the track quality and the track-cluster matching, as well as particle identification variables using information from the transition-radiation tracker.

For the Phase-I studies in [113], the tight cuts are used, together with a $p_T > 20$ GeV cut on the electron momentum. The same cuts are used here.

Jets are identified with the anti- k_t clustering algorithm [144] with a distance parameter of $R = 0.4$. In addition, a 20 GeV cut on the transverse momentum of the jet is applied.

In order to associate a particle with an event, the ϕ and η coordinates must be within the hottest supercell or one of its neighbors. If neither an electron nor a jet is assigned to an event, it is discarded. To use the particle information of the main readout for the LAr demonstrator, the events of the two datasets need to be matched.

8.2. Matching of Main Readout and Demonstrator Data

The matching process uses the L1ID, the BCID, and the TType. In total, over 3 million LAr demonstrator events are studied. About 96% of these events are matched with main readout events.

To verify the matching process, the energy depositions in four supercells (one per detector layer) are compared. The data are taken from run 334 487. Figure 8.1 shows the correlation between the LAr demonstrator and the main readout. In general, all four supercells show a good correlation between the transverse energy deposited in the LAr demonstrator and the main readout. Only for $E_T < 1$ GeV differences are visible.

Next, the signal detection efficiency is investigated for different energy ranges. The

¹Which are related to the number of hits in the inner detector.

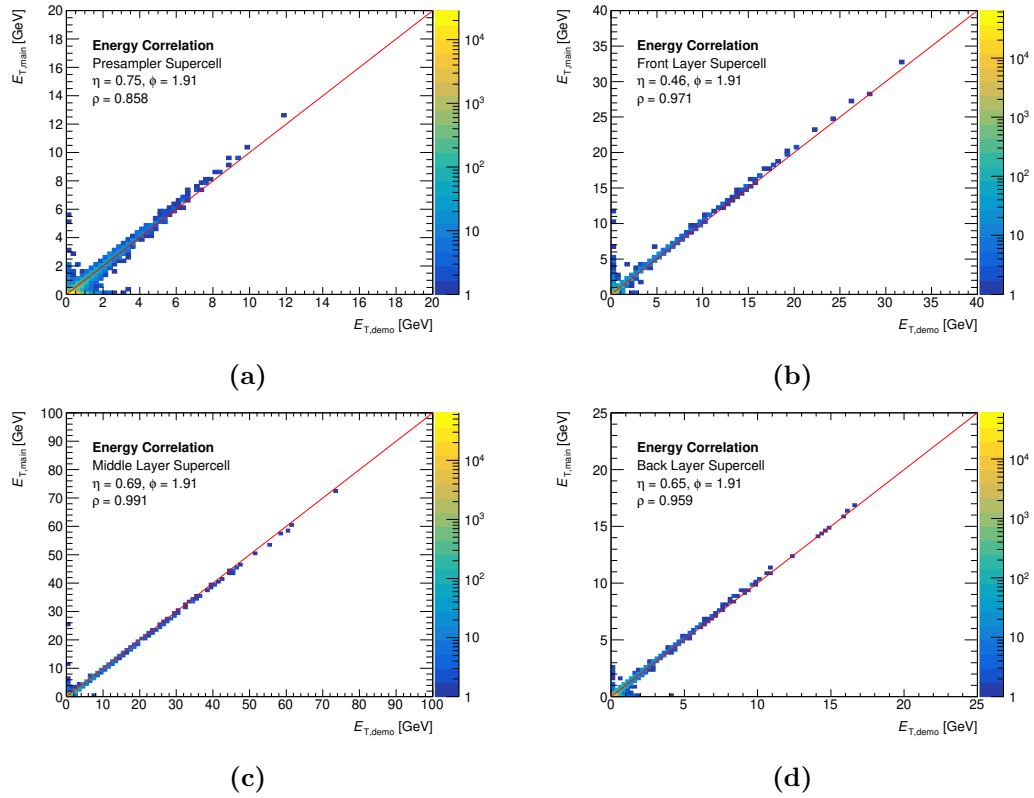


Figure 8.1.: Correlation, ρ , between the transverse energy deposited in the LAr demonstrator and the main readout for four supercells. For energies above 1 GeV, all detector layers show a good correlation.

8. Studies of the Shower-Shape Variables

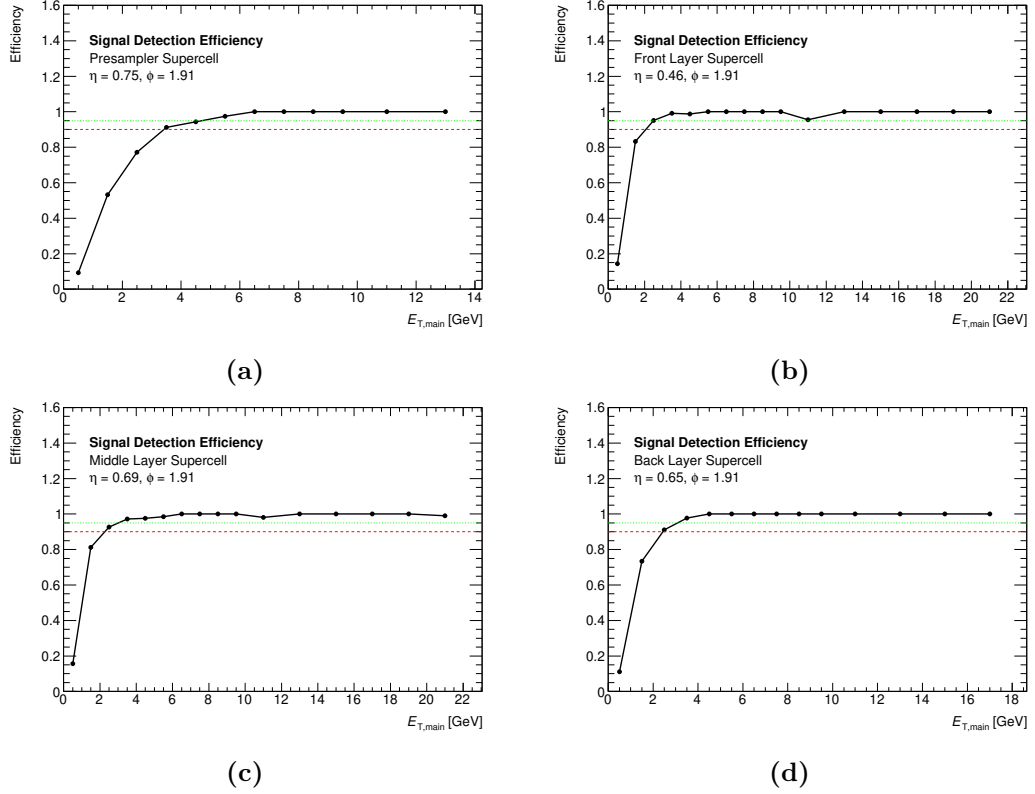


Figure 8.2.: Signal detection efficiency of four supercells. The energies below 10 GeV are summed up in intervals with a width of 1 GeV. Between 10 GeV and 20 GeV, the intervals have a width of 2 GeV. In the front layer and the middle layer, energies above 20 GeV are summed up in the last point.

following criterion has to be fulfilled for a signal to be detected:

$$\Delta E_{\text{rel}} = \left| \frac{E_{T,\text{demo}} - E_{T,\text{main}}}{E_{T,\text{main}}} \right| < 0.1 \quad (8.1)$$

where ΔE_{rel} is the relative energy difference, $E_{T,\text{demo}}$ is the transverse energy deposited in the supercell of the LAr demonstrator, and $E_{T,\text{main}}$ the summed transverse energies in the corresponding elementary cells of the main readout. In fig. 8.2, the signal detection efficiency of this procedure is shown for the same four supercells as before.

While the front layer, the middle layer, and the back layer reach a signal detection efficiency of 90 % for $E_T > 2$ GeV, the presampler only reaches this threshold at 3 GeV.

This is in agreement with the observations regarding the energy correlation. The difference for small energies has to be taken into account when comparing the shower-shape variables calculated for the main readout with those for the LAr demonstrator.

Finally, the energy depositions of a shower as seen by the LAr demonstrator and the main readout are compared. An event with $E_T > 200$ GeV in the hottest supercell is displayed in fig. 8.3. For the hottest supercell and the neighboring supercells in η direction, the energy depositions show a good agreement. Nonetheless, certain differences are visible. As described in section 7.2, the amount of recorded data in the main readout is reduced. Only the energy information of the supercells in the region of the hottest supercell are included. For some events, this has an impact on the calculated energy of the 7×2 cluster of R_η , for example.

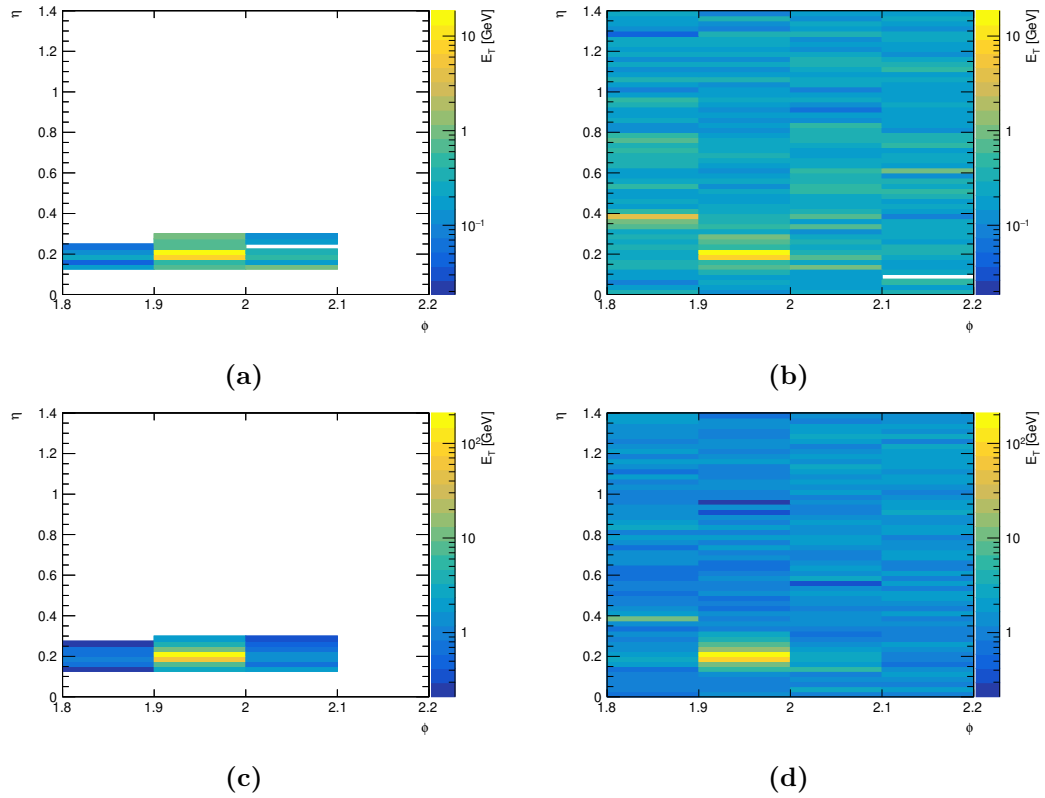


Figure 8.3.: Shower distribution of a matched event. On the left are the distributions in the main readout, on the right the ones of the LAr demonstrator. Figures (a) and (b) display the distributions in the front layer. Figures (c) and (d) display the distributions in the middle layer. In the region of the energy deposition, they show good agreement.

8.3. Energy Distribution of the Hottest Supercell

The starting point for the calculation of all three shower-shape variables is the hottest supercell in the middle layer. In both readouts, this supercell is required to have a minimum energy deposition of $E_T > 4$ GeV. The energy distribution of the hottest supercell in the middle layer is displayed in fig. 8.4 for electrons and jets. In total, about 1 million events are used for studies of the shower-shape variables.

The energy distributions of the electrons and the jets show a good agreement. Next, the coordinates of the hottest supercell for the LAr demonstrator and the main readout are compared. The difference in terms of units of the supercell width is shown in fig. 8.5.

For the majority of the events, the hottest supercells are the same for the LAr demonstrator and the main readout; both for electrons and jets, the fraction of the events with different coordinates of the hottest supercell is below 1 %.

For the following studies, two more cuts are applied to the LAr demonstrator and the main readout: the hottest supercell must be in a ϕ -slices with $i_\phi = 19$ or $i_\phi = 20$. Further, the range of the possible η -slices, i_η , is limited to $i_\phi = 3$ –52. When calculating f_3 in section 8.5, the η -range is reduced $i_\phi = 4$ –51.

8. Studies of the Shower-Shape Variables

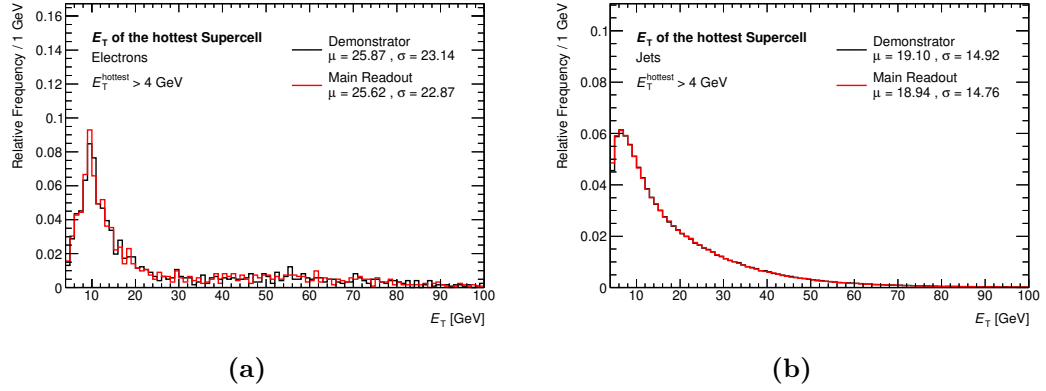


Figure 8.4.: Energy distribution of the hottest supercell in the middle layer. The left figure shows the distribution for electrons, the right for jets. On both, an energy cut of 4 GeV is applied.

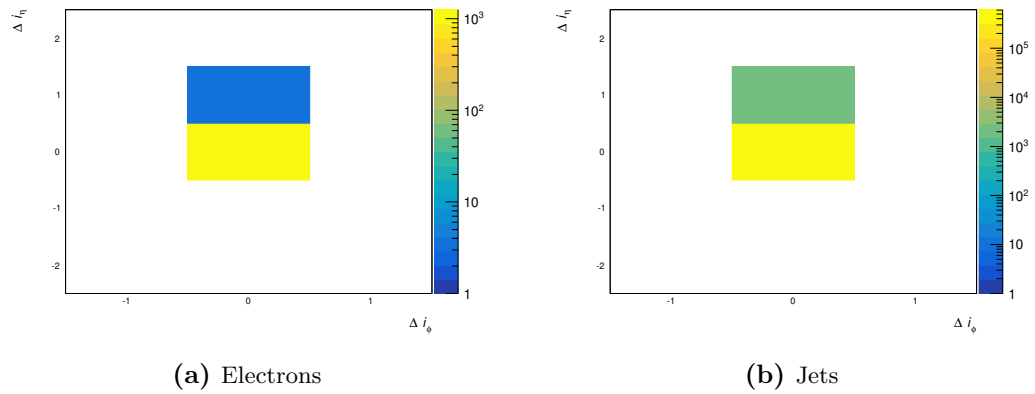


Figure 8.5.: Difference in the coordinates of the hottest supercell of the LAR demonstrator and the main readout. The difference is given in units of the supercell width.

8.4. Studies of the Shower-Shape variable R_η

The first shower-shape variable that is studied is the energy ratio, R_η . The definition can be found in eq. (5.1). Jets are expected to form a broader shower in the LAr calorimeter as compared to electrons.

Figure 8.6 shows the R_η distribution for electrons and jets.

For the electrons, the R_η distribution of the main readout shows the expected narrow shape shifted towards 1. The R_η distribution of the LAr demonstrator is slightly broader and tends to lower R_η values.

As predicted by the simulations, the distributions of the jets show a broad shape. Both distributions are very similar.

To further investigate the differences for electrons, the energy depositions in the 3×2 cluster are compared between the LAr demonstrator and the main readout in fig. 8.7. The energy depositions in the 7×2 cluster are shown in fig. 8.8.

For the 3×2 cluster, the distributions of both the electrons and the jets show a good agreement. This confirms the results shown in fig. 8.3. For the hottest supercell and the closest neighboring supercells, the energy depositions are very similar.

While for the 7×2 cluster, the distributions of the LAr demonstrator and the main readout for electrons and jets are very similar, a slight shift of the distribution of the LAr demonstrator with respect to the main readout is visible.

The difference becomes more apparent when comparing the ratio between the energy in the outer part of the 7×2 cluster, which is $E_{T,7 \times 2} - E_{T,3 \times 2}$, and the energy of the 3×2 cluster. Figure 8.9 shows the ratios for electrons and jets. The ratio for the jets of the LAr demonstrator shows a slight shift with respect to the main readout. For the electrons, a clear difference is visible. The ratio of the energy depositions in the outer part of the 7×2 cluster is almost double for the LAr demonstrator compared to the main readout. This has an impact on the R_η value and is responsible for the difference in the R_η distribution of the LAr demonstrator and the main readout.

The reason is the better energy resolution of supercells of the main readout which are summed up from individual elementary cells. These elementary cells have a lower least significant bit compared to the supercells read out by the LAr demonstrator. The least significant bit of elementary cells in the middle layer is in the order of $1/8$ of the noise level. For the supercells of the LAr demonstrator, the least significant bit is in the order of the noise level.

8. Studies of the Shower-Shape Variables

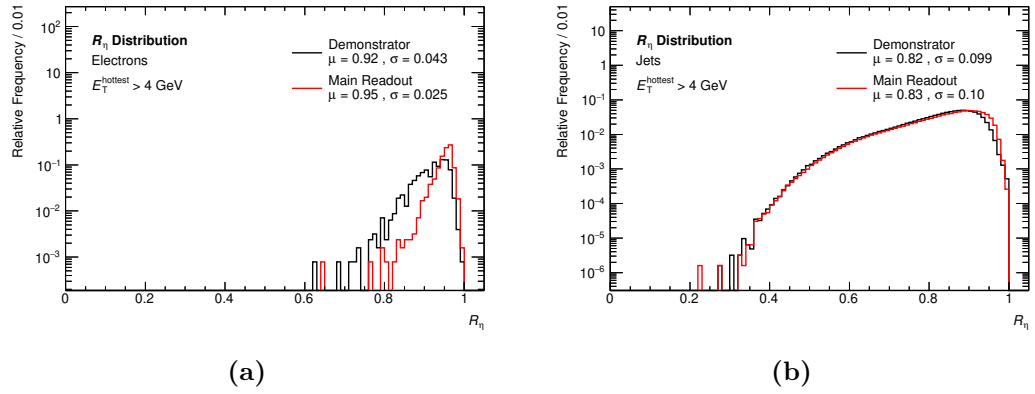


Figure 8.6.: Comparison of the R_n distribution for electrons and jets between the LAr demonstrator and the main readout.

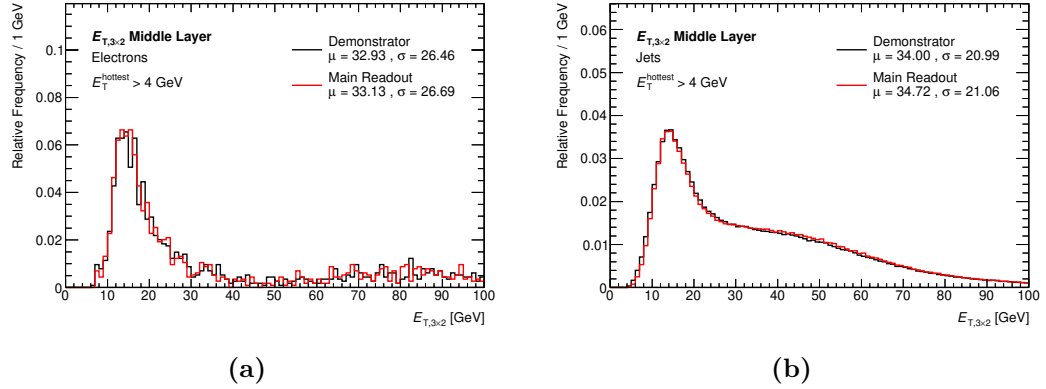


Figure 8.7.: Comparison of the energy distribution in the 3×2 cluster for electrons and jets between the LAr demonstrator and the main readout.

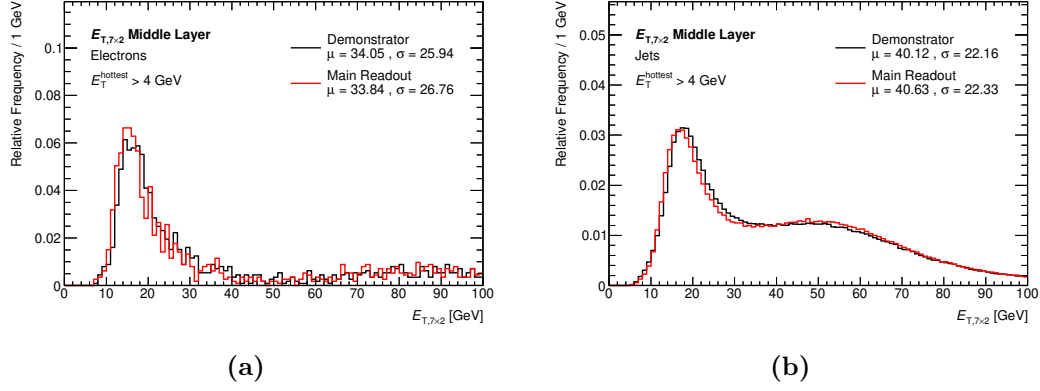


Figure 8.8.: Comparison of the energy distribution in the 7×2 cluster for electrons and jets between the LAr demonstrator and the main readout.

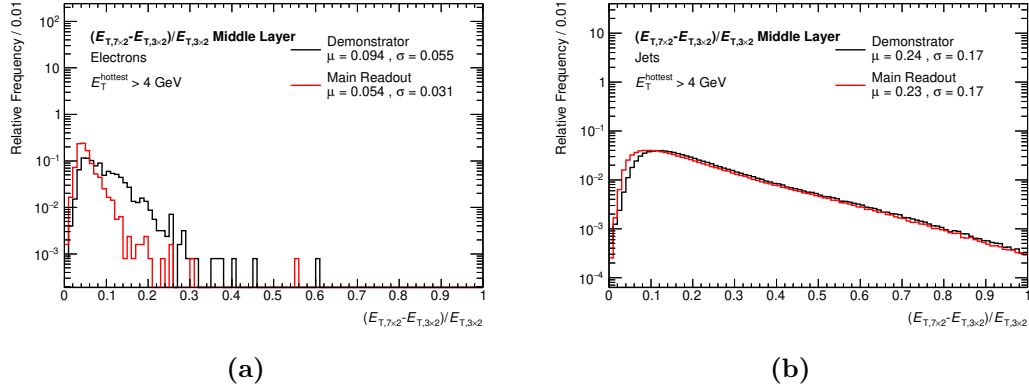


Figure 8.9.: Comparison of the ratio between the energy in the outer part of the 7×2 cluster and the energy of the 3×2 cluster for electrons and jets.

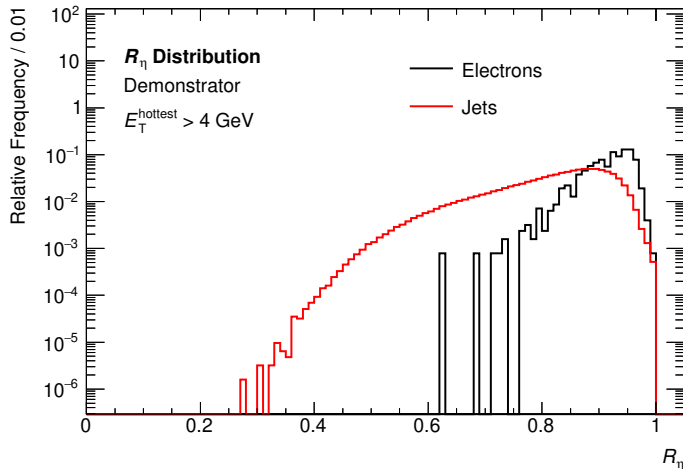


Figure 8.10.: Comparison of the R_η distribution for electrons and jets for the LAr demonstrator.

The background rejection power of R_η for the LAr demonstrator is compared in fig. 8.10. In direct comparison, the expected differences are visible. The peak of the R_η distribution of the electrons is shifted towards 1, while the peak of the jets is around 0.8. In addition, the distribution of the electrons is more narrow compared to the broad, almost flat distribution of the jets.

To evaluate the background rejection power, the cut efficiency, ϵ_{cut} , is determined. It is defined as:

$$\epsilon_{\text{cut}} = \int_x^1 f(R_\eta) dR_\eta, \quad (8.2)$$

where $f(R_\eta)$ is the relative frequency of R_η , and x is the cut value. The background rejection power is defined as $1 - \epsilon_{\text{cut}}^{\text{Jets}}$ over the cut efficiency of the signal, $\epsilon_{\text{cut}}^{\text{e}}$, which is called trigger efficiency. Both the cut efficiencies for electrons and jets and the background rejection power are shown in fig. 8.11.

The cut efficiency for electrons and jets is 1 for small R_η values. For jets, the cut efficiency starts decreasing for $R_\eta > 0.55$. While for electrons, the decrease starts for $R_\eta > 0.85$. The background rejection power is about 60 % (50 %) for a desired trigger efficiency of 90 % (95 %). With the R_η distributions of the main readout², a background rejection power of about 82 % (75 %) can be achieved.

²See appendix A.2

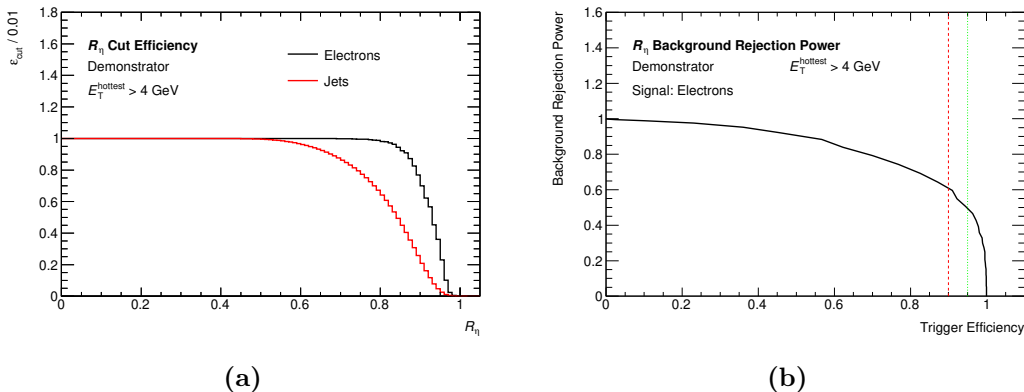


Figure 8.11.: Cut efficiencies for electrons and jets and the background rejection power. For the background rejection power on the right, 90 % (red) and 95 % (green) trigger efficiency are marked.

8.5. Studies of the Shower-Shape variable f_3

The definition of the energy fraction in the back layer, f_3 , can be found in eq. (5.2). Compared to electrons, jets are expected to deposit a higher fraction of their energy in the back layer.

Figure 8.12 shows the distributions of f_3 for electrons and jets for the LAr demonstrator and the main readout. The f_3 distribution for electrons shows the expected narrow shape which is shifted towards zero. In the LAr demonstrator, the distribution is slightly broader than in the main readout.

For the jets, the f_3 is much broader and slowly decays towards higher values. The distributions of the LAr demonstrator and the main readout show a good agreement.

To examine the differences in the distributions, the energy depositions in the 3×2 cluster in the front layer are compared for the LAr demonstrator and the main readout (see fig. 8.13). The energy depositions in the 2×2 cluster in the back layer are shown in fig. 8.14. The 3×2 cluster of the middle layer is already examined in section 8.4. In the front layer, the distributions of electrons and jets show good agreement between the LAr demonstrator and the main readout. In the 2×2 cluster in the back layer, the mean and standard deviation values for the LAr demonstrator and the main readout differ for electrons. This leads to the difference in the f_3 distributions for the LAr demonstrator and the main readout. For jets, the energy distributions of the 2×2 cluster in the back layer show a good agreement.

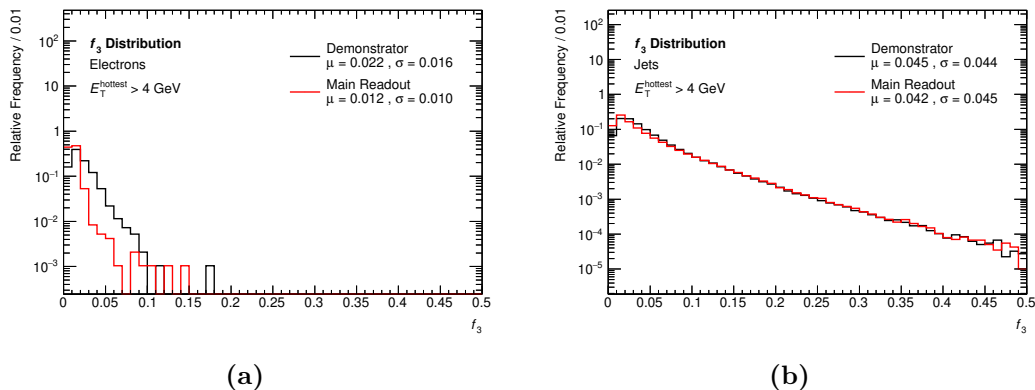


Figure 8.12.: Comparison of the f_3 distribution for electrons and jets between the LAr demonstrator and the main readout.

The background rejection power of f_3 for the LAr demonstrator is compared in fig. 8.15. The comparison of the f_3 distributions of the LAr demonstrator and the main readout exhibits the expected differences between them. The narrow distribution of the electrons is clearly distinguishable from the broader shape of the jet distribution.

The definition of the cut efficiency for f_3 differs from the one for R_η as the cut direction is reversed. It is defined as:

$$\epsilon_{\text{cut}} = \int_0^x f(f_3) df_3, \quad (8.3)$$

where $f(f_3)$ is the relative frequency of f_3 , and x is the cut value. Again, the background rejection power is defined as $1 - \epsilon_{\text{cut}}^{\text{Jets}}$ over the trigger efficiency, ϵ_{cut}^e . Both the cut efficiencies for electrons and jets and the background rejection power are shown in fig. 8.16.

For electrons, the cut efficiency is a bit steeper for low f_3 values and converges to 1 for $f_3 > 0.1$. The curve of the cut efficiency for jets is a bit flatter and gets close to 1 for cuts on $f_3 > 0.2$. The background rejection power is about 37 % (30 %) for a desired trigger efficiency of 90 % (95 %). With the f_3 distributions of the main readout³, a background rejection power of about 62 % (52 %) can be achieved.

³See appendix A.2

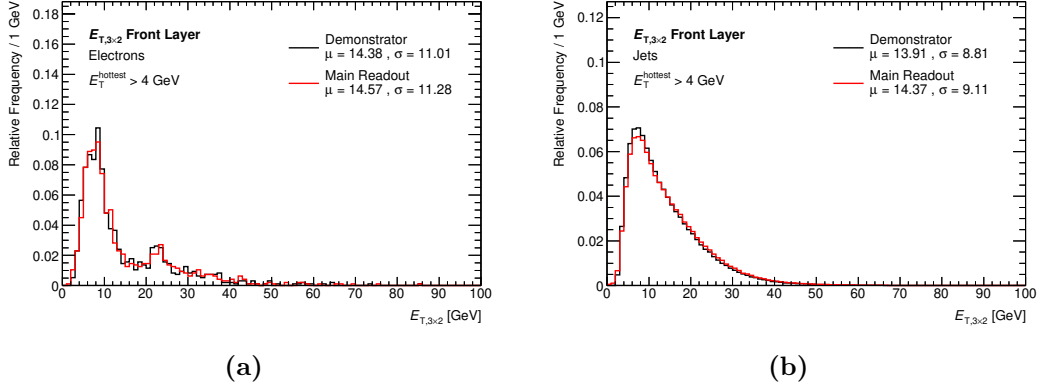


Figure 8.13.: Comparison of the energy distribution in the 3×2 cluster for electrons and jets between the LAr demonstrator and the main readout in the front layer.

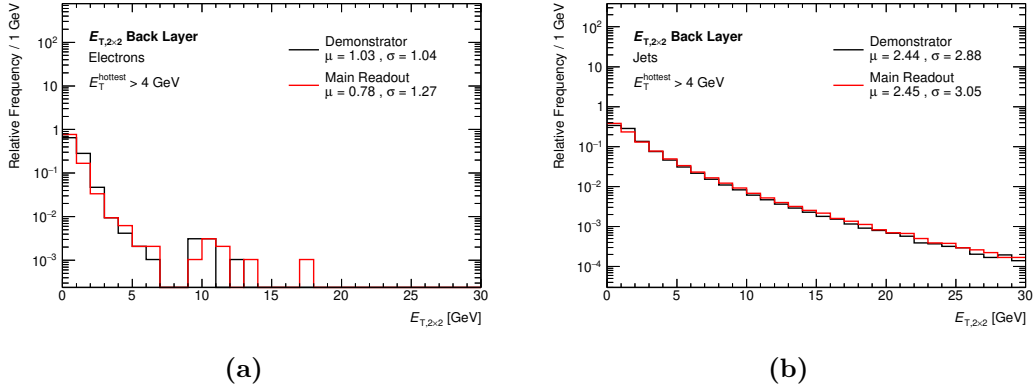


Figure 8.14.: Comparison of the energy distribution in the 2×2 cluster for electrons and jets between the LAr demonstrator and the main readout in the back layer.

8. Studies of the Shower-Shape Variables

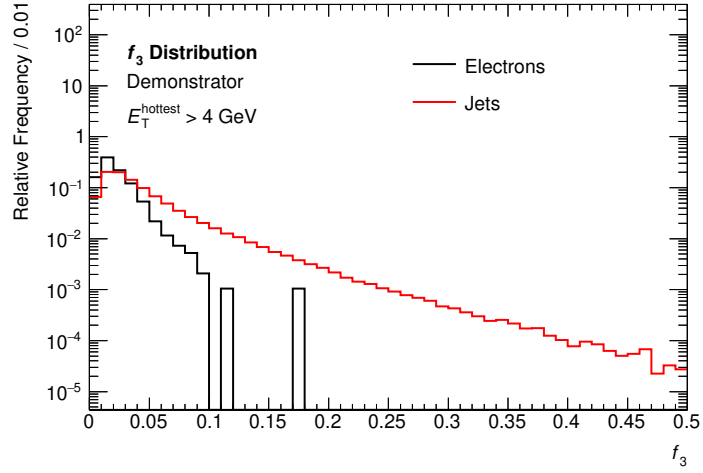


Figure 8.15.: Comparison of the f_3 distribution for electrons and jets for the LAr demonstrator.

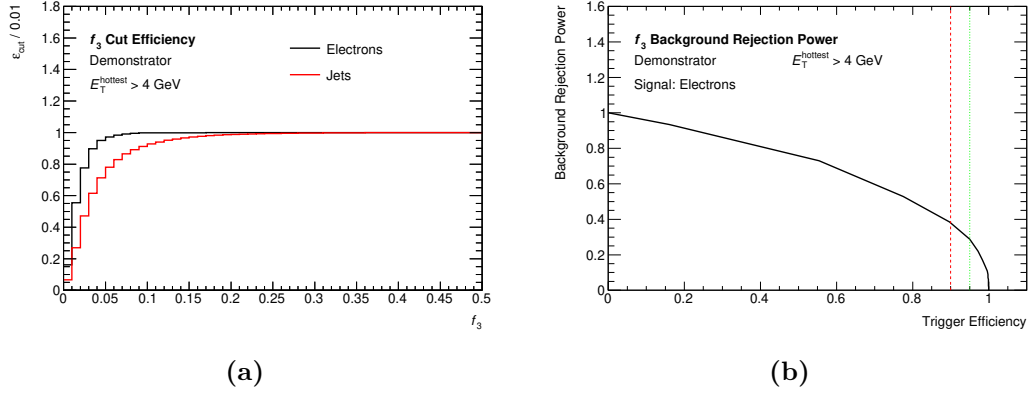


Figure 8.16.: Cut efficiencies for electrons and jets and the background rejection power. For the background rejection power on the right, 90 % (red) and 95 % (green) trigger efficiency are marked.

8.6. Studies of the Shower-Shape variable $w_{\eta,2}$

The last shower-shape variable to be studied is the shower width, $w_{\eta,2}$. The definition can be found in eq. (5.3). Electrons are expected to spread their energy across fewer supercells than jets.

Figure 8.17 shows the distributions of $w_{\eta,2}$ for electrons and jets for the LAr demonstrator and the main readout. Both the $w_{\eta,2}$ distribution of the electrons and the jets show good agreement for the LAr demonstrator and the main readout. This is because of the similar energy depositions in the 3×2 cluster, as has been shown in the R_η studies.

Next, the background rejection power of $w_{\eta,2}$ for the LAr demonstrator and the main readout is studied. The $w_{\eta,2}$ distributions for electrons and jets are displayed in fig. 8.18.

Because the energy spread of the electrons is on average smaller than for the jets, the two distributions are separated by a clear shift.

The cut efficiency for $w_{\eta,2}$ is carried out in the same manner as for f_3 . Also, the definition of the background rejection power is identical. Both the cut efficiencies for electrons and jets and the background rejection power are shown in fig. 8.19.

The similarities in the f_3 distributions are reflected in the cut efficiency curves. For electrons, the rise starts at a lower $w_{\eta,2}$ value than for the jets. The background rejection power is about 67% (57%) for a desired trigger efficiency of 90% (95%). With the $w_{\eta,2}$ distributions of the main readout⁴, a background rejection power of about 70% (67%) can be achieved.

⁴See appendix A.2

8. Studies of the Shower-Shape Variables

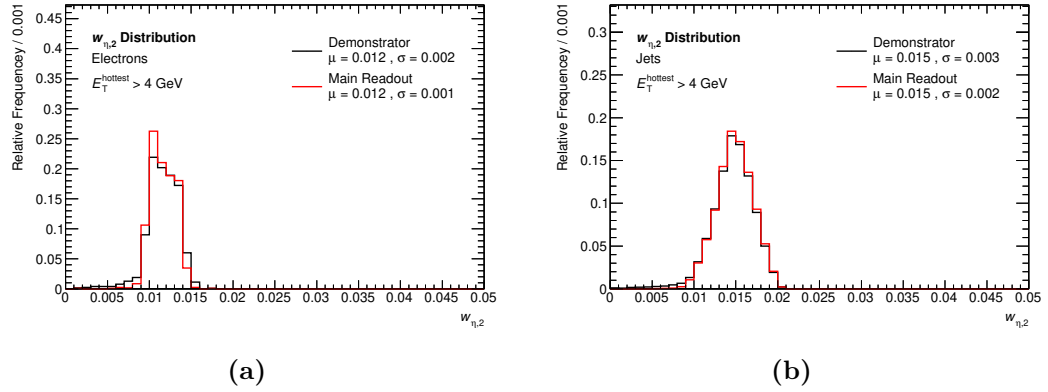


Figure 8.17.: Comparison of the $w_{\eta,2}$ distribution for electrons and jets between the LAr demonstrator and the main readout.

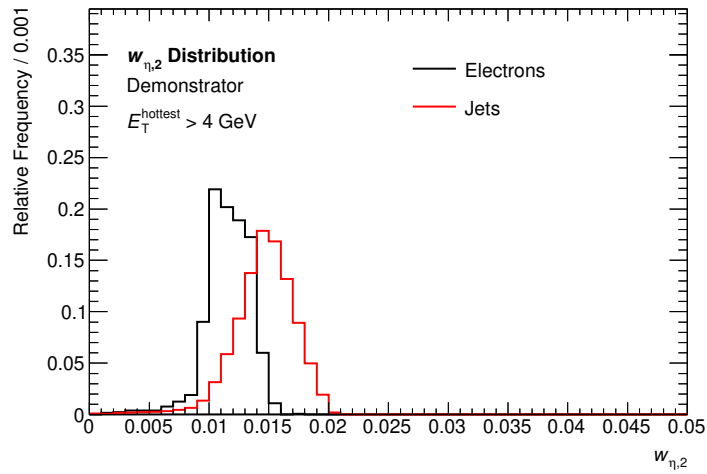


Figure 8.18.: Comparison of the $w_{\eta,2}$ distribution for electrons and jets for the LAr demonstrator.

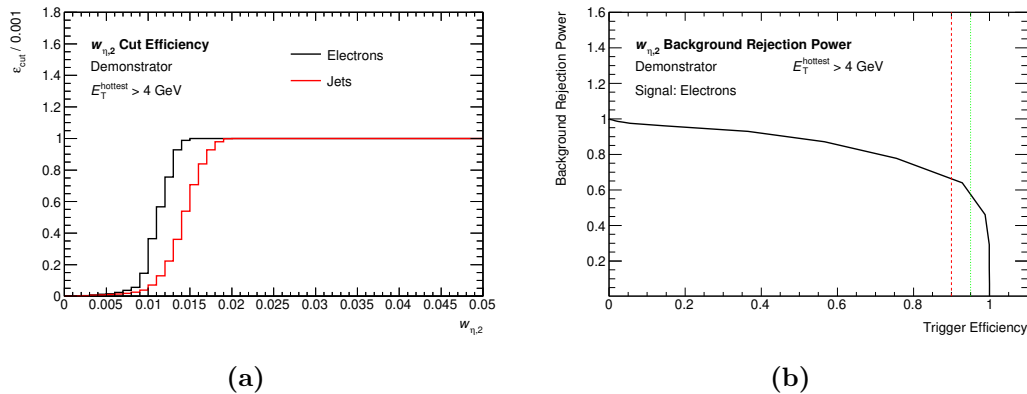


Figure 8.19.: Cut efficiencies for electrons and jets and the background rejection power. For the background rejection power on the right, 90 % (red) and 95 % (green) trigger efficiency are marked.

8.7. Trigger Efficiency Performance of the Shower-Shape Variables

In the following, the simulation studies performed in [113] are compared with results from this analysis. As a reminder of section 5.3.5, the simulation study suggests two sets of optimized cut parameters for the shower-shape variables.

- Set 95 (95 % ϵ_{cut}^e): $R_\eta \geq 0.93$, $f_3 \leq 0.02$, $w_{\eta,2} < 0.0146$
- Set 90 (90 % ϵ_{cut}^e): $R_\eta \geq 0.94$, $f_3 \leq 0.02$, $w_{\eta,2} < 0.014$

In addition, a 1 GeV cut on the HadCore⁵ variable is used in the simulation. This cut is neglected here, as no information from the Tile calorimeter is available. It is, however, important to note that a cut on the HadCore variable is very efficient. This has to be taken into account when comparing the results from this analysis to the simulation studies.

The proposed cuts are applied to the data of the LAr demonstrator and the main readout. The resulting trigger efficiency and the background rejection power are summarized in table 8.1.

While both the LAr demonstrator and the main readout show a good background rejection power, the trigger efficiencies are below expectations for the optimized cut

⁵The definition can be found in section 5.3.5.

Table 8.1.: Achieved trigger efficiency and background rejection power with the two sets of optimized cut parameters for the shower-shape variables.

	Achieved Trigger Efficiency	Achieved Background Rejection
<hr/> LAr Demonstrator <hr/>		
Set 95	38 %	96 %
Set 90	32 %	97 %
<hr/> Main Readout <hr/>		
Set 95	80 %	91 %
Set 90	71 %	94 %

parameters. What is striking is that not just the LAr demonstrator does not meet the expectations, but also the main readout. As the data from the main readout is expected to contain the most accurate energies, the results can be seen as an upper limit. Because of the missing cut on the HadCore variable, a direct comparison is not meaningful though.

To investigate the possible trigger efficiency further, a simple variation of the cut parameters is done. For R_η , the cut parameter is varied in the range of 0.75–0.95 in steps of 0.01. The cut parameter of f_3 is varied in the range of 0.01–0.1 in steps of 0.01, for $w_{\eta,2}$ in the range of 0.0135–0.015 in steps of 0.0001.

The results for the trigger efficiency and the background rejection power together with the corresponding cut parameters are summarized in table 8.2. Selected are the parameters with which at least 95 % (90 %) trigger efficiency are achieved. Because several sets of cut parameters fulfill these conditions, a grid search was performed to find the ones with the highest background rejection power. For the simulation studies in [113], the background rejection power was not given explicitly. Instead, the reduction of the trigger rate for different E_T thresholds was examined.

For the main readout, the outcomes of the cut parameters are close to the ones of the simulation. The results of the cut parameters for the LAr demonstrator are mixed: while the values for $w_{\eta,2}$ are almost identical to the simulation, R_η and f_3 show a clear difference.

Table 8.2.: Achieved trigger efficiency and background rejection power with the variation of the cut parameters for the shower-shape variables. In [113], the background rejection power was not given explicitly for the simulation studies.

Achieved	Achieved	Cut values on		
Trigger Efficiency	Background Rejection	R_η	f_3	$w_{\eta,2}$
LAr Demonstrator				
95 %	68 %	0.82	0.1	0.0144
90 %	75 %	0.82	0.08	0.0139
Main Readout				
95 %	81 %	0.89	0.03	0.0145
91 %	86 %	0.91	0.03	0.014
Cut Parameters from [113]				
Set 95		0.93	0.02	0.0146
Set 90		0.94	0.02	0.014

8.8. Conclusion

About 95 % of the LAr demonstrator events are successfully matched to main readout data. Roughly one-third of the events are good for the studies of the shower-shape variable.

The comparison between the shower-shape variables calculated for the LAr demonstrator and the main readout data show the impact of the main readout's higher precision for small energies. This has a direct effect on the shower-shape variables, especially when it comes to the energies in the outer part of the 7×2 cluster in the middle layer (used for the calculation of R_η) and the 2×2 cluster in the back layer (used for the calculation of f_3). The deviations lead to distributions of R_η and f_3 for the LAr demonstrator that are not as narrow as the ones for supercells calculated from the main readout.

These differences have an impact on the cut parameters. When compared with the optimized parameters from [113] for 95 % and 90 % trigger efficiency, only the values of $w_{\eta,2}$ match. While the values of R_η and f_3 differ just slightly for the main readout, the broader distributions of R_η and f_3 obtained by the LAr demonstrator and the

8. *Studies of the Shower-Shape Variables*

main readout lead to clear differences in these values. Adjusting the cut parameters leads to a lower background rejection power.

While the studies show the power of the shower-shape variables to reduce background, they also demonstrate the dependence on a precise energy reconstruction. Even small changes in the reconstructed energies have an impact on the distribution of R_η and f_3 . Therefore, it is important to study the cut parameters within the running system. If necessary, they have to be adjusted to get a sufficiently high trigger efficiency.

9. Pile-Up Analysis

With the future increase of the luminosity, the average number of pile-up events will rise. While the design luminosity of the LHC is $L = 10^{34} \text{ cm}^{-2} \text{ s}^{-1}$, a peak luminosity of $L = 2.1 \times 10^{34} \text{ cm}^{-2} \text{ s}^{-1}$ was reached in 2018 [145]. The average number of pile-up events during Run 2 was $\langle \mu \rangle = 33.7$, as shown in fig. 3.13.

Both the luminosity and the average number of pile-up events are expected to further increase after the future upgrades of the LHC. Following the Phase-I upgrade, a luminosity of $L = 2.2 \times 10^{34} \text{ cm}^{-2} \text{ s}^{-1}$ and a $\langle \mu \rangle = 60$ are expected [113]. For the HL-LHC, a luminosity of $L = 5\text{--}7.5 \times 10^{34} \text{ cm}^{-2} \text{ s}^{-1}$ and a $\langle \mu \rangle$ between 140 and 200 are expected [108].

As explained in section 6.2, pile-up effects pose a major challenge to the energy reconstruction. Since pile-up noise is part of the noise term of the energy resolution (see eq. (4.2)), it has a direct impact on it. It is expected in the HL-LHC era, that the noise term will dominate the energy resolution [108].

As stated in section 3.3, the interactions of interest have a high momentum transfer. But these hard interactions are often superimposed by pile-up events with low momentum transfer. Hence, a good understanding of pile-up effects is necessary to determine their impact on the measurement of hard interactions.

The data of the LAr demonstrator allow a study of the pile-up effects. In contrast to the main readout of the LAr calorimeter, which only reads out four samples around the peak of each pulse, the LAr demonstrator data contain 50 ADC samples. That means the complete pulse of an event is recorded. With the peak of the pulse being around the 22nd sample, it is possible to examine bunch crossings that are before and after the peak.

In section 9.1, the process of assigning the BCIDs to samples is described. In section 9.2, the energy distribution of the pile-up events is studied. The effect of pile-up on the baseline is examined in section 9.3. The development of the average pile-up energy over the course of a run is investigated in section 9.4.1. In section 9.4.2, the pile-up energy dependence on μ is analyzed.

9.1. BCID Assignment and Examined Range

For the following pile-up analyses, it is necessary to assign a BCID to each of the 50 ADC samples. This is done for each event in the same manner. First, the supercell with the highest energy deposition is identified. Next, the sample of the energy deposition, S_E , of this supercell is determined. If S_E is in a range of ± 5 around the usual S_{peak} of the supercell (see section 7.4), the event is valid for the pile-up analysis. Otherwise, it is discarded, to exclude events with a potential unstable S_{peak} . The event's BCID is then assigned to the sample S_E . This allows a determination of the BCID for each sample of this supercell and event. This takes into account that the peak of the bipolar pulse shapes is about 50 ns behind the peak of the detector pulse (see fig. 4.8).

To assign the correct BCID to the samples of the other supercells, it is necessary to calculate the shift, δ_{shift} , between S_E and S_{peak} . With δ_{shift} and the individual S_{peak} of each supercell, it is possible to assign each sample to a BCID.

As described in section 7.4, the process of the peak sample determination is error-prone. Hence, the assigned BCID should be regarded with caution.

The examined range of samples is the same for all pile-up analyses. It is adjusted individually for each supercell. Only samples before S_{peak} are investigated. To account for possible shifts of S_{peak} , this range is reduced by the 5 samples in front of S_{peak} .

9.2. Pile-Up Energy Spectrum

For the spectrum of the pile-up energy depositions in the examined range, only samples which are a local maximum are selected. Also, the bunch crossing of the sample has to be within a bunch train. The resulting energy spectra of the four detector layers for run 334 487 are shown in fig. 9.1. They are overlaid with the energy spectra of the triggered events for the same run for comparison.

Both the energy spectra of the pile-up and of the triggered events show an exponential decay in the low E_T part. For high E_T , the shape of the spectra changes to a power law [146, 147]. The maximum energy of the pile-up events is smaller than that of the triggered events. This is explained by the low momentum transfer in soft collisions.

Because μ , the average number of pp collisions, is not constant over a run, the energy spectra should be studied for different μ . Therefore, each event is assigned a μ value. The values are read from the ATLAS Run Queries database [148] and assigned

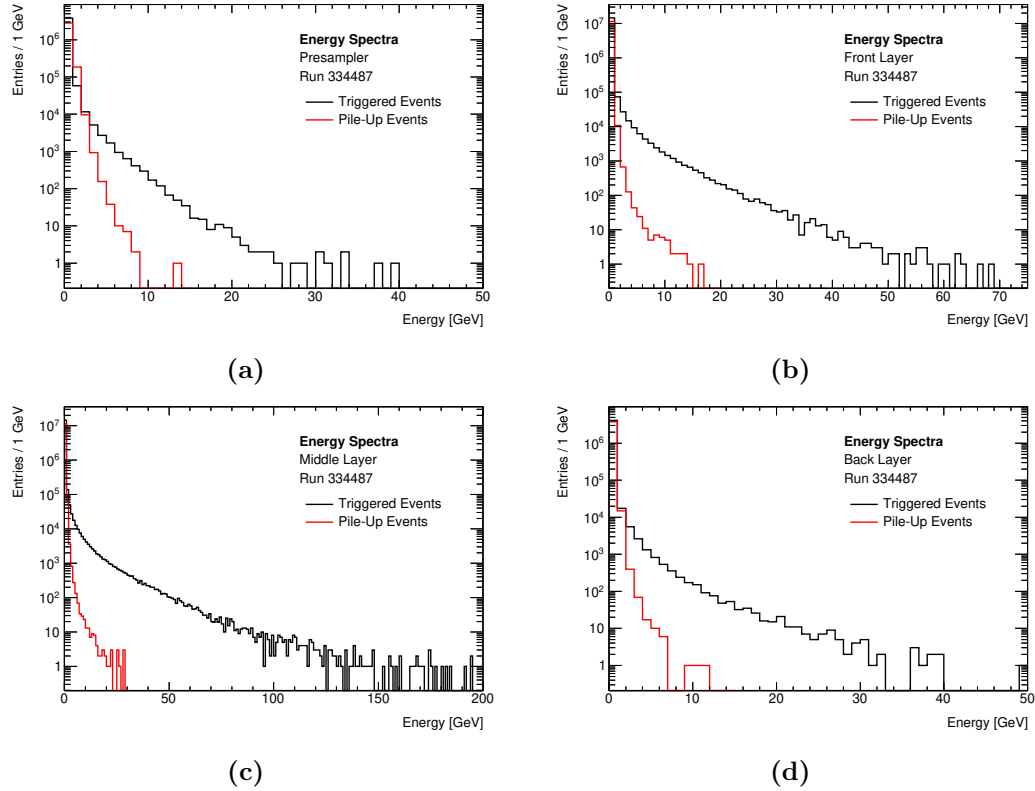


Figure 9.1.: The energy spectra of pile-up (red) and triggered events (black) in all four detector layers. The data are from run 334 487.

9. Pile-Up Analysis

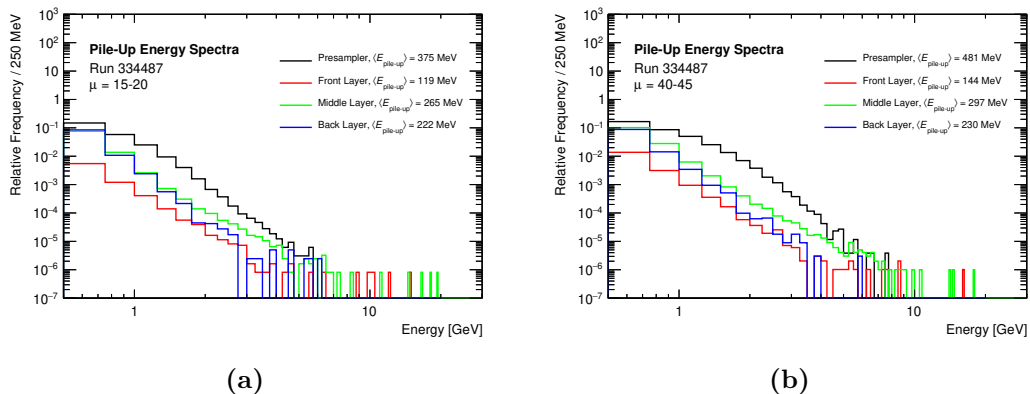


Figure 9.2.: The pile-up energy spectra of the four detector layers for different μ intervals. The data are from run 334 487.

Table 9.1.: Average pile-up energy of the four layers for different μ intervals.

μ range	15–20	20–25	25–30	30–35	35–40	40–45
Layer	Average pile-up energy in MeV					
Presampler	368	383	405	427	458	471
Front	116	119	125	130	138	141
Middle	275	279	286	293	302	305
Back	210	211	214	216	218	219

to intervals of width 5. The energy spectra for two different μ intervals are shown in fig. 9.2.

As the average pile-up energy depositions, $\langle E_{\text{pile-up}} \rangle$, for the four detector layers indicate, the energy spectra shift towards higher energies for higher μ . However, the maximum energies do not change significantly. Instead, the fraction of high-energy entries increases, as more particles deposit their energies in the supercells. On average, the highest pile-up energies are deposited in the presampler and the middle layer. $\langle E_{\text{pile-up}} \rangle$ for different μ intervals is summarized in table 9.1. While $\langle E_{\text{pile-up}} \rangle$ increases from $\mu = 15\text{--}20$ to $\mu = 40\text{--}45$ by over 100 MeV in the presampler, it is almost constant for all μ intervals in the back layer.

To compare the total values of $\langle E_{\text{pile-up}} \rangle$, it is important to take the size of the different supercells into account (see table 5.1). The supercells of the presampler and the back layer have the same size in $\eta \times \phi$. The supercells of the front and the

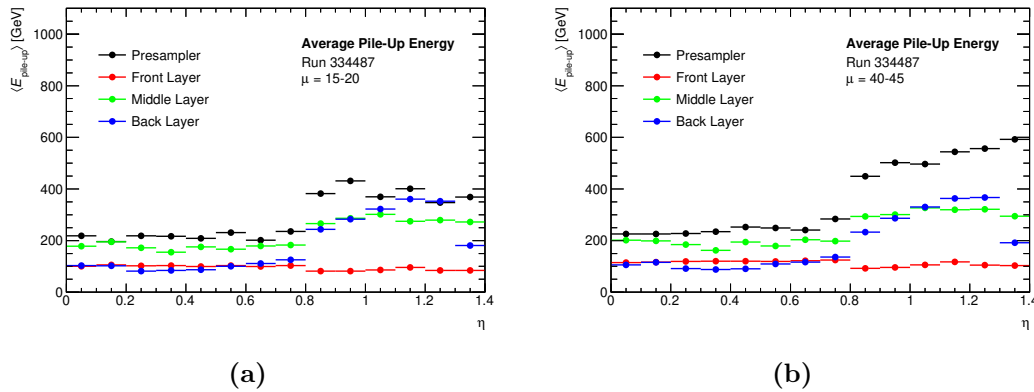


Figure 9.3.: The average pile-up energy of the four layers for different μ . In the front layer and the middle layer, four neighboring supercells are summed to partially account for different supercell sizes.

middle layer have a 4-times finer separation in η . Additionally, the middle layer is the largest in terms of radiation lengths (see fig. 4.5). Because a simple conversion of the different cell sizes is not possible, a direct comparison of the total values of $\langle E_{\text{pile-up}} \rangle$ is not meaningful.

Because of the larger size in terms of radiation lengths, the supercells in the middle layer have a higher $\langle E_{\text{pile-up}} \rangle$ than the supercells in the front layer. Though the supercells in the presampler and the back layer have the same size in $\eta \times \phi$, $\langle E_{\text{pile-up}} \rangle$ is higher in the presampler than in the back layer. The reason for this is, that the most low-energetic particles are stopped before they can reach the back layer.

Finally, the η -dependence of $\langle E_{\text{pile-up}} \rangle$ for different μ intervals is shown in fig. 9.3. To enhance comparability, in the front layer and the middle layer four neighboring supercells are summed up. For the supercells in the front layer, the middle layer, and the back layer no significant change in $\langle E_{\text{pile-up}} \rangle$ is apparent. In the presampler, however, $\langle E_{\text{pile-up}} \rangle$ increases noticeably for $\eta > 0.8$.

9.3. Pile-Up Baseline Shift

Because the BCID is known for every sample, it is possible to assign the energy of the sample to this BCID. The assigned energy is divided by the recorded average number of pp collisions, μ . This is done to account for the change of μ over time

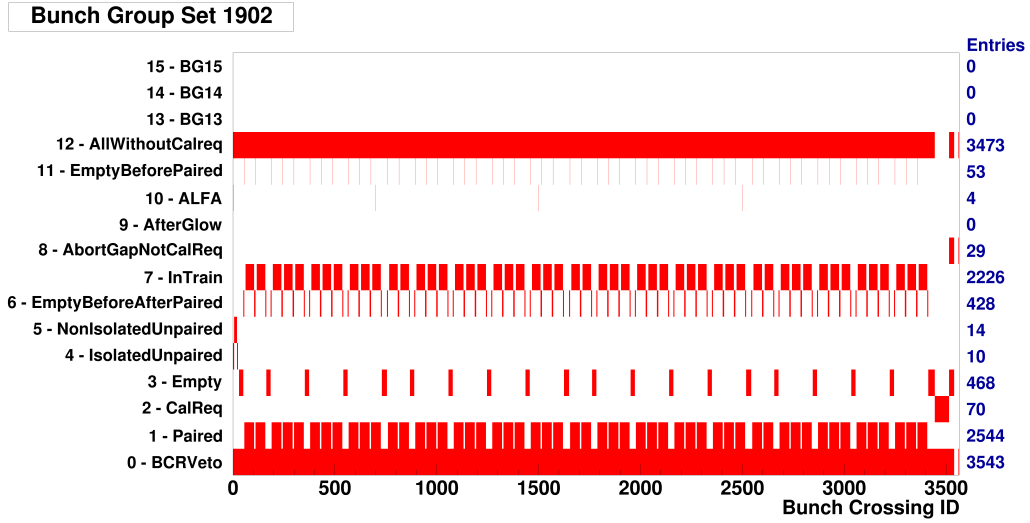


Figure 9.4.: Overview of the bunch structure of run 330470 [149]. The filled bunches are marked in red in the line *1-Paired*. The pattern starts with 56 empty bunches followed by the first block which consists of a 2-batch and three 3-batch sets. The 2-batch set has two bunch trains of 48 filled bunches, which are separated by a gap of 7 empty bunches. The 3-batch set consists of three bunch trains of 48 filled bunches with two gaps of 7 empty bunches each. The following three blocks consist of a 2-batch and four 3-batch sets. Between the blocks, 35 bunches are empty. The last 156 bunches are empty again.

(see section 9.4.2). After the analysis of a full run, the average pile-up energy for each BCID, $\langle E_{\text{pile-up}}/\mu \rangle$, is calculated.

As an example, run 330470 (recorded on 24 July 2017) is investigated. The filling scheme for this run differs from the 25 ns filling scheme as described in section 3.1. An overview of the bunch structure is shown in fig. 9.4.

In fig. 9.5, the average pile-up energy per bunch crossing is displayed for a sequence of 250 bunch crossings. The number of registered energy depositions differs for each BCID. To exclude BCIDs with only a few entries, a threshold of 5% of the maximum number of entries is set.

The effect of pile-up manifests itself in a shift of the baseline. It looks the same for all detector layers and reflects the expectations. The curve for the presampler is used as an example for the following discussion.

Before the first bunch train, the negative baseline shift caused by the last bunch

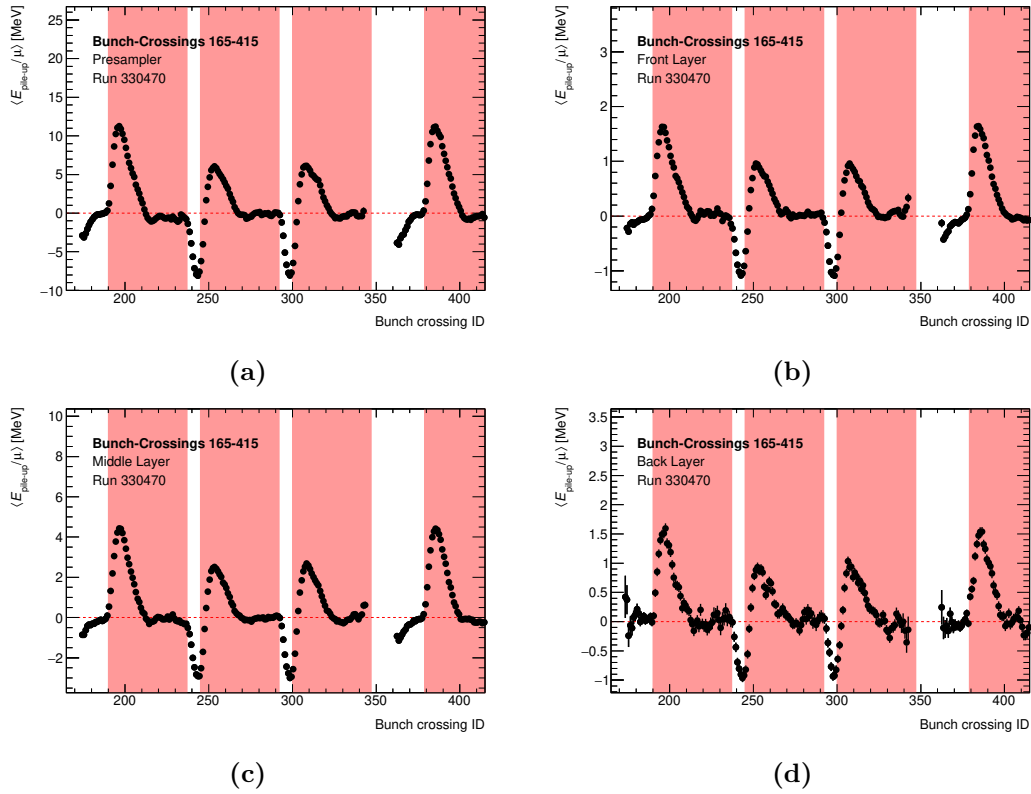


Figure 9.5.: Average energy deposition for a sequence of 250 bunch crossings. The energy of the supercells of the same layer is summed. To account for the change of μ over the course of a run, the energies are divided by the average number of pp collisions. The bunch trains are highlighted in red.

train – which is not shown in the plot – returns to the pedestal. This effect is also visible before the fourth bunch train. After the beginning of the first bunch train, the baseline rises until the undershoots of the pulses compensate for the shift (as described in section 6.2).

In the gap between the first and the second bunch train, a negative baseline shift is visible. Since the gap is not long enough for the baseline to return to its pedestal value, it distorts the positive baseline shift at the beginning of the second bunch train. For this reason, the baseline shift is not as pronounced as the first. The same applies to the gap between the second and the third bunch train.

At the end of the third bunch train, a negative baseline shift is expected. Yet, for the middle layer (and especially the front layer), the baseline seems to shift in the positive direction. To investigate this potential baseline shift further, the data of the four ϕ slices are displayed separately in fig. 9.6.

It shows, that the potential baseline shift is visible for $\phi = 2.01$ and $\phi = 2.11$. Also, the amplitude of the first positive baseline shift for $\phi = 2.01$ has half the value of the other ϕ slices. Therefore, the single supercells in the front layer at $\phi = 2.01$ are investigated. The data of the two most common patterns are shown in fig. 9.7.

The curve is much noisier due to lower statistics in these individual supercells. Figure 9.7a generally shows the expected baseline shift. Yet, at the end of the third bunch train, the unexpected positive baseline shift is visible. In fig. 9.7b, the bunch trains do not show this baseline shift. Though in some bunch crossing ranges, the samples shift in the same direction, for the majority of the entries, the values seem to be distributed randomly between -1 MeV and 1 MeV. Still, at the end of the third bunch train, the potential positive baseline shift is visible.

The cause for the potential positive baseline shift can not be determined ultimately. One hypothesis is that for the supercell with $i_\phi = 28$, S_{peak} is not determined by the peak sample identification. Instead, a default value is used for this supercell in this run. Further, the instability of the prototype electronics has to be taken into account. It has been observed that in some runs, S_{peak} of individual supercells was not stable.

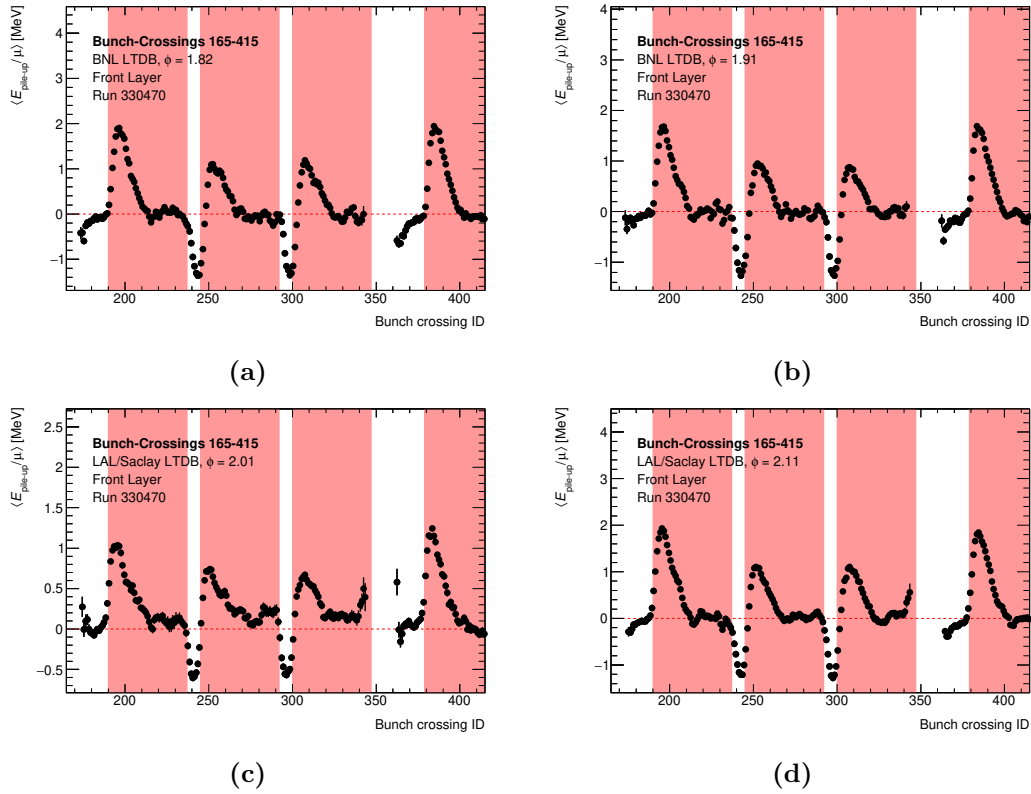


Figure 9.6.: Mean energy deposition for a sequence of 250 bunch crossings. The bunch trains are highlighted in red. To account for the change of μ over the course of a run, the energies are divided by the average number of pp collisions. The data of the supercells of the four ϕ slices are summed.

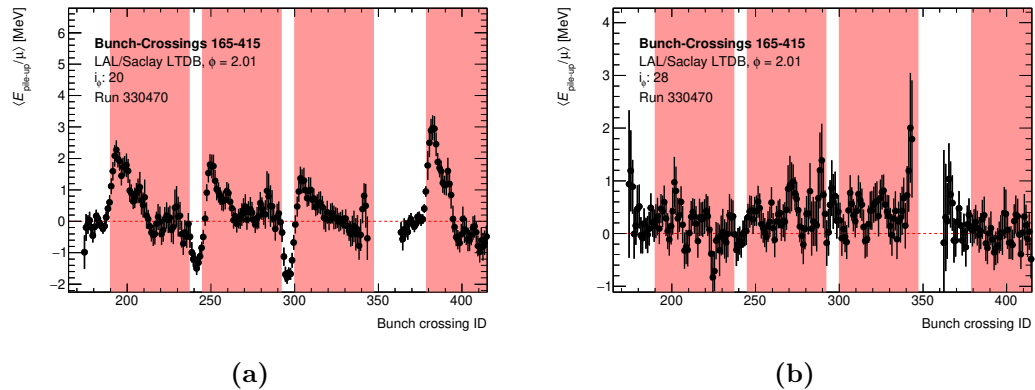


Figure 9.7.: Mean energy deposition for a sequence of 250 bunch crossings. The bunch trains are highlighted in red. To account for the change of μ over the course of a run, the energies are divided by the average number of pp collisions. The data are of the supercells with $i_\phi = 20$ on the left and $i_\phi = 28$ on the right.

9.4. Studies of the Bunch-Train Beginning

As seen in section 9.3, the positive baseline shift reaches a maximum at the beginning of a bunch train. The following studies examine the position of the maximum. To prevent the bunch crossing from being affected by a previous pulse, a gap of 25 empty bunch crossings is required ahead of the bunch train. All events that fulfill these conditions are used for the analyses.

9.4.1. Development of the Average Pile-Up Energy during a Run

The development of the average pile-up energy, $\langle E_{\text{pile-up}} \rangle$, of the bunch crossing with the highest positive baseline shift is studied over the course of run 333487 (recorded on 17 August 2017). Because every recorded event is marked with a timestamp, it is possible to assign each bunch crossing to a point in time during a run. The duration of the run is divided into time slices of 30 min. For each time slice, $\langle E_{\text{pile-up}} \rangle$ is calculated. The development of $\langle E_{\text{pile-up}} \rangle$ in the four detector layers is shown in fig. 9.8. It is overlaid with the development of μ during that run, taken from the ATLAS Run Queries database [148].

At the beginning of a run, the LHC is filled with bunches of approximately 1.15×10^{11} protons. Due to collisions, this number decreases with each bunch crossing.

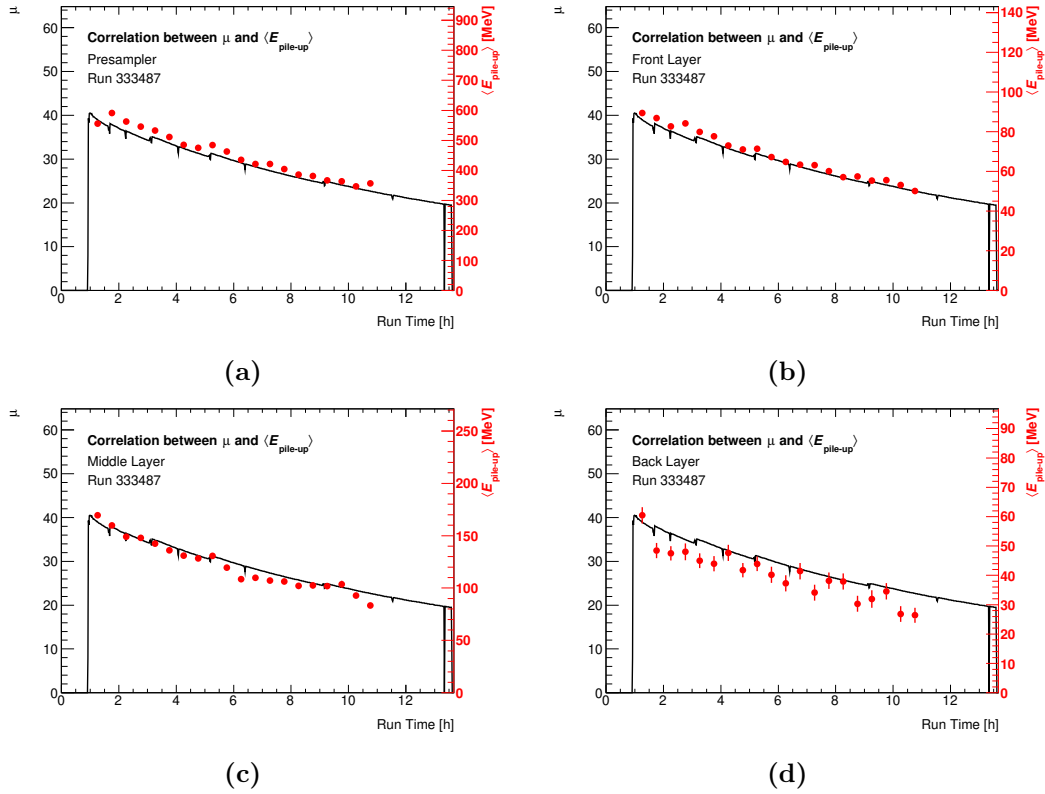


Figure 9.8.: Development of the average pile-up energy in the sample with the maximum of the positive baseline shift in each bunch train (red) over the course of run 333487. It is overlaid with the development of μ (black) for this run. The average over time slices of 30 min is taken.

Hence, over the course of a run, the luminosity decreases and with it the average number of pp collision, μ . The curves shown in fig. 9.8 support this assumption.

9.4.2. Correlation between Pile-Up Energy and μ

This study uses data from run 338 183 (recorded on 13 October 2017).

In addition to the requirements on the gap in front of the bunch train (see section 9.4), only supercells in a region with $\eta < 0.8$ are considered in this study. This ensures that for each detector layer, the $\langle E_{\text{pile-up}} \rangle$ of all examined supercells is similar (see fig. 9.3). If a sample meets these criteria, it is recorded together with the corresponding μ value. For the analysis, the μ values are assigned to intervals of width 5. After examining a full run, $\langle E_{\text{pile-up}} \rangle$ is calculated for each μ range. The correlation between energy and μ is shown in fig. 9.9 for each detector layer.

In general, all four detector layers show a correlation between $\langle E_{\text{pile-up}} \rangle$ and μ . The observations of $\langle E_{\text{pile-up}} \rangle$ in section 9.3 for the different detector layers also apply for this study. When μ changes from 20–25 to 55–60, $\langle E_{\text{pile-up}} \rangle$ increases by a factor of 2.

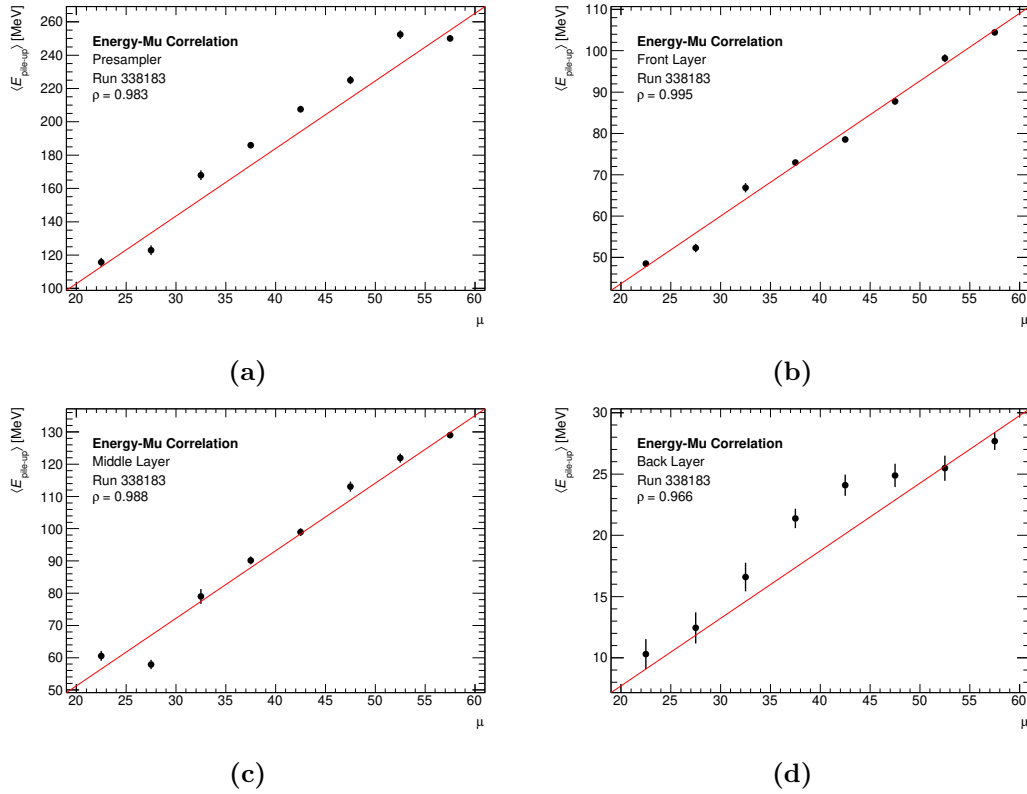


Figure 9.9.: The correlation, ρ , between the average pile-up energy of the maximum of the positive baseline shift and μ . All four detector layers show a good correlation. The data are from run 338 183. For a visual reference, the diagonal is marked in red.

9.5. Conclusion

In the data of the LAr demonstrator, the effects of pile-up are observable.

The average pile-up energy correlates with the average number of pp collisions. While this effect has only a minor impact in the back layer, the presampler is greatly affected by it. The reason is that low energy particles do not reach the back layer and lose all their energy in the inner layers. Furthermore, supercells that are in the more forward region with $|\eta| > 0.8$ are exposed to higher average pile-up energy.

The additional energy deposition poses a major challenge to the L1 trigger. Especially the baseline shift at the beginning of a bunch train can lead to fake triggers, which occupy the limited trigger rate. Although an increase of the p_T threshold could account for this, events of interest would be suppressed too. Hence, it is necessary to study pile-up mitigation techniques. An example is the preprocessor of the L1Calo trigger, which was equipped with new multi-chip modules during Long Shutdown 1. These modules allow a dynamic, bunch-by-bunch pedestal correction [150].

The new trigger readout electronics will implement a pedestal correction. Because the average pile-up energy depends on the location of the supercell, it is necessary to calculate the correction for each supercell individually.

10. Wiener Filter Studies

In this chapter, the Wiener filter is examined as an alternative to the Optimal Filter for energy reconstruction in the trigger readout of the LAr calorimeter. The focus is on the signal detection efficiency for different phase shifts of the pulse shape. In section 10.1, the pulse shapes that are used for the calculation of the filter coefficients are introduced. In section 10.2, the WF_{FC} and its ability to correct the undershoot are studied. In section 10.3, two configurations of the Wiener filter are investigated.

10.1. Pulse Shape Comparison

As described in section 6.5, the pulse shape of the signal has to be known to calculate the filter coefficients of the Wiener filter. The same applies to the Optimal Filter (see section 6.4). The physics pulse shapes used here are predicted from the calibration pulse shapes with the Response Transformation Method [151]. To compare the predicted pulse shapes and the measured pulse shapes of recorded events, events with $E_{\text{main}} > 5$ GeV from run 334 487 are examined.

First, the phase shift, t_{shift} , between the two kinds of pulse shapes is determined. For that, the predicted pulse shape is sampled multiple times at 40 MHz. Each time, it is shifted by 500 ps. The objective is to find the time shift, $t_{\text{shift}}^{\text{min}}$, where the sum of the squared residuals is minimal. Only the six samples around the peak are taken into account, as they are used by the filter algorithms to reconstruct the energy. The sum is defined as:

$$\sum_{i=0}^5 (S_i^{\text{meas}} - S_i^{\text{cal}}(t_{\text{shift}}))^2 \quad (10.1)$$

where S_i^{meas} are the measured samples, and $S_i^{\text{cal}}(t_{\text{shift}})$ are the samples of the predicted pulse shape for a given t_{shift} .

In the next step, the difference between the S_i^{meas} and $S_i^{\text{cal}}(t_{\text{shift}}^{\text{min}})$ for each of the 25 samples of the pulse shape is recorded. With the recorded values, the average difference between the measured detector pulse shape and the predicted pulse shape

10. Wiener Filter Studies

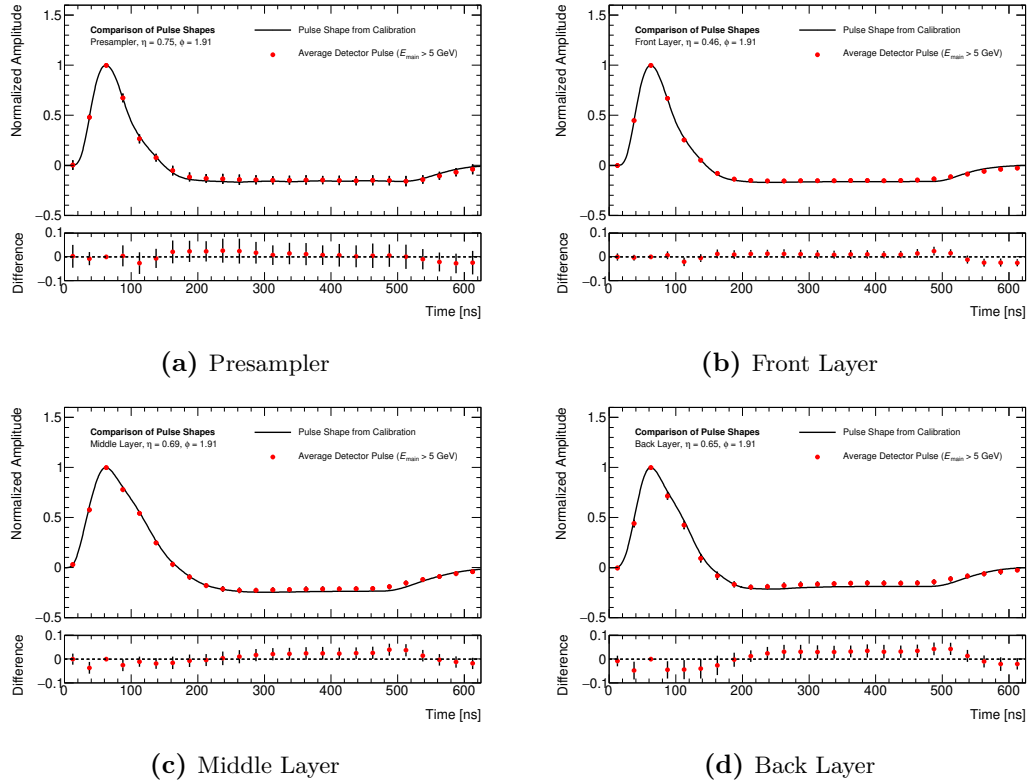


Figure 10.1.: Comparison between the average detector pulse shape and the pulse shape predicted from the calibration pulse. The data are taken from run 334 487.

for each sample is determined. The average measured pulse shape is obtained by applying the difference to each sample of the predicted pulse shape.

In fig. 10.1, a comparison between the average detector pulse shape and the pulse shape predicted from the calibration pulse is shown. 153 measured pulse shapes are examined for the presampler, 243 for the front layer, 628 for the middle layer, and 123 for the back layer. Especial the front layer shows good agreement of the samples around the peak between measured pulse and calibration.

10.2. Studies on the Wiener Filter with Forward Correction

The filter coefficients for the study of the performance of the WF_{FC} are determined with AREUS¹ [125, 127]. For the calculation, the predicted pulse shapes from calibration described in section 10.1 are used since they agree well with the measured data. The filter depth is $M_{WF} = 6$. For the FIR filter that corrects the falling edge of the undershoot, the filter depth is $M_{fall} = 4$, and for the FIR filter that corrects the rising edge of the undershoot, it is $M_{rise} = 3$. The margin on the peak to post-peak sample ratio is $m = 0.15$. In fig. 10.2, the operating principle as described in section 6.6 is shown in separate figures.

The WF_{FC} seeks to correct the undershoot of the bipolar pulse shape. This improves the energy resolution in subsequent samples. In fig. 10.3, an example of such a situation is shown. In sample 20 of the ADC output, an energy deposition with about 13 GeV is visible. This is followed by a second energy deposition in sample 32. The pulse shape of the second energy deposition is biased by the undershoot of the first energy deposition. While both filters correctly estimate the energy of the first energy deposition, the Optimal Filter underestimates the second hit and sends an energy value of about 2 GeV to the L1Calo trigger. Due to the forward correction, the WF_{FC} correctly estimates the second hit energy value of about 7 GeV.

As discussed in [125], the energy resolution of the WF_{FC} is highly dependent on the phase of the incoming pulses. Since the phase of the recorded pulses can no longer be shifted, the WF_{FC} is instead trained on shifted pulse shapes. To investigate the phase shift behavior of the WF_{FC} , 25 sets of filter coefficients for pulse shapes shifted in steps of 1 ns in a range of 0–24 ns are calculated and applied to the recorded events. In the following, the focus is on a supercell in the front layer with $\eta = 0.46$ and $\phi = 1.91$, as the measured pulse shapes for the front layer show the best agreement with the predicted pulse shapes from calibration.

As an example, the response with coefficients for a phase shift of 9 ns and 14 ns are compared in fig. 10.4. With the set of filter coefficients for a phase shift of 9 ns, the peak is detected. The set of filter coefficients for a pulse shape that is shifted by 14 ns does not detect the peak. The reason is, that the ratio between the peak and the post-peak sample changes when the pulse shape is shifted. Consequently, the WF_{FC} does not deliver the desired output anymore. In this case, the peak sample gets

¹AREUS stands for *ATLAS Readout Electronics Upgrade Simulation*. As the name states, it is a software framework to simulate the future readout electronics of the LAr calorimeter of the ATLAS detector.

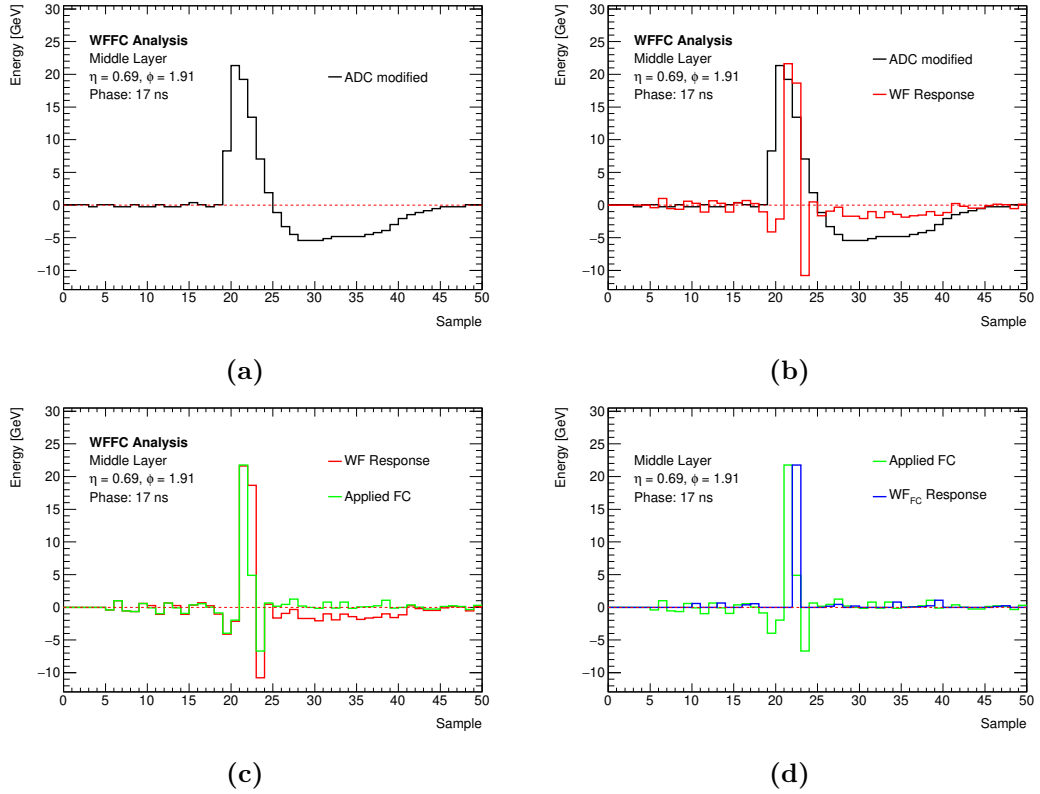


Figure 10.2.: Illustration of the operating principle of the WF_{FC} . The starting point builds the ADC samples drawn in fig. (a). In fig. (b), the response of the Wiener filter (red) to the ADC samples is displayed. The subsequent peak detection recognizes a peak in sample 22 followed by a post-peak in sample 23. In fig. (c), the response of the Wiener filter with the applied forward correction is drawn in green. The energy value of the peak (blue) is sent to the L1Calo trigger as shown in fig. (d). The data are taken from run 334 487.

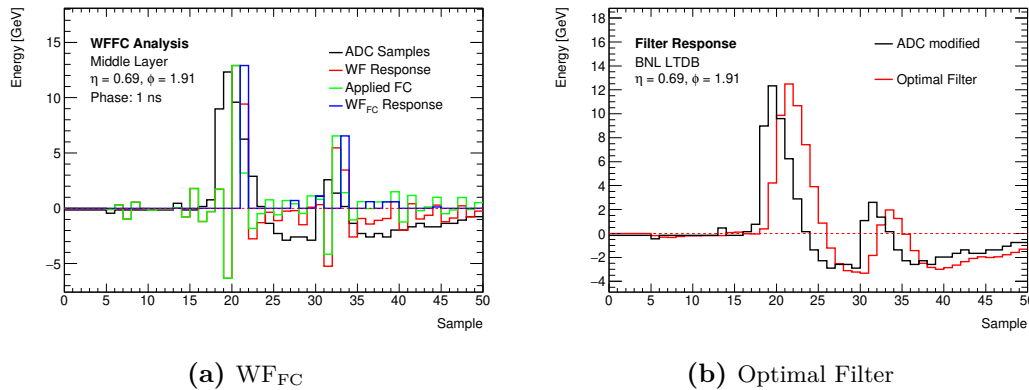


Figure 10.3.: Filter response of the WF_{FC} and the Optimal Filter to an energy deposition in the undershoot. While both filters correctly estimate the first energy value, only the WF_{FC} would send a correct estimation of the second hit to the L1Calo trigger. The data are taken from run 338 183.

overestimated and the post-peak sample underestimated. With about 2 GeV, it does not meet the requirement that the ratio between the peak sample and the post-peak sample has to be at least 0.35. The peak sample has a value of about 7 GeV, which requires the post-peak sample to be at least 2.45 GeV.

To classify this, the signal detection efficiencies of the 25 sets of filter coefficients for the WF_{FC} are compared to eight sets of filter coefficients for the Optimal Filter. For the Optimal Filter, the pulse shape is shifted in steps of 3 ns in a range of 0–21 ns. The filter coefficients of the Optimal Filter are derived with the ATHENA framework [142].

For this study, only events with $E_{\text{main}} > 5$ GeV, where E_{main} is the energy estimated by the main readout, are investigated. This is the case for 254 events in run 334 487 for the supercell in the front layer. A signal is considered as being detected, if:

$$\left| \frac{E_{\text{reco}} - E_{\text{main}}}{E_{\text{main}}} \right| < 0.1 \quad (10.2)$$

where E_{reco} is the energy estimated by the corresponding filter. In fig. 10.5, the signal detection efficiency of the WF_{FC} and the Optimal Filter are compared. For most of the Optimal Filter coefficients, the phase shift does not influence the outcome. With seven of the eight sets, a high signal detection efficiency of above 90% is achieved. This is different in the case of the WF_{FC} . Only for two phase shifts, namely 9 ns and 10 ns, the signal detection is above 90%.

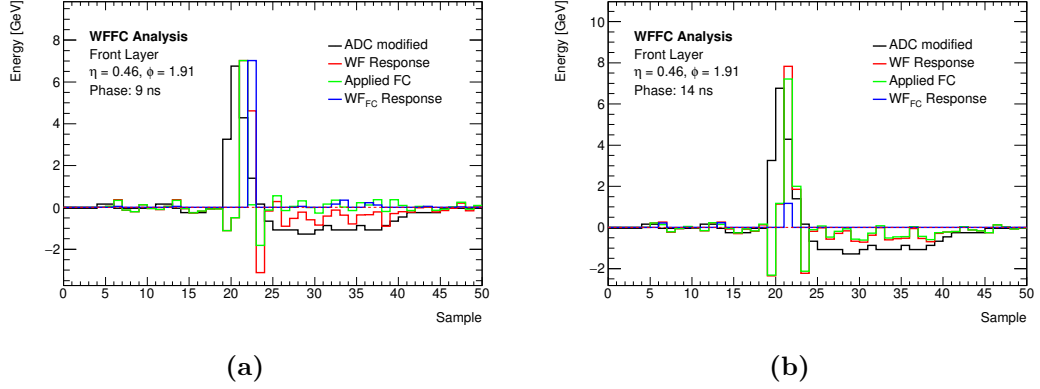


Figure 10.4.: WF_{FC} response to an energy deposition with two sets of filter coefficients for different phase shifts of the pulse shape. The data are taken from run 334 487.

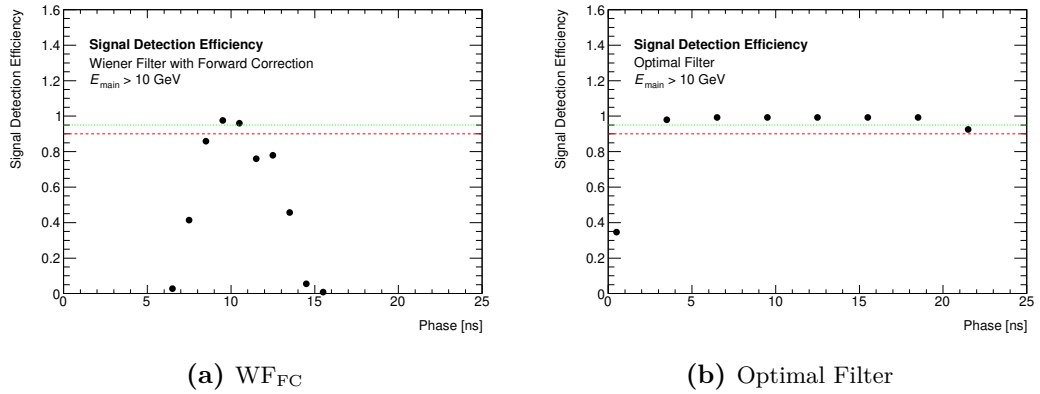


Figure 10.5.: Comparison of the signal detection efficiency of the WF_{FC} and the Optimal Filter with filter coefficients for different phase shifts of the pulse shape. The data are taken from run 334 487.

10.3. Studies on the Wiener Filter

The filter coefficients for the study of the performance of the Wiener filter are determined with AREUS. For the calculation, the predicted pulse shapes from calibration described in section 10.1 are used. The filter depth is $M_{WF} = 6$. The Wiener filter is studied using two different desired output signals during the calculation of the filter coefficients.

The first one has as desired output signal a peak with no pre-peak or post-peak sample. In fig. 10.6, the response with sets of filter coefficients for a phase shift of 10 ns and 24 ns are compared. For the coefficients for a phase shift of 10 ns, the desired output signal is apparent. The energy of the peak is slightly overestimated. Also, the samples before and after the peak show large oscillations in the positive and negative direction. The coefficients for a phase shift of 24 ns show instead of the desired output signal a signal with two peaks that have almost the same height. The explanation for this behavior is similar to the WF_{FC} studies in section 10.2. Due to the shift in the ratios of the different samples, the Wiener filter does not deliver the desired output signal anymore.

For the signal efficiency, the same conditions as used for the WF_{FC} are applied. In fig. 10.7, the signal detection efficiency of the Wiener filter is shown. Only for two phase shifts, namely 8 ns and 14 ns, the signal detection is above 90 %.

The second investigated Wiener filter has as desired output signal a peak with a pre-peak and a post-peak sample. Due to this, the deflections before and after the peak are flattened out. In fig. 10.8, the response with sets of filter coefficients for a phase shift of 9 ns and 20 ns are compared. For the coefficients for a phase shift of 9 ns, the desired output signal is apparent. At the same time, the estimated energy is much closer to the expected result. The coefficients for a phase shift of 20 ns shows instead of the desired output signal a signal with two peaks that have almost the same height. Also, the location of the maximum of the Wiener filter response has changed from being two samples after the peak to three samples after the peak. This has an impact on the bunch crossing identification².

For the signal efficiency, the same conditions as used for the WF_{FC} are applied. In fig. 10.9, the signal detection efficiency of the Wiener filter is shown. Over the range of a phase shift of 2–16 ns, the Wiener filter shows a signal detection with over 90 %.

²Besides the energy estimation, the correct bunch crossing identification is the second major task of the trigger system. This topic is not covered in this thesis, however.

10. Wiener Filter Studies

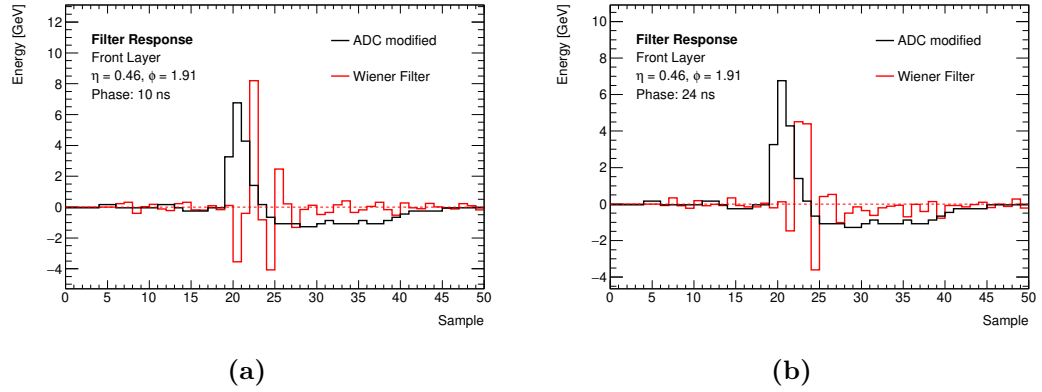


Figure 10.6.: Filter response of the Wiener filter to an energy deposition for two different phases. The data are taken from run 334487.

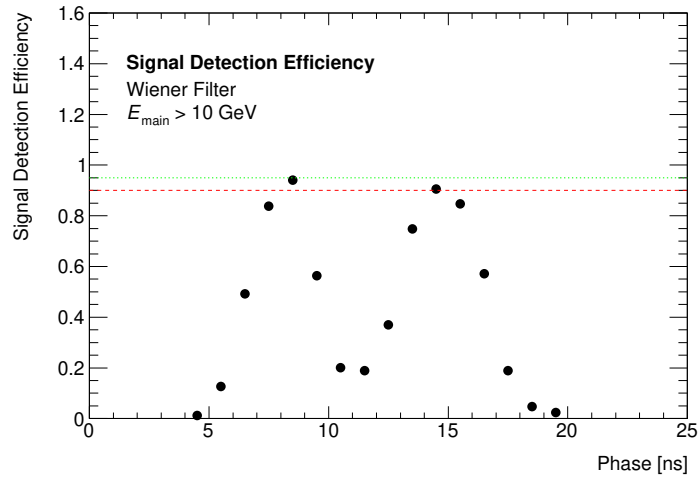


Figure 10.7.: Signal detection efficiency of the Wiener filter with filter coefficients for different phase shifts of the pulse shape. The data are taken from run 334487.

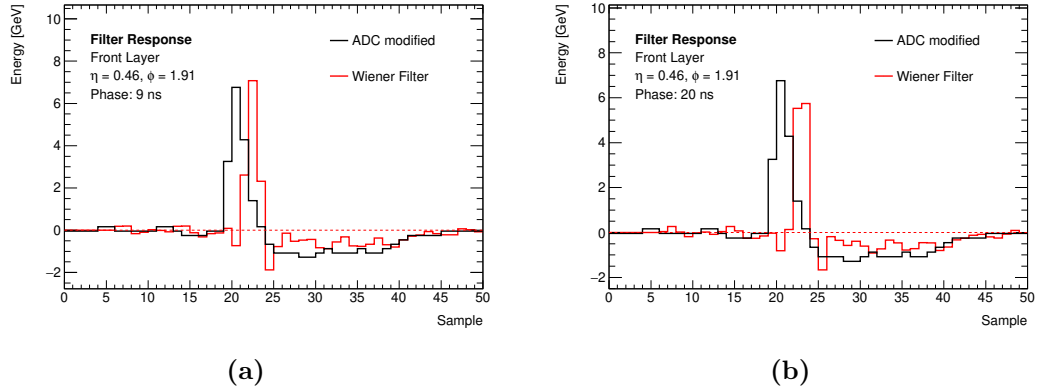


Figure 10.8.: Filter response of the Wiener filter to an energy deposition for two different phases. The data are taken from run 334 487.

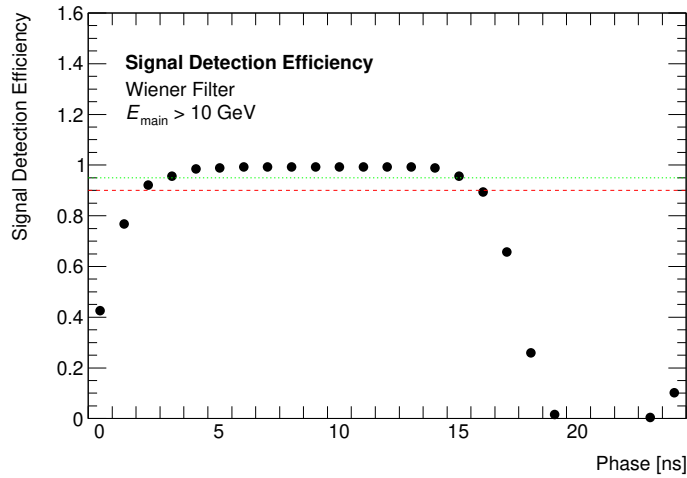


Figure 10.9.: Signal detection efficiency of the Wiener filter with filter coefficients for different phase shifts of the pulse shape. The data are taken from run 334 487.

10.4. Conclusion

The studies show that the WF_{FC} has both advantages and disadvantages. The WF_{FC} is capable to remove the bias from the undershoot of the bipolar pulse shape. Therefore, it is possible to detect two consecutive signals which are separated by less than the length of the pulse shape. On the other hand, the WF_{FC} relies on a stable shift of the pulse shape to deliver a high signal detection efficiency. If the pulse shape is shifted by more than a nanosecond, the energy is not estimated correctly. In the worst case, if the ratio between the energy of the peak and the post-peak sample does not match the required threshold, the signal is not detected at all.

As the WF_{FC} , the Wiener filter performance depends strongly on the pulse shape phase. Due to the varying ratios between the samples of the signal, the Wiener filter cannot deliver the expected output signal. This has an impact on signal detection efficiency. For the configuration of the Wiener filter with a narrow response, the results show, that as soon as the phase is shifted by a nanosecond the signal detection efficiency drops significantly.

The Wiener filter with a pre-peak and a post-peak sample shows better results. For a wide range of phase shifts, the signal detection efficiency is comparable with the Optimal Filter.

The bunch crossing identification has not been taken into account. This is equally as important for the trigger readout as the precise estimation of the energy deposited in the LAr calorimeter. If the wrong bunch crossing is identified, the data acquisition system does not record the correct samples for the offline reconstruction. Hence, the event is not usable for physics analyses.

The studies of the Wiener filter show that a shift of the pulse shape may lead to a different output of the filter algorithms, with the maximum being in a different sample than expected.

Overall, the Optimal Filter which is already used in the trigger readout seems to be the most applicable. Nevertheless, the Wiener filter with pre-peak and post-peak sample shows similar results in terms of signal detection efficiency. Both the WF_{FC} and the Wiener filter with neither a pre-peak nor a post-peak sample depend on a stable pulse phase. With a stable phase, however, the WF_{FC} could be a good candidate for higher luminosities as expected in the era of the HL-LHC. Because with a higher luminosity, consecutive energy depositions in a single supercell are more likely. This, however, needs further investigations that may be carried out during the upcoming LHC Run 3 2021–2024.

11. Conclusion and Outlook

The LHC and the ATLAS experiment can look back at a very successful history. To maintain this status, both follow an ambitious upgrade schedule. An increase in the luminosity delivered by the LHC is necessary to achieve precise measurements of Standard Model parameters and at the same time search for physics beyond the Standard Model.

Run 3 already foresees an increase in luminosity and center-of-mass energy of the particle collisions. On the one hand, this brings new opportunities for the ATLAS detector, on the other hand, it is also associated with new challenges. The increase in luminosity leads to an increase in signal and background events. Due to the technical limits on the L1 trigger rate, it is not possible to record all events. While a raised trigger threshold for keeping the trigger rate low would be an easy fix, this would also affect the acceptance of signals that contain physics of interest. To overcome this issue, an upgrade of the readout electronics of the LAr calorimeter is planned.

The new trigger electronics will allow a precise estimate of the energy deposition. At the same time, the elementary cells of the LAr calorimeter are summed up with higher granularity. The newly introduced supercells enable the use of more sophisticated shower-shape variables at trigger level. Data taken with a prototype of the future trigger readout electronics of the LAr calorimeter allows an investigation of these variables. Data that are processed by the ATLAS reconstruction software serve as a reference. Cuts on the single shower-shape variables R_η , f_3 , and $w_{\eta,2}$ allow distinguishing between signal and background. The combination leads to a background rejection power of 75 % (68 %) while keeping the trigger efficiency for electrons at 90 % (95 %). Possible extensions to these studies could calculate the trigger rate reduction for the data taken in an experimental environment. An integration of the information of the Tile calorimeter to calculate e.g. the HadCore variable would allow a comparison of the trigger rate reduction to predictions from simulations. This was not possible with the dataset available from the demonstrator setup.

The increased luminosity will lead to pile-up effects, which will challenge the filter algorithms that are used for the energy estimation in the trigger readout. In the data

taken with the prototype, a visible baseline shift at the beginning of a bunch train is apparent. The average energy deposited by pile-up events correlates with the average number of pp collisions. Therefore, a pedestal correction is crucial to be implemented in the new trigger readout electronics. Since the pile-up effects are dependent on the location of the cell, both in η direction and the detector layer, it is necessary to correct each supercell individually.

At the same time, it is important to have filter algorithms for the estimation of the energy deposited in the supercells that have a high signal detection efficiency.

The Wiener filter could be an alternative to the Optimal Filter that is currently used in the main readout. Different configurations of the Wiener filter show mixed results when it comes to signal detection efficiency. While a Wiener filter with a pre-peak and a post-peak sample is comparable to an Optimal Filter, the WF_{FC} with only a post-peak sample and a Wiener filter with neither a pre-peak nor a post-peak sample depend greatly on the correct phase of the pulse shape. Hence, they are not feasible for effective signal detection. Nevertheless, the WF_{FC} with its correction of the undershoot could be a suitable option for the era of the HL-LHC, where closely spaced events in a single cell are more likely to appear. A more robust implementation of the WF_{FC} with a pre-peak and post-peak sample is object to future studies.

Because the correct estimation of low energies is important for the precise calculation of the shower-shape variables, especially f_3 and R_η , further studies should focus on the signal detection efficiency for the low energy range. Also, studies on different filter algorithms addressing the correct identification of the bunch crossing are necessary. It is crucial to record the correct data with the bunch crossing at which the event took place.

While the results from simulations are a good measure for the ability of the new trigger electronics, it is important to validate them with data taken with real hardware in an experimental environment. This way, an effective and reliable data taking can be ensured.

With the precision measurement of the Standard Model parameters and the search for signatures of new physics, the ATLAS detector follows a challenging physics program. The results obtained in this thesis will help to ensure an efficient and robust energy reconstruction in the LAr calorimeter trigger readout, which is the basis for foreseen physics measurements.

A. Appendix

A.1. Calibration Runs

The ATLAS detector can be operated either in calibration or in physics mode. During calibration mode, the calibration boards of the LAr calorimeter readout electronics are used to inject signals in readout channels. In the following, a short overview of the calibration process is given. For more details refer to [152].

There are three different types of calibration runs. During a pedestal run, no signals are injected. These runs are used to determine a pedestal value¹ for each channel. Also, the noise level can be monitored and the autocorrelation matrix of the electronics noise can be obtained. The matrix is used for the calculation of the filter coefficients (see chapter 6). In fig. A.1, the pedestal values of the supercells are shown.

During a delay run, each readout channel is pulsed 200 times with signals with given input current. The time delay between the calibration pulse and the sampling clock is shifted in steps of about 1 ns. From the outputs, precise pulse shapes can be obtained. Since the signals of the calibration board differ from the physics signals, the physics pulse shapes have to be predicted from the obtained pulse shapes. The physics pulse shapes are then used for the calculation of the filter coefficients (see chapter 6).

During a ramp run, each readout channel is pulsed various times depending on the detector and the gain. Thereby, the input currents (DAC² values) are varied. From ADC values of the amplitude of the resulting pulses and the DAC values, the gain of the readout channel can be obtained.

The process of the computation of the ADC to MeV conversion factors which are displayed in fig. A.2 is explained in detail in [152]. For the computation, a factor from the prediction of the physics pulse shapes, thus from the delay runs, and the gain obtained in the ramp runs are used.

Figure A.3 shows the high-voltage correction factors which are calculated from

¹The ADC value without any input signal.

²Digital-to-Analog Converter

A. Appendix

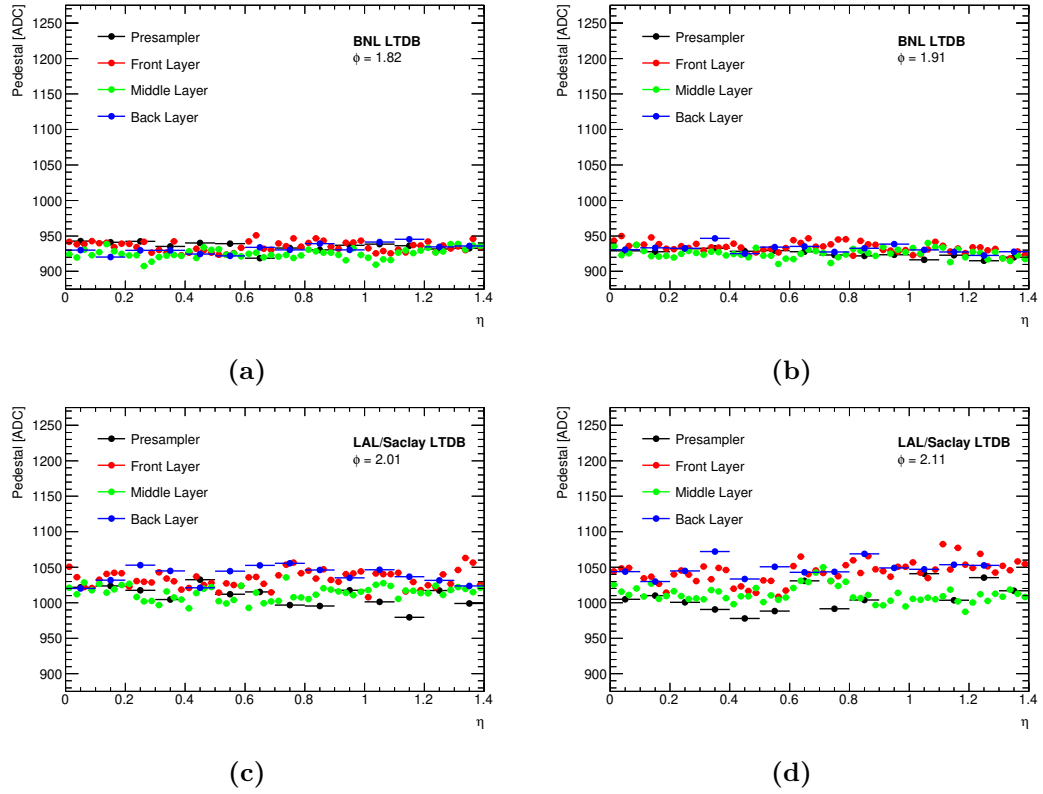
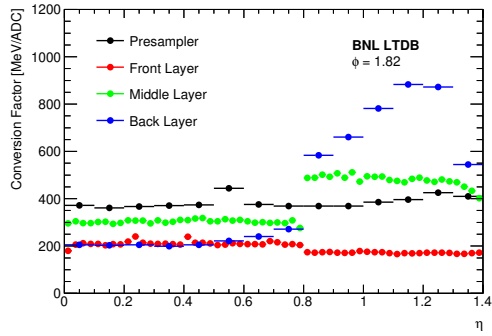
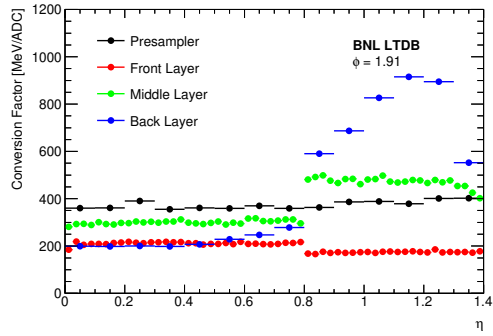


Figure A.1.: The measured pedestal values for the four LTDBs.

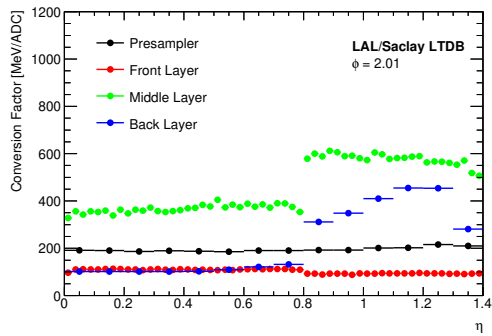
the official ATLAS database. All constants are derived using the ATHENA framework [142].



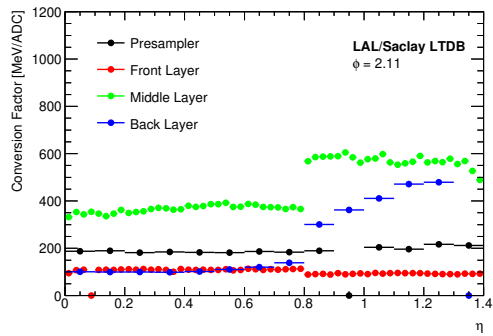
(a)



(b)



(c)



(d)

Figure A.2.: The ADC to MeV conversion factor for the four LTDBs.

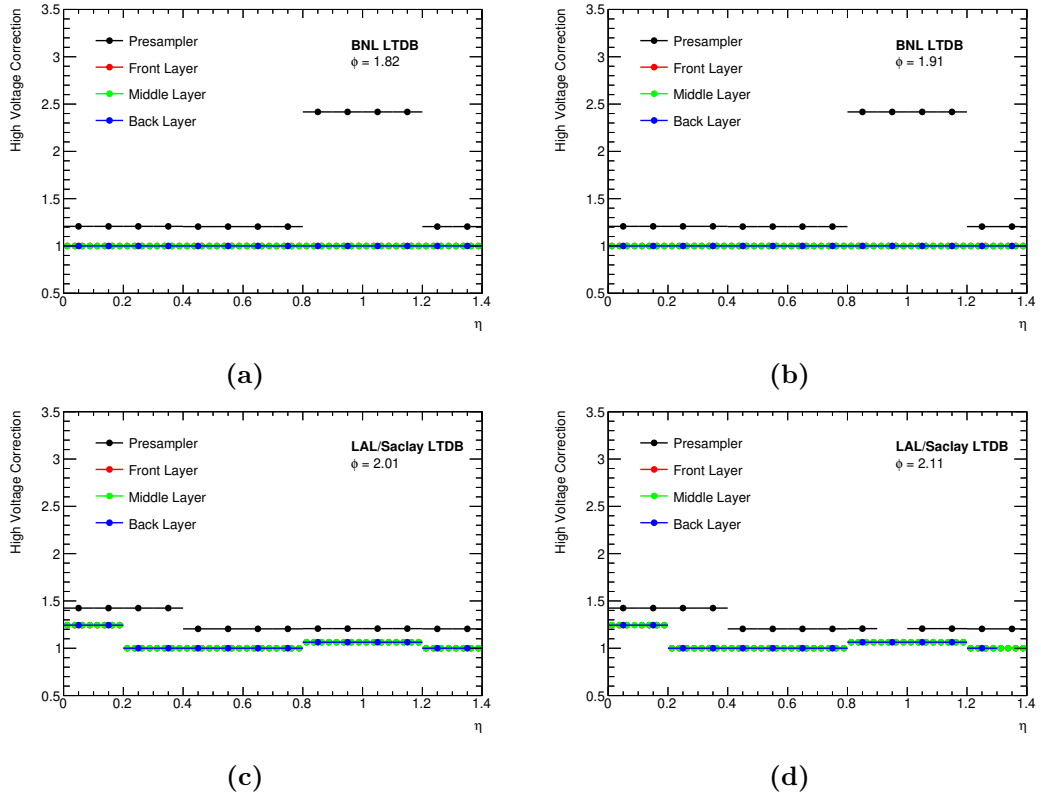


Figure A.3.: The high-voltage correction factors for the four LTDBs.

A.2. Additional Plots of the Shower-Shape Variables Study

In sections 8.4 to 8.6, the cut efficiencies of the three shower-shape variables R_η , f_3 , and $w_{\eta,2}$ are shown for the LAr demonstrator. In addition, the values of the background rejection power of the main readout are given. The corresponding figures are shown in the following.

In fig. A.4, both the cut efficiencies of R_η for electrons and jets, and the background rejection power of R_η are shown.

In fig. A.5, both the cut efficiencies of f_3 for electrons and jets, and the background rejection power of f_3 are shown.

In fig. A.6, both the cut efficiencies of $w_{\eta,2}$ for electrons and jets, and the background rejection power of $w_{\eta,2}$ are shown.

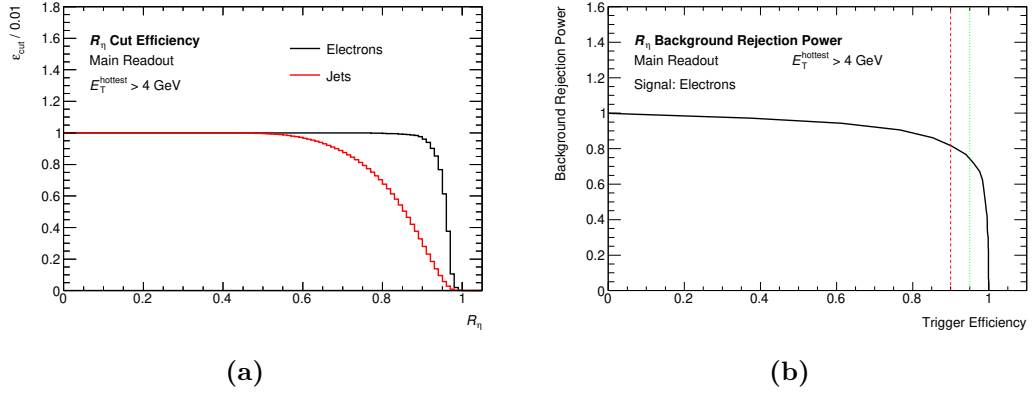


Figure A.4.: Cut efficiencies for electrons and jets and the background rejection power. For the background rejection power on the right, 90 % (red) and 95 % (green) trigger efficiency are marked.

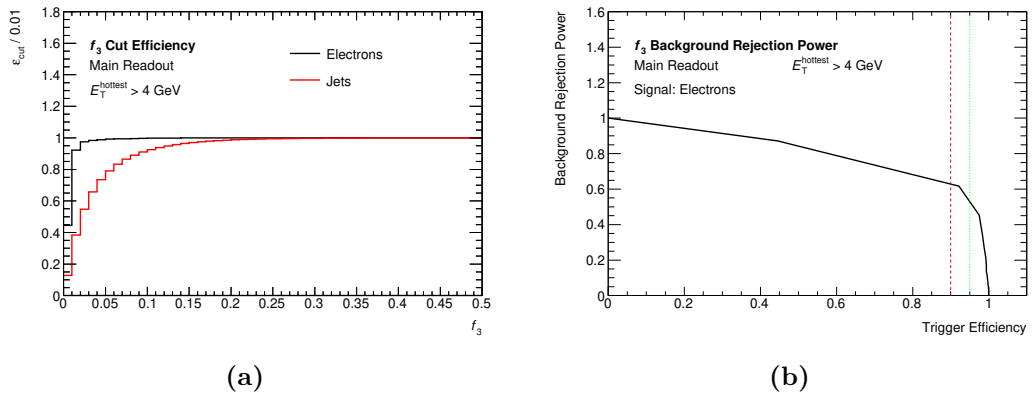
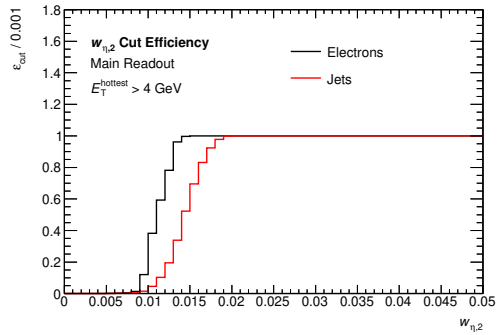
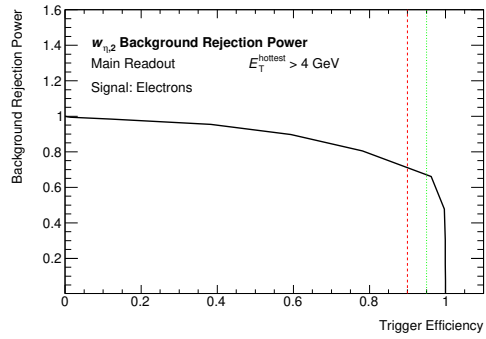


Figure A.5.: Cut efficiencies for electrons and jets and the background rejection power. For the background rejection power on the right, 90 % (red) and 95 % (green) trigger efficiency are marked.



(a)



(b)

Figure A.6.: Cut efficiencies for electrons and jets and the background rejection power. For the background rejection power on the right, 90 % (red) and 95 % (green) trigger efficiency are marked.

List of Figures

2.1. The elementary particles of the Standard Model.	7
3.1. Overview of the CERN accelerator complex.	12
3.2. Schematic view of the 25 ns filling scheme for high luminosity.	13
3.3. Total integrated luminosity for Run 1 and Run 2.	15
3.4. Schematic overview of the ATLAS detector.	16
3.5. Schematic overview of the ATLAS detector magnet system.	19
3.6. Schematic overview of the ATLAS detector inner detector.	19
3.7. Schematic overview of the ATLAS detector calorimeter.	21
3.8. Schematic overview of the ATLAS detector muon spectrometer	22
3.9. Schematic overview of the Run 2 configuration of the TDAQ system.	24
3.10. Overview of the Standard Model total production cross-section measurements at the ATLAS detector.	26
3.11. Cross-section of inelastic pp collisions as a function of \sqrt{s}	27
3.12. Exemplary inelastic pp collision at the LHC simulated with SHERPA.	28
3.13. Luminosity-weighted distribution of the average number of interactions per bunch crossing for the years 2015–2018.	29
4.1. Energy loss per radiation length X_0 of electrons and positrons in lead depending on their energy.	32
4.2. Schematic overview of the LAr calorimeter.	34
4.3. The accordion geometry of the EMB.	35
4.4. Segmentation of the EMB for $\eta = 0$ in three layers.	37
4.5. The total amount of material in radiation lengths X_0 for the EMB and the EMEC as a function of η	38
4.6. Block diagram of the current LAr calorimeter readout electronics.	40
4.7. Block diagram of the FEB architecture.	41
4.8. The different stages of the pulse processing.	42
4.9. Block diagram of L1Calo trigger.	44
5.1. Overview of the LHC operation and upgrade plan.	46
5.2. The Phase-I upgrade readout electronics of the LAr calorimeter.	48

5.3. Comparison of the granularity of the trigger tower and the supercell concept.	50
5.4. Block diagram of the new LTDB.	51
5.5. Block diagram of the new LDPS.	52
5.6. Block diagram of the L1Calo trigger Phase-I upgrade.	54
5.7. R_η distribution for electrons and background jets with $p_T > 20$ GeV.	55
5.8. f_3 distribution for electrons and background jets with $p_T > 20$ GeV.	56
5.9. $w_{\eta,2}$ distribution for electrons and background jets with $p_T > 20$ GeV.	57
5.10. Trigger rates for $\langle\mu\rangle = 80$ as a function of E_T with (a) 90% and (b) 95% trigger efficiency.	58
5.11. Measured pulse shapes of a front layer supercell of the LAr demonstrator system.	60
5.12. Measured noise level in transverse energy as a function of η of the LAr demonstrator system supercells.	61
6.1. Shaping of the LAr calorimeter detector pulse shape.	64
6.2. Comparison of measured and simulated pulse shapes of the EMB.	65
6.3. Schematic depiction of the baseline shift due to pile-up.	67
7.1. p_T distribution and η and ϕ distribution of the recorded electrons by the LAr demonstrator.	77
7.2. Optimal Filter response to a sampled pulse shape.	81
7.3. Example of the histogram of the recorded peak samples of the pulse shapes.	83
7.4. Sample of the peak of the pulse shapes.	83
7.5. A shifted baseline with a value much higher or lower than the pedestal value.	85
7.6. Response of the analog shaper to a delta peak and the unlocked-fiber pattern of the ABBA.	85
7.8. Anomalies in the recorded data.	86
8.1. Correlation, ρ , between the transverse energy deposited in the LAr demonstrator and the main readout.	89
8.2. Signal detection efficiency of four supercells.	90
8.3. Shower distribution of a matched event.	92
8.4. Energy distribution of the hottest supercell in the middle layer.	94
8.5. Difference in the coordinates of the hottest supercell of the LAr demonstrator and the main readout.	94

8.6. Comparison of the R_η distribution for electrons and jets between the LAr demonstrator and the main readout.	96
8.7. Comparison of the energy distribution in the 3×2 cluster for electrons and jets between the LAr demonstrator and the main readout.	96
8.8. Comparison of the energy distribution in the 7×2 cluster for electrons and jets between the LAr demonstrator and the main readout.	97
8.9. Comparison of the ratio between the energy in the outer part of the 7×2 cluster and the energy of the 3×2 cluster for electrons and jets.	97
8.10. Comparison of the R_η distribution for electrons and jets for the LAr demonstrator.	98
8.11. Cut efficiencies for electrons and jets and the background rejection power.	99
8.12. Comparison of the f_3 distribution for electrons and jets between the LAr demonstrator and the main readout.	100
8.13. Comparison of the energy distribution in the 3×2 cluster for electrons and jets between the LAr demonstrator and the main readout in the front layer.	101
8.14. Comparison of the energy distribution in the 2×2 cluster for electrons and jets between the LAr demonstrator and the main readout in the back layer.	101
8.15. Comparison of the f_3 distribution for electrons and jets for the LAr demonstrator.	102
8.16. Cut efficiencies for electrons and jets and the background rejection power.	102
8.17. Comparison of the $w_{\eta,2}$ distribution for electrons and jets between the LAr demonstrator and the main readout.	104
8.18. Comparison of the $w_{\eta,2}$ distribution for electrons and jets for the LAr demonstrator.	104
8.19. Cut efficiencies for electrons and jets and the background rejection power.	105
9.1. The pile-up energy spectra for the four detector layers.	111
9.2. The pile-up energy spectra of the four detector layers for different μ intervals.	112
9.3. The average pile-up energy of the four layers for different μ	113
9.4. Overview of the bunch structure of run 330470.	114
9.5. Average energy deposition for a sequence of 250 bunch crossings (four detector layers).	115

9.6. Mean energy deposition for a sequence of 250 bunch crossings (front layer, four ϕ slices).	117
9.7. Mean energy deposition for a sequence of 250 bunch crossings (front layer, two single cells).	118
9.8. Development of the average pile-up energy in the sample with the maximum of the positive baseline shift in each bunch train (red) over the course of run 333 487	119
9.9. The correlation, ρ , between the average pile-up energy deposition and μ	121
10.1. Comparison between the average detector pulse shape and the pulse shape predicted from the calibration pulse.	124
10.2. Illustration of the operating principle of the WF_{FC}	126
10.3. Filter response of the WF_{FC} and the Optimal Filter to an energy deposition in the undershoot.	127
10.4. WF_{FC} response to an energy deposition with two sets of filter coefficients for different phase shifts of the pulse shape.	128
10.5. Comparison of the signal detection efficiency of the WF_{FC} and the Optimal Filter with filter coefficients for different phase shifts of the pulse shape.	128
10.6. Filter response of the Wiener filter to an energy deposition for two different phases.	130
10.7. Signal detection efficiency of the Wiener filter with filter coefficients for different phase shifts of the pulse shape.	130
10.8. Filter response of the Wiener filter to an energy deposition for two different phases.	131
10.9. Signal detection efficiency of the Wiener filter with filter coefficients for different phase shifts of the pulse shape.	131
A.1. The measured pedestal values for the four LTDBs.	136
A.2. The ADC to MeV conversion factor for the four LTDBs.	137
A.3. The high-voltage correction factors for the four LTDBs.	138
A.4. Cut efficiencies for electrons and jets and the background rejection power.	140
A.5. Cut efficiencies for electrons and jets and the background rejection power.	140
A.6. Cut efficiencies for electrons and jets and the background rejection power.	141

List of Tables

3.1. General performance goals of the ATLAS detector.	16
4.1. Overview of the cell sizes of the different detector layers of the EMB. .	36
4.2. Overview of the cell sizes of the different detector layers of the EMEC.	38
5.1. Comparison of the current trigger tower granularity and the future supercell granularity in the EMB.	49
7.1. The bits of the TType and their meaning.	76
7.2. The relation between the source ID, the ABBA FPGA, the LTDB, and the ϕ -slice.	79
8.1. Achieved trigger efficiency and background rejection power with the two sets of optimized cut parameters for the shower-shape variables. .	106
8.2. Achieved trigger efficiency and background rejection power with the variation of the cut parameters for the shower-shape variables.	107
9.1. Average pile-up energy of the four detector layers for different μ intervals.	112

Glossary

***pp* collision** Proton-Proton Collision

ABBA ATCA Test Board for Baseline Acquisition

ADC Analog-to-Digital Converter

ALICE A Large Ion Collider Experiment

AOD Analysis Object Data

AREUS ATLAS Readout Electronics Upgrade Simulation

ATLAS A Toroidal LHC ApparatuS

BCID Bunch-Crossing Identification

CERN European Organization for Nuclear Research

CMS Compact Muon Solenoid

DESY German Electron Synchrotron

EMB Electromagnetic Barrel Calorimeter

EMEC Electromagnetic End-Cap Calorimeter

ESD Event Summary Data

FCal Forward Calorimeter

FEB Front-End Board

FEC Front-End Crate

FIR filter Finite Impulse Response Filter

FPGA Field Programmable Gate Array

FTK Fast Tracker

HEC Hadronic End-Cap Calorimeter

HL-LHC High Luminosity LHC

IIR filter Infinite Impulse Response Filter

L1 trigger Level-1 Trigger

L1A signal Level-1 Trigger Accept Signal

L1Calo trigger Level-1 Calorimeter Trigger

L1ID Level-1 Identification

L1Muon trigger Level-1 Muon Trigger

L1Topo trigger Level-1 Topological Trigger

L2 trigger Level-2 Trigger

LAr calorimeter Liquid-Argon Calorimeter

LArC board Liquid-Argon Carrier Board

LATOME LAr Trigger prOcessing MEzzanine

LDPB LAr Digital Processing Blade

LDPS LAr Digital Processing System

LHC Large Hadron Collider

LHCb Large Hadron Collider beauty

Long Shutdown 1 Long Shutdown 1

Long Shutdown 2 Long Shutdown 2

Long Shutdown 3 Long Shutdown 3

LTDB LAr Trigger Digitizer Board

Optimal Filter Optimal Filter

QCD Quantum Chromodynamics

QED Quantum Electrodynamics

TBB Tower-Builder Board

TDAQ system Trigger and Data Acquisition System

TDB Tower-Driver Board

TType Trigger Type

WF_{FC} Wiener Filter with Forward Correction

Wiener filter Wiener Filter

Bibliography

- [1] S. L. Glashow, *Partial Symmetries of Weak Interactions*, Nucl. Phys. **22** (1961) 579.
- [2] Steven Weinberg, *A Model of Leptons*, Physical Review Letters **19** (1967) 1264.
- [3] Abdus Salam, “Elementary particle theory”, *Prog. Of the Nobel Symposium, 1968, Stockholm, Sweden*, vol. 367, 1968.
- [4] Gerard 't Hooft, *Renormalizable Lagrangians for Massive Yang-Mills Fields*, Nucl. Phys. **B35** (1971) 167, [,201(1971)].
- [5] Gerard 't Hooft and M. J. G. Veltman, *Regularization and Renormalization of Gauge Fields*, Nucl. Phys. **B44** (1972) 189.
- [6] Oliver Sim Brüning et al., *LHC Design Report Vol.1: The LHC Main Ring*, CERN Yellow Reports: Monographs, Geneva: CERN, 2004, URL: <http://cds.cern.ch/record/782076>; Oliver Sim Brüning et al., *LHC Design Report. 2. The LHC infrastructure and general services*, CERN Yellow Reports: Monographs, Geneva: CERN, 2004, URL: <http://cds.cern.ch/record/815187>; Michael Benedikt, Paul Collier, V Mertens, John Poole, and Karlheinz Schindl, *LHC Design Report. 3. The LHC injector chain*, CERN Yellow Reports: Monographs, Geneva: CERN, 2004, URL: <http://cds.cern.ch/record/823808>.
- [7] Lyndon Evans and Philip Bryant, *LHC Machine*, JINST **3** (2008) S08001.
- [8] ATLAS Collaboration, *The ATLAS Experiment at the CERN Large Hadron Collider*, JINST **3** (2008) S08003.
- [9] ATLAS Collaboration, *Observation of a new particle in the search for the Standard Model Higgs boson with the ATLAS detector at the LHC*, Phys. Lett. **B716** (2012) 1, arXiv: 1207.7214 [hep-ex].

- [10] CMS Collaboration, *Observation of a new boson at a mass of 125 GeV with the CMS experiment at the LHC*, Phys. Lett. **B716** (2012) 30, arXiv: 1207.7235 [hep-ex].
- [11] ATLAS Collaboration, *Letter of Intent for the Phase-I Upgrade of the ATLAS Experiment*, tech. rep. CERN-LHCC-2011-012. LHCC-I-020, CERN, 2011, URL: <http://cds.cern.ch/record/1402470>.
- [12] Bose, *Plancks Gesetz und Lichtquantenhypothese*, Zeitschrift für Physik **26** (1924) 178, ISSN: 0044-3328, URL: <https://doi.org/10.1007/BF01327326>.
- [13] E. Fermi, *Zur Quantelung des idealen einatomigen Gases*, Zeitschrift für Physik **36** (1926) 902.
- [14] Paul Adrien Maurice Dirac, *On the theory of quantum mechanics*, Proc. R. Soc. Lond. A **112** (1926) 661.
- [15] David J Griffiths, *Introduction to elementary particles*, TextBook Physics, Wiley, 1987.
- [16] A. Das and T. Ferbel, *Introduction to Nuclear and Particle Physics*, Second, WORLD SCIENTIFIC, 2003, eprint: <https://www.worldscientific.com/doi/pdf/10.1142/5460>, URL: <https://www.worldscientific.com/doi/abs/10.1142/5460>.
- [17] Guy Coughlan, J. E. Dodd, and B. M. Gripaios, *The Ideas of Particle Physics: An Introduction for Scientists*, Cambridge University Press, 2006.
- [18] K. Bethge and U. E. Schröder, *Elementarteilchen und ihre Wechselwirkungen: Eine Übersicht*, Lehrbuch Physik, Wiley, 2012, ISBN: 9783527662166.
- [19] Bogdan Povh, Klaus Rith, Christoph Scholz, Frank Zetsche, and Werner Rodejohann, *Particles and nuclei: an introduction to the physical concepts; 7th ed.* Graduate texts in physics, Springer, 2015.
- [20] Emmy Noether, *Invariant variation problems*, Transport Theory and Statistical Physics **1** (1971) 186.
- [21] Peter W. Higgs, *Broken symmetries, massless particles and gauge fields*, Phys. Lett. **12** (1964) 132.

-
- [22] Peter W. Higgs, *Broken Symmetries and the Masses of Gauge Bosons*, Phys. Rev. Lett. **13** (1964) 508, [,160(1964)].
- [23] Peter W. Higgs, *Spontaneous Symmetry Breakdown without Massless Bosons*, Phys. Rev. **145** (1966) 1156.
- [24] F. Englert and R. Brout, *Broken Symmetry and the Mass of Gauge Vector Mesons*, Physical Review Letters **13** (1964) 321, [,157(1964)].
- [25] G. S. Guralnik, C. R. Hagen, and T. W. B. Kibble, *Global Conservation Laws and Massless Particles*, Phys. Rev. Lett. **13** (1964) 585, [,162(1964)].
- [26] R. P. Feynman, *Mathematical formulation of the quantum theory of electromagnetic interaction*, Phys. Rev. **80** (1950) 440, [,198(1950)].
- [27] E. Fermi, *An attempt of a theory of beta radiation. 1.*, Z. Phys. **88** (1934) 161.
- [28] H. Fritzsch, Murray Gell-Mann, and H. Leutwyler, *Advantages of the Color Octet Gluon Picture*, Phys. Lett. **47B** (1973) 365.
- [29] H. David Politzer, *Reliable Perturbative Results for Strong Interactions?*, Phys. Rev. Lett. **30** (1973) 1346, [,274(1973)].
- [30] David J. Gross and Frank Wilczek, *Ultraviolet Behavior of Nonabelian Gauge Theories*, Phys. Rev. Lett. **30** (1973) 1343, [,271(1973)].
- [31] Steven Weinberg, *Nonabelian Gauge Theories of the Strong Interactions*, Phys. Rev. Lett. **31** (1973) 494.
- [32] MissMJ, *Standard Model of Elementary Particles*, 2006,
URL: https://commons.wikimedia.org/wiki/File:Standard_Model_of_Elementary_Particles.svg.
- [33] R. Brandelik et al., *Evidence for Planar Events in $e^+ e^-$ Annihilation at High-Energies*, Phys. Lett. **86B** (1979) 243.
- [34] D. P. Barber et al., *Discovery of Three Jet Events and a Test of Quantum Chromodynamics at PETRA Energies*, Phys. Rev. Lett. **43** (1979) 830.
- [35] Christoph Berger et al., *Evidence for Gluon Bremsstrahlung in $e^+ e^-$ Annihilations at High-Energies*, Phys. Lett. **86B** (1979) 418.

- [36] W. Bartel et al., *Observation of Planar Three Jet Events in $e^+ e^-$ Annihilation and Evidence for Gluon Bremsstrahlung*, Phys. Lett. **91B** (1980) 142.
- [37] G. Arnison et al., *Experimental Observation of Isolated Large Transverse Energy Electrons with Associated Missing Energy at $s^{*(1/2)} = 540\text{-GeV}$* , Phys. Lett. **B122** (1983) 103, [,611(1983)].
- [38] M. Banner et al., *Observation of Single Isolated Electrons of High Transverse Momentum in Events with Missing Transverse Energy at the CERN anti- $p p$ Collider*, Phys. Lett. **B122** (1983) 476, [,7.45(1983)].
- [39] G. Arnison et al., *Experimental Observation of Lepton Pairs of Invariant Mass Around $95\text{-GeV}/c^{*2}$ at the CERN SPS Collider*, Phys. Lett. **B126** (1983) 398, [,7.55(1983)].
- [40] A. Einstein, *Die Grundlage der allgemeinen Relativitätstheorie*, Annalen der Physik **354** (1916) 769, eprint: <https://onlinelibrary.wiley.com/doi/pdf/10.1002/andp.19163540702>, URL: <https://onlinelibrary.wiley.com/doi/abs/10.1002/andp.19163540702>.
- [41] Y. Fukuda et al., *Evidence for oscillation of atmospheric neutrinos*, Phys. Rev. Lett. **81** (1998) 1562, arXiv: hep-ex/9807003 [hep-ex].
- [42] Q. R. Ahmad et al., *Measurement of the rate of $\nu_e + d \rightarrow p + p + e^-$ interactions produced by 8B solar neutrinos at the Sudbury Neutrino Observatory*, Phys. Rev. Lett. **87** (2001) 071301, arXiv: nucl-ex/0106015 [nucl-ex].
- [43] CERN Physics, *Dark matter*, Accessed: 2019-06-19, URL: <https://home.cern/science/physics/dark-matter>.
- [44] Laurent Canetti, Marco Drewes, and Mikhail Shaposhnikov, *Matter and Antimatter in the Universe*, New J. Phys. **14** (2012) 095012, arXiv: 1204.4186 [hep-ph].
- [45] John Ellis, *The Physics Landscape after the Higgs Discovery at the LHC*, Nucl. Part. Phys. Proc. **267-269** (2015) 3, arXiv: 1504.03654 [hep-ph].
- [46] Stephen P. Martin, *A Supersymmetry primer*, (1997) 1, [Adv. Ser. Direct. High Energy Phys.18,1(1998)], arXiv: hep-ph/9709356 [hep-ph].

- [47] Pierre Fayet, *About the origins of the supersymmetric standard model*, Nucl. Phys. Proc. Suppl. **101** (2001) 81, [,81(2001)], arXiv: hep-ph/0107228 [hep-ph].
- [48] Salvatore Rappoccio, *The experimental status of direct searches for exotic physics beyond the standard model at the Large Hadron Collider*, Rev. Phys. **4** (2019) 100027, arXiv: 1810.10579 [hep-ex].
- [49] LEP Collaboration, *LEP Design Report: Vol.2. The LEP Main Ring*, CERN, 1984.
- [50] Esmâ Mobs, *The CERN accelerator complex - August 2018. Complexe des accélérateurs du CERN*, General Photo, 2018, URL: <https://cds.cern.ch/record/2636343>.
- [51] R Bailey and Paul Collier, *Standard Filling Schemes for Various LHC Operation Modes*, tech. rep. LHC-PROJECT-NOTE-323, CERN, 2003, URL: <https://cds.cern.ch/record/691782>.
- [52] ALICE Collaboration, *The ALICE experiment at the CERN LHC*, JINST **3** (2008) S08002.
- [53] LHCb Collaboration, *The LHCb Detector at the LHC*, JINST **3** (2008) S08005.
- [54] CMS Collaboration, *The CMS Experiment at the CERN LHC*, JINST **3** (2008) S08004.
- [55] *First beam in the LHC - accelerating science*, Accessed: 2019-06-19, 2008, URL: <https://home.cern/news/press-release/cern/first-beam-lhc-accelerating-science>.
- [56] *CERN releases analysis of LHC incident*, Accessed: 2019-06-19, 2008, URL: <https://home.cern/news/press-release/cern/cern-releases-analysis-lhc-incident>.
- [57] *The LHC is back*, Accessed: 2019-06-19, 2009, URL: <https://home.cern/news/press-release/cern/lhc-back>.
- [58] *LHC sets new record - accelerates beam to 3.5 TeV*, Accessed: 2019-06-19, 2010, URL: <https://home.cern/news/press-release/cern/lhc-sets-new-record-accelerates-beam-35-tev>.

- [59] *LHC physics data taking gets underway at new record collision energy of 8 TeV*, Accessed: 2019-06-19, 2012,
URL: <https://home.cern/news/press-release/cern/lhc-physics-data-taking-gets-underway-new-record-collision-energy-8tev>.
- [60] Mike Lamont,
“The First Years of LHC Operation for Luminosity Production”,
Proceedings, 4th International Particle Accelerator Conference (IPAC 2013): Shanghai, China, May 12-17, 2013, 2013 MOYAB101,
URL: <http://JACoW.org/IPAC2013/papers/moyab101.pdf>.
- [61] *Proton beams are back in the LHC*, Accessed: 2019-06-19, 2015, URL: <https://home.cern/news/press-release/cern/proton-beams-are-back-lhc>.
- [62] *LHC experiments back in business at record energy*, Accessed: 2019-06-19, 2015, URL: <https://home.cern/news/news/accelerators/lhc-experiments-back-business-record-energy-0>.
- [63] ATLAS Collaboration, *Luminosity determination in pp collisions at $\sqrt{s} = 13$ TeV using the ATLAS detector at the LHC*,
tech. rep. ATLAS-CONF-2019-021, CERN, 2019,
URL: <http://cds.cern.ch/record/2677054>.
- [64] *LHC prepares for new achievements*, Accessed: 2019-06-19, 2018,
URL: <https://home.cern/news/press-release/accelerators/lhc-prepares-new-achievements>.
- [65] ATLAS Collaboration, *Total Integrated Luminosity in 2011 and 2012*, 2013,
URL: <https://twiki.cern.ch/twiki/bin/view/AtlasPublic/LuminosityPublicResults>.
- [66] ATLAS Collaboration,
Total Integrated Luminosity at Run 2 (13 TeV pp data only),
URL: https://twiki.cern.ch/twiki/bin/view/AtlasPublic/LuminosityPublicResultsRun2#Multiple_Year_Collision_Plots.
- [67] ATLAS Collaboration, *The ATLAS central solenoid*,
Nucl. Instrum. Methods Phys. Res., A **584** (2007) 53,
URL: <http://cds.cern.ch/record/1069672>.
- [68] ATLAS Collaboration, *ATLAS inner detector: Technical Design Report, 1*,
Technical Design Report ATLAS, CERN, 1997,
URL: <http://cds.cern.ch/record/331063>.

- [69] ATLAS Collaboration, *ATLAS inner detector: Technical Design Report, 2*, Technical Design Report ATLAS, CERN, 1997, URL: <http://cds.cern.ch/record/331064>.
- [70] ATLAS Collaboration, *ATLAS pixel detector: Technical design report*, tech. rep., CERN, 1998.
- [71] ATLAS Collaboration, *ATLAS pixel detector electronics and sensors*, JINST **3** (2008) P07007.
- [72] ATLAS Collaboration, *ATLAS Insertable B-Layer Technical Design Report*, tech. rep. CERN-LHCC-2010-013. ATLAS-TDR-19, CERN, 2010, URL: <https://cds.cern.ch/record/1291633>.
- [73] ATLAS Collaboration, *The Silicon microstrip sensors of the ATLAS semiconductor tracker*, tech. rep., CERN, 2007 98.
- [74] ATLAS Collaboration, *The ATLAS Transition Radiation Tracker (TRT) proportional drift tube: Design and performance*, JINST **3** (2008) P02013.
- [75] Bartosz Mindur, *ATLAS Transition Radiation Tracker (TRT): Straw tubes for tracking and particle identification at the Large Hadron Collider*, tech. rep. ATL-INDET-PROC-2016-001, CERN, 2016, URL: <https://cds.cern.ch/record/2139567>.
- [76] ATLAS Collaboration, *ATLAS liquid-argon calorimeter: Technical Design Report*, Technical Design Report ATLAS, CERN, 1996, URL: <http://cds.cern.ch/record/331061>.
- [77] ATLAS Collaboration, *ATLAS tile calorimeter: Technical Design Report*, Technical Design Report ATLAS, CERN, 1996, URL: <http://cds.cern.ch/record/331062>.
- [78] ATLAS Collaboration, *ATLAS muon spectrometer: Technical Design Report*, Technical Design Report ATLAS, CERN, 1997, URL: <http://cds.cern.ch/record/331068>.
- [79] ATLAS Collaboration, *ATLAS high-level trigger, data-acquisition and controls: Technical Design Report*, Technical Design Report ATLAS, CERN, 2003, URL: <https://cds.cern.ch/record/616089>.
- [80] Yu Nakahama, *The ATLAS Trigger System: Ready for Run-2*, J. Phys. Conf. Ser. **664** (2015) 082037, URL: <http://cds.cern.ch/record/2015211>.

- [81] Moritz Backes, *The ATLAS Trigger System: Ready for Run-2*, PoS **LeptonPhoton2015** (2016) 045, URL: <http://cds.cern.ch/record/2058618>.
- [82] ATLAS Collaboration, *Technical Design Report for the Phase-I Upgrade of the ATLAS TDAQ System*, tech. rep. CERN-LHCC-2013-018. ATLAS-TDR-023, Final version presented to December 2013 LHCC., 2013, URL: <http://cds.cern.ch/record/1602235>.
- [83] ATLAS Collaboration, *The ATLAS Level-1 Trigger system*, J. Phys. Conf. Ser. **396** (2012) 012010.
- [84] ATLAS Collaboration, *Upgrade of the ATLAS Level-1 Trigger with event topology information*, tech. rep. ATL-DAQ-PROC-2015-017. 8, CERN, 2015, URL: <https://cds.cern.ch/record/2016644>.
- [85] G J Alner et al., *The UA5 high energy $\bar{p}p$ simulation program*, Nucl. Phys. B **291** (1986) 445, URL: <http://cds.cern.ch/record/173907>.
- [86] R. K. Ellis, W. J. Stirling, and B. R. Webber, *QCD and Collider Physics*, Cambridge Monographs on Particle Physics, Nuclear Physics and Cosmology, Cambridge University Press, 1996.
- [87] R. P. Feynman, *The behavior of hadron collisions at extreme energies*, Conf. Proc. **C690905** (1969) 237.
- [88] ATLAS Collaboration, *Summary plots from the ATLAS Standard Model physics group*, 2018, URL: <https://atlas.web.cern.ch/Atlas/GROUPS/PHYSICS/CombinedSummaryPlots/SM/>.
- [89] M. Aaboud et al., *Measurement of the Inelastic Proton-Proton Cross Section at $\sqrt{s} = 13$ TeV with the ATLAS Detector at the LHC*, Phys. Rev. Lett. **117** (2016) 182002, arXiv: 1606.02625 [hep-ex].
- [90] W. Heisenberg, *Mesonenerzeugung als Stosswellenproblem*, Z. Phys. **133** (1952) 65.
- [91] John M. Campbell, J. W. Huston, and W. J. Stirling, *Hard Interactions of Quarks and Gluons: A Primer for LHC Physics*, Rept. Prog. Phys. **70** (2007) 89, arXiv: hep-ph/0611148 [hep-ph].
- [92] Enrico Bothmann et al., *Event Generation with SHERPA 2.2*, (2019), arXiv: 1905.09127 [hep-ph].

-
- [93] Amber Harmon, Accessed: 2019-06-12, 2014,
URL: <https://sciencenode.org/feature/sherpa-and-open-science-grid-predicting-emergence-jets.php>.
- [94] Torbjorn Sjostrand, “Monte Carlo Generators”, *High-energy physics. Proceedings, European School, Aronsborg, Sweden, June 18-July 1, 2006*, 2006 51, arXiv: hep-ph/0611247 [hep-ph],
URL: <http://weplib.cern.ch/abstract?CERN-LCGAPP-2006-06>.
- [95] Maxim Perelstein, “Introduction to Collider Physics”, *Physics of the large and the small, TASI 09, proceedings of the Theoretical Advanced Study Institute in Elementary Particle Physics, Boulder, Colorado, USA, 1-26 June 2009*, 2011 421, arXiv: 1002.0274 [hep-ph].
- [96] Michael G. Albrow et al., *Tevatron-for-LHC Report of the QCD Working Group. Tevatron-for-LHC Report of the QCD Working Group*, tech. rep. hep-ph/0610012. Fermilab-Conf-2006-359, FERMILAB, 2006,
URL: <https://cds.cern.ch/record/987065>.
- [97] ATLAS Collaboration, *Number of Interactions per Crossing*,
URL: https://twiki.cern.ch/twiki/bin/view/AtlasPublic/LuminosityPublicResultsRun2#Pileup_Interactions_and_Data_Tak.
- [98] Michael Leyton,
“Minimum Bias and Underlying Event Measurements with ATLAS”,
Proceedings, 3rd International Workshop on Multiple Partonic Interactions at the LHC (MPI@LHC 2011): Hamburg, Germany, 21-25 Nov 2011, 2012 11,
arXiv: 1202.2090 [hep-ex].
- [99] Christian Wolfgang Fabjan and F Gianotti, *Calorimetry for Particle Physics*,
Rev. Mod. Phys. **75** (2003) 1243,
URL: <http://cds.cern.ch/record/692252>.
- [100] M. Tanabashi et al., *Review of Particle Physics*,
Phys. Rev. D **98** (3 2018) 030001,
URL: <https://link.aps.org/doi/10.1103/PhysRevD.98.030001>.
- [101] ATLAS Collaboration, *Drift Time Measurement in the ATLAS Liquid Argon Electromagnetic Calorimeter using Cosmic Muons*,
Eur. Phys. J. **C70** (2010) 755, arXiv: 1002.4189 [physics.ins-det].
- [102] ATLAS Collaboration, *The ATLAS Liquid Argon calorimeter: An overview*,
Journal of Physics: Conference Series **160** (2009) 012043,
URL: <https://doi.org/10.1088%2F1742-6596%2F160%2F1%2F012043>.
-

- [103] Joao Pequena, “Computer generated image of the ATLAS Liquid Argon”, 2008, URL: <https://cds.cern.ch/record/1095928>.
- [104] ATLAS Collaboration, *ATLAS liquid argon calorimeter front end electronics*, JINST **3** (2008) P09003.
- [105] ATLAS Collaboration, *ATLAS liquid argon calorimeter back end electronics*, JINST **2** (2007) P06002.
- [106] ATLAS Collaboration, *The ATLAS level-1 calorimeter trigger*, JINST **3** (2008) P03001.
- [107] Letizia Diamante, *Key plans for the next two years of the LHC*, Accessed: 2019-07-09, 2018, URL: <https://home.cern/news/news/accelerators/key-plans-next-two-years-lhc>.
- [108] ATLAS Collaboration, *Technical Design Report for the Phase-II Upgrade of the ATLAS LAr Calorimeter*, tech. rep. CERN-LHCC-2017-018. ATLAS-TDR-027, CERN, 2017, URL: <https://cds.cern.ch/record/2285582>.
- [109] G. Apollinari et al., *High-Luminosity Large Hadron Collider (HL-LHC)*, CERN Yellow Rep. Monogr. **4** (2017) 516.
- [110] *LHC Schedule*, Accessed: 2019-07-09, URL: <https://project-hl-lhc-industry.web.cern.ch/content/project-schedule>.
- [111] *LS2 Report: ATLAS upgrades are in full swing*, Accessed: 2019-11-21, 2019, URL: <https://home.cern/news/news/experiments/ls2-report-atlas-upgrades-are-full-swing>.
- [112] ATLAS Collaboration, *New Small Wheel Technical Design Report*, tech. rep. CERN-LHCC-2013-006. ATLAS-TDR-020, ATLAS New Small Wheel Technical Design Report, 2013, URL: <http://cds.cern.ch/record/1552862>.
- [113] ATLAS Collaboration, *ATLAS Liquid Argon Calorimeter Phase-I Upgrade Technical Design Report*, tech. rep. CERN-LHCC-2013-017. ATLAS-TDR-022, Final version presented to December 2013 LHCC., 2013, URL: <http://cds.cern.ch/record/1602230>.
- [114] ATLAS Collaboration, *The ATLAS Simulation Infrastructure*, Eur. Phys. J. **C70** (2010) 823, arXiv: 1005.4568 [physics.ins-det].

- [115] Torbjörn Sjöstrand et al., *An Introduction to PYTHIA 8.2*, Comput. Phys. Commun. **191** (2015) 159, arXiv: 1410.3012 [hep-ph].
- [116] S. Agostinelli et al., *GEANT4: A Simulation toolkit*, Nucl. Instrum. Meth. **A506** (2003) 250.
- [117] N. Dumont Dayot,
Performance of the Demonstrator System for the Phase-I Upgrade of the Trigger Readout Electronics of the ATLAS Liquid Argon Calorimeters, Journal of Instrumentation **11** (2016) C01026,
URL: <https://doi.org/10.1088/1748-0221/11/01/C01026>.
- [118] Nicolas Dumont Dayot,
Development of an ATCA IPMI controller mezzanine board to be used in the ATCA developments for the ATLAS Liquid Argon upgrade, Journal of Instrumentation **7** (2012) C01020,
URL: <https://doi.org/10.1088/1748-0221/7/01/C01020>.
- [119] Dominique Besin et al., “Design and Evaluation of LAr Trigger Digitizer Board in the ATLAS Phase-I Upgrade”, *21st IEEE Real Time Conference (RT2018) Williamsburg, USA, June 11-15, 2018*, 2019, arXiv: 1806.08046 [physics.ins-det].
- [120] ATLAS Collaboration,
Public Liquid-Argon Calorimeter Plots on Detector Status, Accessed: 2019-10-24, URL: <https://twiki.cern.ch/twiki/bin/view/AtlasPublic/LArCaloPublicResultsDetStatus>.
- [121] Saeed V Vaseghi, *Advanced digital signal processing and noise reduction*, John Wiley & Sons, 2008.
- [122] Anne-Sophie Reimer, “Performance of the Demonstrator System of the future ATLAS LAr Calorimeter Trigger Readout”, MA thesis: TU Dresden, 2018.
- [123] John G. Proakis and Dimitris K. Manolakis,
Digital Signal Processing (4th Edition), Prentice-Hall, Inc., 2006, ISBN: 0131873741.
- [124] W. E. Cleland and E. G. Stern, *Signal processing considerations for liquid ionization calorimeters in a high rate environment*, Nucl. Instrum. Meth. **A338** (1994) 467.

- [125] Steffen Stärz, “Energy Reconstruction and high-speed Data Transmission with FPGAs for the Upgrade of the ATLAS Liquid Argon Calorimeter at LHC”, Presented 19 May 2015, PhD thesis, 2015, URL: <http://cds.cern.ch/record/2030122>.
- [126] Max Köhler, “Entwurf und Implementierung von parametrierbaren Filteralgorithmen für die digitale Ausleselektronik des Flüssig-Argon-Kalorimeters des ATLAS-Detektors am CERN”, MA thesis: TU Dresden, 2012.
- [127] Johannes Philipp Grohs, “Simulation of the upgraded Phase-1 Trigger Readout Electronics of the Liquid-Argon Calorimeter of the ATLAS Detector at the LHC”, Presented 29 Feb 2016, PhD thesis, 2015, URL: <http://cds.cern.ch/record/2135931>.
- [128] Maximilian Hils, “Simulation der Energierekonstruktion der verbesserten Flüssigargon-Kalorimeter-Auslese bei ATLAS”, Presented 2015, MA thesis, 2015, URL: <http://cds.cern.ch/record/2047453>.
- [129] *TopoAlgoDef.py*, Accessed: 2019-11-08, ATLAS Collaboration, URL: <https://svnweb.cern.ch/trac/atlasoff/browser/Trigger/TriggerCommon/TriggerMenu/trunk/python/l1topomenu/TopoAlgoDef.py#L1191>.
- [130] *LAr Demonstrator Twiki*, Accessed: 2019-10-29, ATLAS Collaboration, URL: <https://twiki.cern.ch/twiki/bin/viewauth/LAr/LArDemonstrator>.
- [131] Sune Jakobsen, “Commissioning of the Absolute Luminosity For ATLAS detector at the LHC”, Presented 31 Jan 2014, 2013, URL: <https://cds.cern.ch/record/1637195>.
- [132] ATLAS Collaboration, *Fast TracKer (FTK) Technical Design Report*, tech. rep. CERN-LHCC-2013-007. ATLAS-TDR-021, ATLAS Fast Tracker Technical Design Report, 2013, URL: <http://cds.cern.ch/record/1552953>.
- [133] Karl Jakobs, *Development of FTK*, ATLAS Collaboration, 2019, URL: https://indico.cern.ch/event/740440/contributions/3557060/subcontributions/290223/attachments/1924870/3185474/CB_FTK_2019.10.11.pdf.
- [134] Ketevi A Assamagan et al., *Final report of the ATLAS AOD/ESD Definition Task Force*, (2004).

- [135] *Event Data Model In ATLAS*, CHEP 2006 Proceedings, ATLAS Collaboration, 2006.
- [136] *The Calorimeter Event Data Model In ATLAS*, CHEP 2006 Proceedings, ATLAS Collaboration, 2006.
- [137] R. Brun and F. Rademakers,
ROOT: An object oriented data analysis framework,
Nucl. Instrum. Meth. **A389** (1997) 81, URL: <https://root.cern.ch/>.
- [138] *NTP Timescale and Leap Seconds*, Accessed: 2019-11-22,
URL: <http://doc.ntp.org/4.1.2/leap.htm>.
- [139] S. Ask et al., *The ATLAS central level-1 trigger logic and TTC system*,
JINST **3** (2008) P08002.
- [140] RD Schaffer and Stanislaus Cornelius Maria Bentvelsen,
Definition of Offline Readout Identifiers for the ATLAS detector,
tech. rep. ATL-SOFT-2001-004,
revised version number 1 submitted on 2001-05-28 13:21:00: CERN, 2001,
URL: <http://cds.cern.ch/record/684167>.
- [141] ATLAS Collaboration, *Athena*, version 22.0.1, 2019,
URL: <https://doi.org/10.5281/zenodo.2641997>.
- [142] *Calibration Constants from Athena*, Accessed: 2019-11-05,
ATLAS Collaboration, URL: https://gitlab.cern.ch/LAr_Demonstrator/CalibrationConstants_fromAthena.
- [143] Georges Aad et al., *Electron performance measurements with the ATLAS detector using the 2010 LHC proton-proton collision data*,
Eur. Phys. J. **C72** (2012) 1909, arXiv: 1110.3174 [hep-ex].
- [144] Matteo Cacciari, Gavin P. Salam, and Gregory Soyez,
The anti- k_t jet clustering algorithm, JHEP **04** (2008) 063,
arXiv: 0802.1189 [hep-ph].
- [145] *LuminosityPublicResultsRun2*, Accessed: 2019-11-17, ATLAS Collaboration,
URL: <https://twiki.cern.ch/twiki/bin/view/AtlasPublic/LuminosityPublicResultsRun2>.
- [146] Ferenc Sikler, *Towards the measurement of charged hadron spectra in CMS*,
tech. rep. CMS-CR-2008-077, CERN, 2008,
URL: <http://cds.cern.ch/record/1166334>.

- [147] A. A. Bylinkin and A. A. Rostovtsev, “Systematic studies of hadron production spectra in collider experiments”, *Proceedings, 40th International Symposium on Multiparticle Dynamics (ISMD 2010): Antwerp, Belgium, September 21-25, 2010*, 2010 103, arXiv: 1008.0332 [hep-ph].
- [148] *ATLAS Run Queries*, Accessed: 2019-11-25, ATLAS Collaboration, URL: <https://atlas-runquery.cern.ch/>.
- [149] *Information on Bunch Group Set 1902*, Accessed: 2019-11-25, ATLAS Collaboration, URL: <https://atlas-trigconf.cern.ch/bunchgroups?key=1902>.
- [150] Morad Aaboud et al., *Performance of the ATLAS Trigger System in 2015*, Eur. Phys. J. **C77** (2017) 317, arXiv: 1611.09661 [hep-ex].
- [151] D. Banfi, M. Delmastro, and M. Fanti, *Cell response equalisation of the ATLAS electromagnetic calorimeter without the direct knowledge of the ionisation signals*, JINST **1** (2006) P08001.
- [152] L Courneyea et al., *Computation and validation of the electronic calibration constants for the ATLAS Liquid Argon Calorimeters*, tech. rep. ATL-LARG-INT-2010-007, CERN, 2010, URL: <https://cds.cern.ch/record/1278462>.

Erklärung

Hiermit versichere ich, dass ich die vorliegende Arbeit ohne unzulässige Hilfe Dritter und ohne Benutzung anderer als der angegebenen Hilfsmittel angefertigt habe; die aus fremden Quellen direkt oder indirekt übernommenen Gedanken sind als solche kenntlich gemacht. Die Arbeit wurde bisher weder im Inland noch im Ausland in gleicher oder ähnlicher Form einer anderen Prüfungsbehörde vorgelegt.

Die vorliegende Dissertation wurde am Institut für Kern- und Teilchenphysik der Technischen Universität Dresden unter wissenschaftlicher Betreuung von Prof. Dr. Arno Straessner angefertigt.

Es haben keine früheren erfolglosen Promotionsverfahren stattgefunden.

Ich erkenne die Promotionsordnung des Bereichs Mathematik und Naturwissenschaften an der Technischen Universität Dresden vom 23.02.2011 an.

Dresden, den 20. Dezember 2019

Maximilian Hils